



Defence Research and
Development Canada

Recherche et développement
pour la défense Canada



GMES Sentinel-1 Analysis of Marine Applications Potential (AMAP)

Paris W. Vachon and John Wolfe

This publication is protected by copyright.

Defence R&D Canada warrants that the work was performed in a professional manner conforming to generally accepted practices for scientific research and development.

This report is not a statement of endorsement by the Department of National Defence or the Government of Canada.

Defence R&D Canada – Ottawa
EXTERNAL CLIENT REPORT
DRDC Ottawa ECR 2008-218
October 2008

Canada

GMES Sentinel-1 Analysis of Marine Applications Potential (AMAP)

Paris W. Vachon and John Wolfe
DRDC Ottawa

Prepared For:
The European Space Agency
The European Space Research and Technology Centre - ESTEC
Keplerlaan 1,
NL-2201 AZ Noordwijk
The Netherlands

This publication is protected by copyright

Defence R&D Canada warrants that the work was performed in a professional manner conforming to generally accepted practices for scientific research and development.

This report is not a statement of endorsement by the Department of National Defence or the Government of Canada.

Defence R&D Canada – Ottawa

External Client Report
DRDC Ottawa ECR 2008-218
October 2008

Principal Author

Original signed by Paris W. Vachon

Paris W. Vachon

Defence Scientist

Approved by

Original signed by Pierre Lavoie

Pierre Lavoie

Chief Scientist

Approved for release by

Original signed by Pierre Lavoie

Pierre Lavoie

Head, Document Review Panel

This report is the Final Report deliverable under ESTEC Contract No. 21303/07/NL/CB.

- © Her Majesty the Queen in Right of Canada, as represented by the Minister of National Defence, 2008
- © Sa Majesté la Reine (en droit du Canada), telle que représentée par le ministre de la Défense nationale, 2008

Abstract

This document is the Final Report deliverable under ESTEC Contract No. 21303/07/NL/CB “GMES Sentinel-1 analysis of marine applications potential (AMAP)”. The document includes ship detectability modelling that has been carried out for Sentinel-1, including development of a ship detectability tool that applies to Sentinel-1, RADARSAT-1, RADARSAT-2, and Envisat ASAR image data. Limitations of the tool’s predictions are discussed, and examples from RADARSAT-1 and Envisat ASAR are provided to illustrate the performance of the tool. Also considered is Sentinel-1’s expected capability for other maritime applications, including iceberg detection, wind retrieval, oil spill detection, sea ice surveillance, and ship wake detection. In general, the Interferometric Wide Swath mode with its high spatial resolution and 250 km swath will be a useful mode for maritime surveillance in the littoral zone.

Résumé

Le présent document constitue le rapport final à présenter conformément au contrat du CERS no 21303/07/NL/CB visant l’analyse, dans le cadre de la mission Sentinel-1 du GMES, du potentiel relatif à certaines applications maritimes. Il comprend une modélisation de la capacité de détection de navires effectuée aux fins de la mission Sentinel-1, dont la conception d’un outil de prévision de la capacité de détection de navires pouvant utiliser des données d’imagerie recueillies par les RSO des satellites Sentinel-1, RADARSAT-1, RADARSAT-2 et Envisat. Il porte notamment sur les limites des prévisions de l’outil et comprend des exemples obtenus au moyen des RSO de RADARSAT-1 et d’Envisat, afin d’illustrer le rendement de l’outil. On y traite aussi de la capacité prévue de Sentinel-1, en ce qui concerne d’autres applications maritimes, dont la détection d’icebergs, l’extraction des vents, la détection des déversements de pétrole, la surveillance des glaces de mer et la détection du sillage de navires. En général, le mode d’interférométrie à fauchée large, dont la résolution spatiale est élevée et la fauchée mesure 250 km, se prête à la surveillance maritime dans les zones littorales.

This page intentionally left blank.

Executive summary

GMES Sentinel-1 Analysis of Marine Applications Potential (AMAP)

**Paris W. Vachon; John Wolfe; DRDC Ottawa ECR 2008-218; Defence R&D
Canada – Ottawa; October 2008.**

Introduction: The ESA Sentinels are operational satellites that will support the Global Monitoring for Environment and Security (GMES) program. The Sentinel-1 mission will consist of a constellation of two satellites that will carry C-band synthetic aperture radar (SAR). These radars will support a variety of applications including maritime surveillance. Whereas Sentinel-1 will have several modes of operation, the focus of this work has been on the Interferometric Wide (IW) mode with its 250 km swath, 5x20 metre spatial resolution (ground-range by azimuth, worst case), a single look, and selectable dual polarization (i.e., HH+HV or VV+VH). IW is expected to be the default mode of operation in the littoral zone. Performance of the IW mode for maritime surveillance applications, including ship detection, iceberg detection, wind retrieval, oil spill detection, sea ice detection, and ship wake detection has been compared to current operational practice with RADARSAT-1 and Envisat ASAR.

Results: The focus of this work is on ship detectability modelling, which has been carried out for Sentinel-1, including development of a ship detectability performance tool that applies to Sentinel-1, RADARSAT-1, RADARSAT-2, and Envisat ASAR image data. The tool assumes straightforward, pixel-based detection of ship targets in background ocean clutter and includes separate elements describing the ship radar cross section, the ocean clutter, and the radar system noise. Limitations of the tool, including the impacts of target motion, are discussed, and are included in the tool through a user-selectable margin parameter. Examples from RADARSAT-1 and Envisat ASAR are provided to demonstrate the performance of the tool.

Ship detectability modelling has shown that, due to its spatial resolution and range of incidence angles, IW mode is very well-suited to ship detection, almost regardless of the available polarization. HH polarization is the best of the co-polarization choices, with cross-polarization improving performance at smaller incidence angles. Operational use of two polarizations would improve the detection performance or could be used to reject false alarms.

Other maritime applications were also evaluated based upon backscatter models and imagery from RADARSAT-1 or Envisat ASAR. It is apparent that IW will be well suited to: iceberg detection and ship/iceberg discrimination; wind retrieval, though smaller incidence angles would be better; oil spill detection, though smaller incidence angles would be better; sea ice surveillance, though a larger swath would be desirable; and ship wake detection, though smaller incidence angles would be better.

As a general statement, the one-size-fits-all approach that will be adopted with Sentinel-1 IW operations will suit most maritime applications in the littoral zone rather well.

Significance: This document is the Final Report deliverable under ESTEC Contract No. 21303/07/NL/CB “GMES Sentinel-1 analysis of marine applications potential (AMAP)”.

This page intentionally left blank.

Sommaire

GMES Sentinel-1 Analysis of Marine Applications Potential (AMAP)

Paris W. Vachon; John Wolfe; DRDC Ottawa ECR 2008-218; R & D pour la défense Canada – Ottawa; Octobre 2008.

Introduction : Les satellites Sentinel de l'ASE sont des engins opérationnels qui appuieront le programme GMES (Global Monitoring for Environment and Security – surveillance mondiale pour l'environnement et la sécurité). La mission Sentinel-1 est fondée sur une constellation de deux satellites dotés de radars à synthèse d'ouverture (RSO) en bande C, lesquels appuieront diverses applications, dont la surveillance maritime. Bien que la mission Sentinel-1 implique plusieurs modes de fonctionnement, elle est axée sur le mode d'interférométrie à fauchée large, d'une fauchée de 250 km, d'une résolution spatiale de 5 m sur 20 m (distance au sol d'après l'azimut, dans le pire des cas), à visée unique et à polarisation double (soit HH+HV ou VV+VH). Ce mode d'interférométrie devrait être le mode de fonctionnement par défaut dans la zone littorale. Son rendement à des fins de surveillance maritime, dont la détection d'icebergs, l'extraction des vents, la détection des déversements de pétrole, la détection des glaces de mer et la détection du sillage de navires, a été comparé à celui des modes de fonctionnement courants avec les RSO de RADARSAT-1 et d'Envisat.

Résultats : Les présents travaux sont axés sur la modélisation de la capacité de détection de navires effectuée dans le cadre de la mission Sentinel-1, dont la conception d'un outil de prévision de la capacité de détection de navires pouvant utiliser des données d'imagerie recueillies par les RSO des satellites Sentinel-1, RADARSAT-1, RADARSAT-2 et Envisat. L'outil se base sur la détection simple par pixels de navires ciblés au sein d'un fouillis d'échos dans l'océan et comprend des éléments distincts décrivant la section efficace en radar des navires, le fouillis d'échos dans l'océan et le bruit du radar. Les limites de l'outil, dont l'incidence du déplacement des cibles, sont abordées dans le présent document et prises en considération par l'outil, par le biais d'un paramètre de marge que l'utilisateur peut choisir. Des exemples obtenus au moyen des RSO de RADARSAT-1 et d'Envisat sont présentés, afin de démontrer le rendement de l'outil.

La modélisation de la capacité de détection de navires a montré qu'en raison de sa résolution spatiale et de son éventail d'angles d'incidence, le mode d'interférométrie à fauchée large se prête bien à la détection de navires, peu importe la polarisation disponible, ou presque. La polarisation double HH est la meilleure, la polarisation croisée améliorant la performance à des angles d'incidence inférieurs. L'utilisation opérationnelle de deux polarisations pourrait améliorer la capacité de détection ou servir à éviter de fausses alarmes.

D'autres applications maritimes ont été évaluées d'après des modèles de rétrodiffusion et des images produites par les RSO de RADARSAT-1 ou d'Envisat. L'interférométrie à fauchée large se prêtera manifestement bien à la détection d'icebergs, à la distinction des icebergs et des navires, à l'extraction des vents (des angles d'incidence inférieurs seraient préférables), à la détection des déversements de pétrole (des angles d'incidence inférieurs seraient préférables), à la

détection des glaces de mer (une fauchée plus large serait préférable) et à la détection du sillage de navires (des angles d'incidence inférieurs seraient préférables).

En général, l'approche uniformisée qui sera utilisée pendant les opérations d'interférométrie à fauchée large de la mission Sentinel-1 se prêtera assez bien à la plupart des applications maritimes dans la zone littorale.

Importance : Le présent document constitue le rapport final à présenter conformément au contrat du CERS no 21303/07/NL/CB visant l'analyse, dans le cadre de la mission Sentinel-1 du GMES, du potentiel relatif à certaines applications maritimes.

Table of contents

Abstract	i
Résumé	i
Executive summary	iii
Sommaire	v
Table of contents	vii
List of figures	ix
List of tables	xi
Acknowledgements	xii
1 Introduction.....	1
1.1 Maritime surveillance requirements	1
1.2 Outline of document	2
2 Sentinel-1 description	4
2.1 Other sensors of interest	5
3 Ship detectability	8
3.1 Problem description.....	8
3.2 Ship detection model	9
3.2.1 System noise	9
3.2.2 Ocean clutter	10
3.2.3 Ship RCS and its variability	11
3.2.4 Model implementation	16
3.2.5 Model caveats	18
3.2.5.1 Relative versus absolute model performance	18
3.2.5.2 Inter-look coherence	19
3.2.5.3 Image pre-processing to enhance ship targets	19
3.2.5.4 Impulse response location and target motion	19
3.2.5.5 Ship signature size and spatial resolution.....	24
3.2.5.6 False alarm rate reduction.....	25
3.3 Minimum detectable ship length	26
3.4 Model sensitivity analysis	27
3.5 Implications for Sentinel-1	35
4 Other maritime applications.....	36
4.1 Iceberg detection	36
4.1.1 Problem description	36
4.1.2 Implications for Sentinel-1	36
4.2 Wind retrieval.....	36
4.2.1 Problem description	36

4.2.2	Implications for Sentinel-1	38
4.3	Oil spill detection	38
4.3.1	Problem description	38
4.3.2	Implications for Sentinel-1	40
4.4	Sea ice surveillance	42
4.4.1	Problem description	42
4.4.2	Implications for Sentinel-1	45
4.5	Ship wake detection.....	46
4.5.1	Problem description	46
4.5.2	Implications for Sentinel-1	48
5	Conclusions.....	49
5.1	Future work to consider.....	50
	References	51
	Annex A .. SAR Ship Detectability Performance Tool	55
A.1	Sensor-Specific Ship Detectability Calculator	58
A.2	Sensor-Specific Full Swath Analysis	62
A.3	Generic Ship Detectability Calculator.....	65
A.4	Ship Detectability Sensitivity Analysis	65
	Annex B .. Examples from Envisat ASAR and RADARSAT-1	69
B.1	Case 1 – ASAR dual polarization HH+HV, low incidence angle	70
B.2	Cases – ASAR dual polarization HH+HV, medium incidence angle	71
B.3	Case 3 – ASAR dual polarization HH+HV, high incidence angle	71
B.4	Case 4 – ASAR dual polarization HH+VV, small ships	71
B.5	Case 5 – ASAR dual polarization VV+VH.....	71
B.6	Case 6 – RADARSAT-1 ScanSAR Narrow.....	71
	List of acronyms	81

List of figures

Figure 1: Illustration of the ship detection problem in which the clutter PDF (blue) and the ship PDF (red) overlap, with the solid black line representing the threshold that sets P_{FA} and P_D	8
Figure 2: Plots of ocean clutter level as a function of polarization, wind speed, and wind direction, along with a plot of the noise floor for a RADARSAT-1 SCW product.	9
Figure 3: K-distribution order parameter as a function of wind speed for open ocean conditions.....	12
Figure 4: ECDFs as a function of polarization for Envisat ASAR data: a) all data; b) zoom-in on the lower tail.....	15
Figure 5: 10 th and 20 th percentile values of the ECDFs as a function of ENL for Envisat ASAR data.	16
Figure 6: Visualization of I_c for the case of $P_{FA} = 2.5(10)^{-9}$	18
Figure 7: Doppler suppression of the azimuth impulse response peak.	21
Figure 8: Cross-range velocity suppression of the azimuth impulse response peak.	22
Figure 9: Radial acceleration suppression for a wave of slope (A/Λ)	23
Figure 10: Range smearing due to target radial velocity.	25
Figure 11: Minimum detectable ship length for Sentinel-1 low orbit HH (blue) and RADARSAT-1 (red).	28
Figure 12: Minimum detectable ship length for Sentinel-1 low orbit HH (blue) and Envisat ASAR HH (green).	28
Figure 13: Minimum detectable ship length for Sentinel-1 low orbit HV (blue) and RADARSAT-1 (red).	29
Figure 14: Minimum detectable ship length for Sentinel-1 low orbit HV (blue) and Envisat ASAR HV (green).	29
Figure 15: Minimum detectable ship length as a function of: a) wind speed; b) wind direction; c) model margin; d) order parameter; and e) probability of false alarm.	32
Figure 16: Wind retrieval sensitivity: a) clutter as a function of incidence angle; b) clutter sensitivity to incidence angle; c) clutter as a function of wind speed; d) clutter sensitivity to wind speed.	37
Figure 17: RADARSAT-1 SCNA C-band HH polarization ocean backscatter including an oil slick off the east coast of Canada: a) 30 Sept. 2004; b) 23 Nov. 2004.....	39
Figure 18: C-band ocean backscatter suppression by a thin layer of Oleyl Alcohol: a) VV; b) HH.....	41
Figure 19: C-band ocean backscatter suppression by IFO180, 20% emulsion: a) VV; b) HH.	41

Figure 20: C-band ocean backscatter suppression by a thin layer of Iranian Heavy crude oil: a) VV; b) HH.....	41
Figure 21: Swath having a CNR larger than 6 dB for a nominal noise floor of -24 dB	42
Figure 22: RADARSAT-1 SCW C-band HH polarization sea ice backscatter for smooth new ice: a) near Anticosti Island, 1 Feb. 2005; b) near Newfoundland, 15 Feb. 2005.....	43
Figure 23: C-band sea ice backscatter: a) VV; b) HH; c) HV.....	44
Figure 24: Lowest wind speed required to induce ice/ocean backscatter signature reversal.....	45
Figure 25: RADARSAT-1 image of a ship and its Kelvin wake (©Canadian Space Agency, 2001).	46
Figure 26: Envisat ASAR image of a ship and its wake (©European Space Agency, 2006): a) HH polarization turbulent wake; b) HV polarization wake signature. The arrows point to the wake features of interest.	47
Figure 27: Case 1 with HH (left) and HV (right). RGB = (HV, HH, HV). (Continued on next page.).....	72
Figure 28: Case 2 with HH (left) and HV (right). RGB = (HV, HH, HV). (Continued on next page.).....	73
Figure 29: Case 3 with HH (left) and HV (right). RGB = (HV, HH, HV). (Continued on next page.).....	74
Figure 30: Case 4 with Grenfell (left) and Quest (right). RGB = (VV, HH, VV). (Continued on next page.).....	76
Figure 31: Case 5 with VV (left) and VH (right). RGB = (VV, VH, VV). (Continued on next page.).....	77
Figure 32: Case 6 with a tanker (left) and a cargo ship (right). (Continued on next page.)	78

List of tables

Table 1: Nominal Sentinel-1 parameters.....	5
Table 2: Nominal RADARSAT-1 single beam parameters.	6
Table 3: Nominal RADARSAT-1 ScanSAR parameters.....	7
Table 4: Nominal Envisat ASAR parameters.....	7
Table 5: RCS fits and ECDF percentile values for Envisat ASAR data. (Continued on next page).	13
Table 6: Worst case radial acceleration peak suppression for several sea states for IW2 at mid swath.	24
Table 7: Minimum detectable ship length at mid swath for several scenarios.	30
Table 8: Ship detectability – sensitivity to wind speed (U).....	33
Table 9: Ship detectability – sensitivity to wind direction (ϕ).	33
Table 10: Ship detectability – sensitivity to model margin (M).....	33
Table 11: Ship detectability – sensitivity to order parameter (v).....	33
Table 12: Ship detectability – sensitivity to incidence angle (θ).....	33
Table 13: Ship detectability – sensitivity to polarization state (P), orbit altitude, and probability of detection (P_D).....	34
Table 14: Ship detectability – sensitivity to probability of false alarm (P_{FA}).....	34
Table 15: Ship detectability – sensitivity to sensor parameters (ξ).	34
Table 16: Ship detectability – trading ρ_{SR} for ENL.	35
Table 17: Supported beam modes for each Sensor.....	55
Table 18: Glossary of parameters presented when using the SAR ship detectability performance tool.	56
Table 19: Demonstration products – case studies.	69
Table 20: Demonstration products – ship detectability tool inputs and outputs.....	70

Acknowledgements

The authors thank Dr. Evert Attema (ESTEC) for the opportunity to carry out the project described in this document. We are also grateful to the following individuals for provision of technical information and for helpful discussion: Dr. Evert Attema (ESTEC); Mr. Keith Beckett (MDA); Dr. François Charbonneau (CCRS); Dr. Roger DeAbreu (CIS); Mr. Dean Flett (CIS); Dr. Robert Hawkins (CCRS); Dr. Tony Luscombe (MDA); Dr. Peter Meadows (BAE); Dr. Betlem Rosich (ESRIN); and Dr. Paul Snoeij (ESTEC). The Envisat ASAR imagery used in this project are copyright ESA and were obtained through AO project 255. The RADARSAT-1 imagery used in this project are copyright CSA.

1 Introduction

The ESA Sentinels are operational satellites that will support the Global Monitoring for Environment and Security (GMES) program [1]. The Sentinel-1 mission will consist of a constellation of two satellites that will carry C-band synthetic aperture radar (SAR). These radars will support a variety of applications including maritime surveillance.

A key question is: “What is the capability of Sentinel-1 for maritime surveillance and ship detection in particular?” In this project “GMES Sentinel-1 analysis of marine applications potential (AMAP)”, this question has been addressed by carrying out the following tasks:

1. Create a model for ship detection performance prediction based upon Vachon et al. (1997) [30] and extend the model based upon recent ship detection work by Vachon et al. [32] [34] [36] that also addresses ship detectability by the Envisat ASAR AP mode of operation;
2. Implement the model in Matlab® such that the performance of all Sentinel-1 modes are addressed and may be compared with the performance of RADARSAT-1, RADARSAT-2, and Envisat ASAR;
3. Develop demonstration products using RADARSAT-1 and Envisat ASAR data that are currently available at DRDC Ottawa; and
4. Address the capability of the Interferometric Wide (IW) mode and the other Sentinel-1 modes for iceberg detection, wind retrieval, oil spill detection, sea ice detection, and ship wake detection based upon the expected clutter-to-noise ratio, wind speed sensitivity, oil and ice backscatter, and available observational evidence.

This document is the Final Report project deliverable; it addresses items 1 through 4 of the above tasks.

1.1 Maritime surveillance requirements

There is a vast literature that addresses the role of SAR in the ocean environment, e.g., [7], [12].

For maritime surveillance applications, wide swath coverage is generally required to maximize the rate of area coverage. This requirement is fundamental.

Ship detection relies on the detection of bright point-like targets against an ocean clutter background. The ocean clutter level is influenced predominantly by the local wind speed, which generates centimetre-scale Bragg scattering waves or “roughness” on the ocean surface. The higher the wind, the rougher the surface, and the higher the ocean clutter level. In fact, radiometrically calibrated radar can be used to retrieve high resolution wind fields. However, the clutter is also subject to local modulations from various physical processes, such as local wind speed variations, wakes, and atmospheric turbulence. Oceanographic modulations due to (oceanic) internal waves, current shear, and the presence of surfactants that damp the surface

roughness, also affect the clutter. Ship detection is most effective when the ocean clutter level is low. The clutter decreases with increasing incidence angle.

Iceberg detection is closely related to ship detection. Iceberg signatures tend to have different shapes and wake characteristics than those of ships, and different signatures as a function of radar polarization.

Oil spill detection relies upon the suppression of clutter by the presence of oil. This means that the background clutter must be sufficiently above the instrument noise floor to allow clutter suppression to be observed. As the wind speed increases, the oil layer breaks up and the oil mixes downwards into the water column. Detection of ships in the vicinity of detected oil spills provides information that may be helpful to associate a polluter with a particular oil spill.

Sea ice surveillance requires measurement of the ice edge and classification of the ice type: smooth new, first year, and multi-year ice. The ice edge is more easily detected when the sea/ice contrast is large, that is, when the ocean clutter level is low, as occurs for larger incidence angles. Discrimination between ice types is also incidence angle dependent, with discrimination between ice types increasing with increasing incidence angle.

Observation of ship wakes is also of interest. The presence of a ship wake modulates the background clutter. Measurement of ship wake properties can allow estimation of the ship speed and course. Ship wakes are easier to detect if the clutter level is high, although the wake signature may be obliterated if the wind speed is too large.

There are several competing factors when trying to meet a maritime surveillance requirement with SAR. The key radar parameters are:

- Swath width;
- Incidence angle;
- Spatial resolution;
- Radiometric resolution; and
- Noise floor.

In this project, straightforward C-band radar backscatter models along with nominal radar parameters are used to evaluate the expected performance of Sentinel-1 for ship detection, wind retrieval, oil spill detection, sea ice surveillance, and wake detection.

1.2 Outline of document

Section 2 of this document includes a description of the Sentinel-1 modes and the nominal sensor characteristics that have been used. Also included are the nominal parameters of RADARSAT-1, RADARSAT-2, and Envisat ASAR, for comparison purposes. Section 3 considers ship detectability modelling, which leads to a minimum detectable ship length that permits intercomparison of various radars and modes. A parametric study shows the model sensitivity and several possible system design trade-offs. Section 4 focuses on iceberg detection, wind retrieval, oil spill detection, sea ice detection, and ship wake detection. Conclusions are offered

in Section 5. The Annexes contain a description of the ship detectability model as implemented in Matlab® and some model runs along with RADARSAT-1 and Envisat ASAR imagery of known ships.

2 Sentinel-1 description

Sentinel-1 will offer four modes of operation:

1. Strip Map (S) Mode offers six different beams with an 80 km swath, 5x5 metre spatial resolution (ground-range by azimuth, worst case), a single look, and selectable dual polarization (i.e., HH+HV or VV+VH);
2. Interferometric Wide (IW) Swath Mode is composed of three different beams providing a 250 km swath, 5x20 metre spatial resolution (ground-range by azimuth, worst case), a single look, and selectable dual polarization (i.e., HH+HV or VV+VH);
3. Extra-Wide (EW) Swath Mode is composed of five different beams providing a 400 km swath, 20x40 metre spatial resolution (ground-range by azimuth, worst case), a single look, and selectable dual polarization (i.e., HH+HV or VV+VH); and
4. Wave (W) Mode with 5x20 metre spatial resolution (ground-range by azimuth, worst case), a single look, selectable single polarization, and sampled images of 20x20 km every 100 km along the orbit track.

The Sentinel-1 mission philosophy is, to the extent possible, to operate continuously in a single mode over land and the coastal zone. The preferred mode is IW, with Wave Mode being used for open ocean areas. The focus of this work is on IW performance, with comments on the S and EW modes where applicable.

Sentinel-1 will be operated in a circular orbit with a reference altitude of 711 km relative to the WGS84 ellipsoid. However, there will be a slight orbit eccentricity with respect to the Earth centre; the satellite altitude will vary along the orbit by about 28 km. In order to minimize the number of pulse repetition frequency (PRF) changes, a roll steering law has been defined. The roll steering will reduce the slant-range variation along the orbit, leading to a changing incidence angle relative to a fixed point in the swath. In this work, the Sentinel-1 parameters at the extreme altitude points along the orbit, namely the low-orbit (697 km) and high-orbit (725 km) cases, have been modelled. The actual performance achieved at some other point along the orbit would lie between these two extremes.

Nominal mid-swath values for the relevant Sentinel-1 parameters are summarized in Table 1 in which θ_{Min} is the minimum incidence angle within the beam; θ_{Max} is the maximum incidence angle within the beam; ρ_A is the azimuth resolution; ρ_{SR} is the slant-range resolution; ENL is the equivalent number of independent looks; and NESZ is the noise-equivalent sigma-zero (worst case within the beam). For beam-oriented calculations, the actual noise floor and ground range resolution (both functions of the local incidence angle) are used. Detailed Sentinel-1 information has been compiled from available literature, including [1], [23], and [24], along with input from the ESA Technical Authority for this project.

Table 1: Nominal Sentinel-1 parameters.

<i>Beam</i>	<i>Low orbit (697 km)</i>						<i>High orbit (725 km)</i>					
	θ_{Min} [deg]	θ_{Max} [deg]	ρ_A [m]	ρ_{SR} [m]	<i>ENL</i>	<i>NESZ</i> [dB]	θ_{Min} [deg]	θ_{Max} [deg]	ρ_A [m]	ρ_{SR} [m]	<i>ENL</i>	<i>NESZ</i> [dB]
S1	20.0	26.3	4.9	1.5	1	-24.0	18.3	24.5	4.9	1.5	1	-24.4
S2	23.5	29.5	4.9	1.8	1	-23.4	21.8	27.7	4.9	1.8	1	-23.6
S3	29.3	34.8	4.9	2.3	1	-25.0	27.6	33.0	4.9	2.3	1	-24.7
S4	34.7	39.7	4.9	2.7	1	-23.6	33.0	38.0	4.9	2.7	1	-23.7
S5	39.6	44.1	4.9	3.0	1	-24.2	37.9	42.4	4.9	3.0	1	-23.4
S6	42.5	46.7	4.9	3.2	1	-24.4	40.8	45.0	4.9	3.2	1	-23.7
IW1	30.9	36.6	19.5	2.4	1	-24.1	29.2	34.9	19.5	2.4	1	-23.8
IW2	36.5	41.8	19.5	2.8	1	-23.6	34.8	40.1	19.5	2.8	1	-23.2
IW3	41.7	46.0	19.5	3.2	1	-23.6	40.0	44.2	19.5	3.2	1	-23.1
EW1	20.8	29.3	40.0	6.5	1	-25.8	19.0	27.5	40.0	6.5	1	-25.8
EW2	29.2	35.1	40.0	9.2	1	-27.2	27.4	33.3	40.0	9.2	1	-27.2
EW3	35.1	39.8	40.0	11.0	1	-27.2	33.3	38.0	40.0	11.0	1	-27.2
EW4	39.7	44.2	40.0	12.3	1	-25.6	38.0	42.5	40.0	12.3	1	-25.6
EW5	44.3	47.0	40.0	13.5	1	-32.3	42.5	45.2	40.0	13.5	1	-32.2

2.1 Other sensors of interest

Sentinel-1 performance will be considered in the context of RADARSAT-1, RADARSAT-2, and Envisat ASAR, with the relevant parameters for these sensors listed in Table 2 through Table 4. The SAR system information was derived from [5], [22], and [26].

RADARSAT-1 is an HH polarization instrument. As for Sentinel-1, nominal parameters (Table 2) are provided and the indicated noise floors are the worst case within the swath, unless written as “-25” in which case they are a nominal value. RADARSAT-1 has two ScanSAR modes (Table 3): ScanSAR Narrow (SCN) is composed of 2 (SCNA) or 3 (SCNB) beams with a nominal 300 km swath; ScanSAR Wide (SCW) is composed of 3 (SCWA) or 4 (SCWB) beams with a nominal 500 km swath.

RADARSAT-2 data are modelled with the RADARSAT-1 parameters for common (i.e., heritage) modes, but with the following polarization choices available for RADARSAT-2: selective single polarization (HH or VV) or dual polarization (HH+HV or VV+VH). The RADARSAT-2 noise floor is taken as 5 dB smaller than that of RADARSAT-1. The higher resolution and polarimetric modes offered by RADARSAT-2 have not been considered in this work.

Envisat ASAR offers selective single polarization (IMP product), alternating polarization (APP product) that trades radiometric resolution for polarization in a burst-mode of operation, and a wide swath mode (WSM) composed of 5 beams with a nominal swath width of 450 km (Table 4). For APP mode, the ground range resolution is traded for ENL for larger incidence angle beams.

Table 2: Nominal RADARSAT-1 single beam parameters.

Beam	θ_{Min} [deg]	θ_{Max} [deg]	ρ_A [m]	ρ_{SR} [m]	ENL	NESZ [dB]
S1	19.5	26.7	27.0	9.3	3.1	-25.7
S2	24.1	30.9	27.0	9.3	3.1	-24.4
S3	31.0	37.0	27.0	14.1	3.1	-26.5
S4	33.6	39.4	27.0	14.1	3.1	-26.4
S5	36.4	41.9	27.0	14.1	3.1	-25.8
S6	41.7	46.5	27.0	14.1	3.1	-25.7
S7	44.7	49.2	27.0	14.1	3.1	-25.8
F1	36.8	39.9	8.4	5.2	1	-25.0
F2	39.3	42.1	8.4	5.2	1	-23.9
F3	41.5	44.1	8.4	5.2	1	-25.4
F4	43.5	45.8	8.4	5.2	1	-25.8
F5	45.4	47.6	8.4	5.2	1	-25.0
W1	19.3	30.2	27.0	14.1	3.1	-24.3
W2	30.2	38.9	27.0	14.1	3.1	-23.9
W3	48.9	45.1	27.0	14.1	3.1	-23.6
EH1	49.0	53.4	27.0	14.1	3.1	-25
EH2	50.1	53.5	27.0	14.1	3.1	-25
EH3	51.2	54.6	27.0	14.1	3.1	-25
EH4	54.5	57.2	27.0	14.1	3.1	-25
EH5	55.6	58.2	27.0	14.1	3.1	-25
EH6	56.9	59.4	27.0	14.1	3.1	-25
EL1	10.4	21.9	27.0	9.3	3.1	-24.5

Table 3: Nominal RADARSAT-1 ScanSAR parameters.

Mode	θ_{Min} [deg]	θ_{Max} [deg]	ρ_A [m]	ρ_{SR} [m]	ENL	NESZ [dB]
SCNA						
W1	19.3	30.2	47.8	27.1	3.5	-24.3
W2	30.2	38.9	53.8	27.1	3.5	-23.9
SCNB						
W2	30.2	36.4	71.1	27.1	3.5	-23.9
S5	36.4	41.7	71.9	27.1	3.5	-25.8
S6	41.7	46.9	78.8	27.1	3.5	-25.7
SCWA						
W1	19.3	30.2	93.1	53.8	7.0	-24.3
W2	30.2	38.9	104.7	53.8	7.0	-23.9
W3	38.9	45.1	117.3	53.8	7.0	-23.6
S7	45.1	49.2	117.5	53.8	7.0	-25.8
SCWB						
W1	19.3	30.2	93.1	53.8	7.0	-24.3
W2	30.2	36.4	104.7	53.8	7.0	-23.9
S5	36.4	41.7	106.0	53.8	7.0	-25.8
S6	41.7	46.9	117.6	53.8	7.0	-25.7

Table 4: Nominal Envisat ASAR parameters.

Beam	θ_{Min} [deg]	θ_{Max} [deg]	ρ_A [m]	ρ_{SR} [m]	ENL	NESZ [dB]
IMP-IS1	15.0	22.9	22.1	9.6	3.95	-19.6
IMP-IS2	19.2	26.7	22.1	9.4	3.95	-19.6
IMP-IS3	26.0	31.4	22.1	11.8	3.95	-20.6
IMP-IS4	31.0	36.3	22.1	14.2	3.95	-19.0
IMP-IS5	35.8	39.4	22.1	15.8	3.95	-19.0
IMP-IS6	39.1	42.8	22.1	17.2	3.95	-21.2
IMP-IS7	42.5	45.2	22.1	18.5	3.95	-20.7
APP-IS1	15.0	22.9	27.7	9.7	1.76	-19.6
APP-IS2	19.2	26.7	27.7	9.6	1.73	-19.6
APP-IS3	26.0	31.4	27.7	12.1	2.25	-20.6
APP-IS4	31.0	36.3	27.7	14.3	2.66	-19.0
APP-IS5	35.8	39.4	27.7	16.0	3.30	-19.0
APP-IS6	39.1	42.8	27.7	17.2	3.78	-21.2
APP-IS7	42.5	45.2	27.7	18.4	3.73	-20.7
SS1	17.0	26.0	107.5	44.9	13.19	-19.9
SS2	26.0	31.5	107.5	54.4	13.21	-23.4
SS3	31.0	36.5	107.5	63.6	13.84	-21.8
SS4	36.0	39.0	107.5	73.6	13.77	-23.1
SS5	38.5	42.6	107.5	78.7	13.38	-25.4

3 Ship detectability

3.1 Problem description

In SAR imagery, ships are generally detected by using pixel-based algorithms that search for bright pixels against the ocean clutter background. Ship detection is most effective when the ocean clutter level is low and the spatial resolution of the sensor is high. Modelling ship detectability is a statistical problem that considers separate models for the system noise, the ocean clutter, and the ship radar cross section (RCS) and its variability (i.e., target fading) [30]. The detection problem is illustrated in Figure 1. The two distributions represent the clutter plus noise (on the left) and the ship RCS variability (on the right). The detection performance is generally parameterized by the probability of false alarm (P_{FA}) and the probability of detection (P_D). The area under the clutter plus noise distribution up to the detection threshold line is $(1 - P_{FA})$. The area under the ship RCS variability distribution down to the detection threshold line is P_D . A key requirement in a practical ship detection system is to choose the detection threshold such that P_{FA} is extremely small (e.g., $< 2.5(10)^{-9}$) and P_D is large (e.g., > 0.8). It is generally helpful to express the ship detection performance in terms of a ship length rather than a radar cross section, requiring a model for the relationship between ship RCS and ship length.

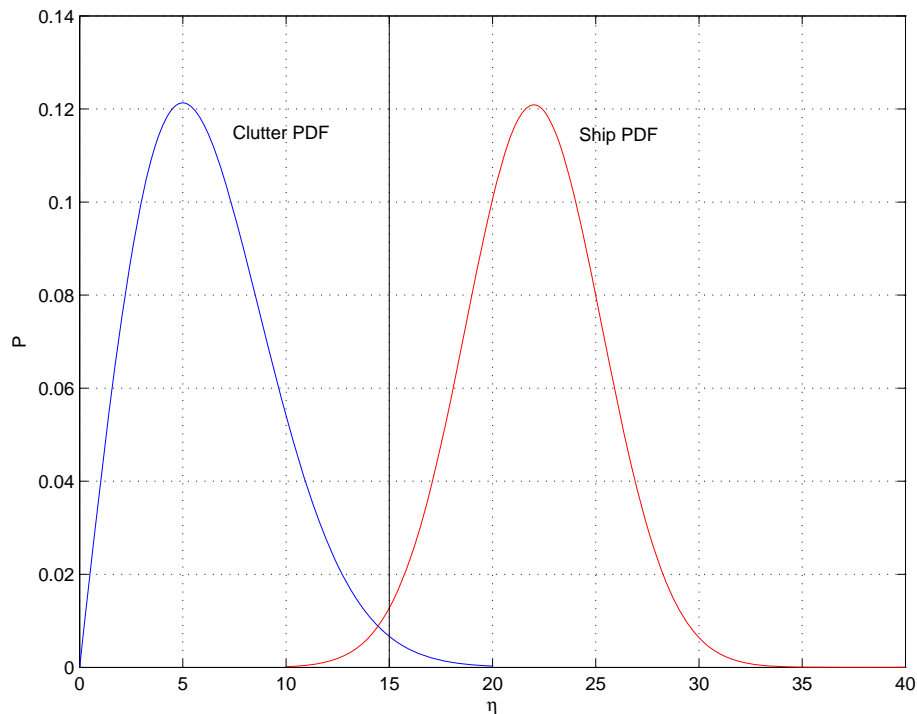


Figure 1: Illustration of the ship detection problem in which the clutter PDF (blue) and the ship PDF (red) overlap, with the solid black line representing the threshold that sets P_{FA} and P_D .

3.2 Ship detection model

In this section, a model for ship detectability is developed.

3.2.1 System noise

The system noise arises in the receiver and is modelled as additive Gaussian noise. However, it is generally expressed as a noise-equivalent normalized RCS, or NESZ (noise-equivalent sigma-zero), which depends upon the range to the scene, the incidence angle, and the elevation antenna pattern, among other things. NESZ is a useful concept since it can be compared directly with the observed backscatter level to establish the clutter-to-noise ratio (CNR). An example of an NESZ plot is shown in Figure 2. The NESZ is variable with range (lumpy in this example) due mainly to the shape of the elevation antenna pattern.

The system noise would be inverse-exponentially distributed for a single-look SAR system. Then, for a multi-look system, which may be characterized by its equivalent number of statistically independent looks (ENL), the noise becomes chi-squared distributed with $2 \times \text{ENL}$ degrees-of-freedom.

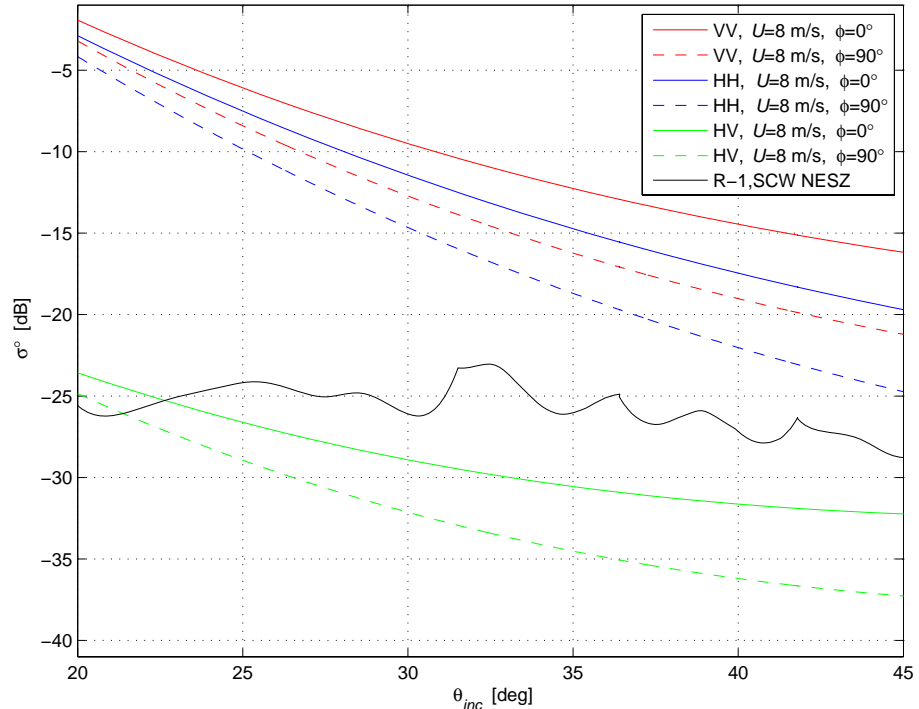


Figure 2: Plots of ocean clutter level as a function of polarization, wind speed, and wind direction, along with a plot of the noise floor for a RADARSAT-1 SCW product.

3.2.2 Ocean clutter

The ocean clutter level is influenced predominantly by the local wind speed, which generates centimetre-scale Bragg scattering waves or “roughness” on the ocean surface. The higher the wind, the rougher the surface, and the higher the ocean clutter level. However, the clutter is also subject to local modulations from various physical processes, such as local wind speed variations, wakes, and turbulence. Oceanographic modulations due to (oceanic) internal waves, current shear, and the presence of surfactants, which damp the roughness, also affect the clutter.

The normalized RCS (σ^0) or backscatter is a measure of the surface roughness. The ocean surface roughness is governed primarily by the local wind conditions. The normalized RCS can be used to estimate the wind speed at the ocean surface to high spatial resolution (1 km or better, as compared to resolutions on the order of 10 km, for a spaceborne scatterometer). By using principles from wind scatterometry, a semi-empirical model function may be used to estimate the surface wind speed from the observed normalized RCS, the local incidence angle, and the relative wind direction. The normalized RCS may be estimated directly from the SAR image; the local incidence angle is derived from the acquisition geometry. It remains a challenge to estimate the wind direction from SAR image data alone, but there are often useful indicators in the imagery such as boundary layer rolls, wind shadows, and wakes, or external sources of wind direction such as numerical weather prediction models, buoy observations, and scatterometers may be used.

In this work, the following models for the C-band normalized RCS (σ^0) of the ocean surface are considered. For VV polarization CMOD-IFREMER2, a C-band wind scatterometry model that was developed at IFREMER (France) for processing of archived ERS scatterometer data is used; for HH polarization a hybrid model composed of CMOD-IFREMER2 and a co-polarization ratio that is based upon Kirchhoff scattering is used. These models have been extensively discussed and validated in the RADARSAT-1 context, e.g., [31]. Representative clutter transects based upon this model are also shown in Figure 2.

Expressed in decibels, the clutter-to-noise ratio (CNR) for a particular wind speed, direction, and incidence angle is the difference between a particular normalized RCS curve and the noise floor. The CNR approaches zero decibels (i.e., equal clutter and noise contributions) for increasing incidence angles. Negative clutter-to-noise ratios indicate noise-limited imaging (i.e., the SAR image is dominated by system noise).

The CNR increases for increasing wind speed. For the same wind speed and direction, VV polarization will always have a larger CNR than HH polarization. For the same wind speed and polarization, an upwind or a downwind look direction (i.e., wind blowing towards or away from the radar) will always have a larger CNR than an across-wind look direction (i.e., wind blowing perpendicular to the radar look direction). The wind direction sensitivity is caused by the directional distribution of the Bragg-scale waves.

Cross polarization requires a further modification to the model. It is well-known that cross-pol clutter is extremely small and is generally expected to be near or below the noise floor of the instrument. An airborne SAR example is presented in [33]. For many spaceborne systems, it may be assumed that the cross-pol clutter level is zero such that ship detection is against the instrument noise floor rather than against the background clutter. Recent work with Envisat

ASAR AP mode data shows that there could be some cross-pol clutter signature at smaller incidence angles [36].

Based upon fitting to the data presented in [33], a very simple formulation for the cross-pol clutter has been developed as a correction to the VV polarization clutter:

$$\sigma^{\circ}_{VH} = \sigma^{\circ}_{HV} = \sigma^{\circ}_{VV}(U, \theta, \varphi) + 0.25 U + 0.22 \theta - 28.1 \quad [\text{dB}] \quad (1)$$

where U is the wind speed in m/s, θ is the local incidence angle in degrees, and φ is the relative wind direction (defined as zero blowing towards the radar). The correction is derived from clutter data that is limited to observations at two wind speeds (7 and 13 m/s) over a rather narrow incidence angle range (35° to 50°), and is assumed to be independent of wind aspect angle. However, the correction will be used to convert VV to cross-polarization clutter at all wind speeds and incidence angles considered. Representative cross-polarization clutter transects based upon this model modification are also included in Figure 2.

The K-distribution is used to describe the distribution of digital numbers in the image due to image fading (speckle) and local modulation of the mean clutter level by meteorological or oceanographic processes. The K-distribution includes two parameters: the ENL describes the speckle fading; the order parameter v describes the local modulation of the mean. For large order parameters, the K-distribution converges on the chi-squared distribution (i.e., the clutter becomes Gaussian). For small order parameters, the clutter becomes rather inhomogeneous, and the tail of the K-distribution becomes long.

A key problem is what order parameter to use for purposes of ship detectability modelling. Some empirical estimates of the order parameter from an ERS and RADARSAT-1 database of images taken over operational buoys are shown in Figure 3 [31]. Although it is desirable to model the order parameter as a function of the wind speed (e.g., the model shown as a blue line in the figure), in general, this sort of dependence is not observed. Although there appear to be fewer occurrences of large order parameters as the wind speed increases, it is seen that the order parameter can be small at any wind speed.

3.2.3 Ship RCS and its variability

There is rather little discussion of ship RCS in the open literature. In response to requirements to characterize RADARSAT-1's ship detection performance, a semi-empirical model was developed based upon a very limited number of observations of known ships [30]. The initial model was parameterized in terms of the ship length and the local incidence angle. The model applied to HH polarization only and was considered to provide a useful rule-of-thumb.

With the advent of automatic identification system (AIS), a mandated VHF transponder system for collision avoidance in commercial shipping, it has become feasible to generate very large databases of validated ship signatures. At DRDC Ottawa, shore-based commercial AIS data were obtained in conjunction with several RADARSAT-1 and Envisat ASAR trials [32] [34] [36], for compilation of a database of more than 4000 validated ship signatures that may be used to improve models of ship RCS and its variability.

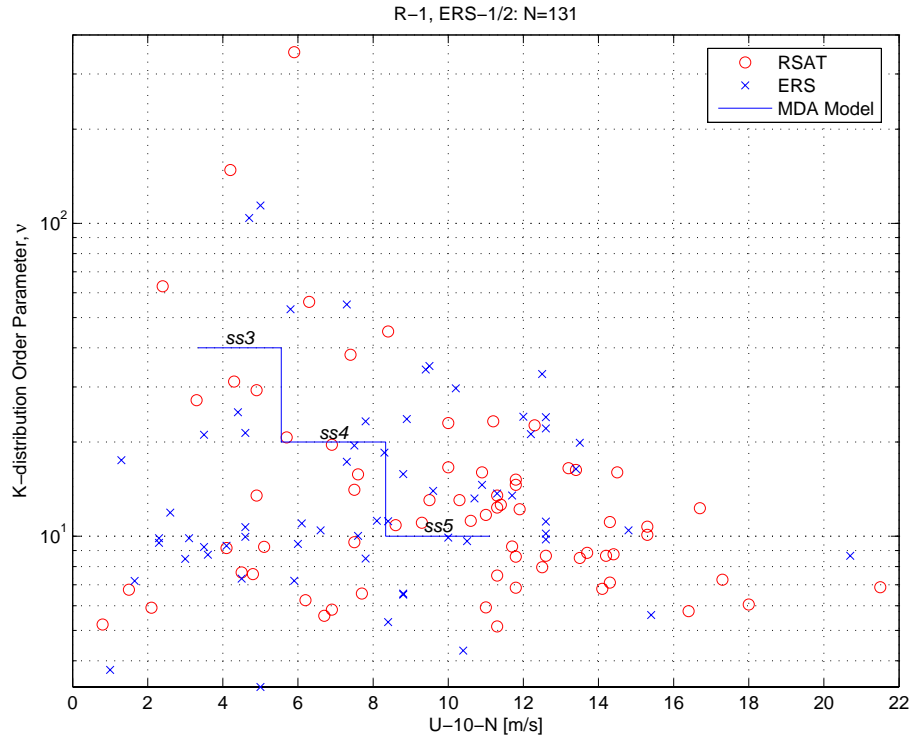


Figure 3: K-distribution order parameter as a function of wind speed for open ocean conditions.

For Sentinel-1 modelling, the focus is on Envisat ASAR ship signatures since they provide polarization information. The ship RCS data were evaluated to establish parametric dependencies [36]. The only strong correlation that was noted was on the ship length; no systematic dependence on incidence angle was observed.

Based upon the AIS database, the initial model for RADARSAT-1 data established a very simple relationship of the form:

$$\sigma = 1.25 L^2 \quad (2)$$

where σ is ship RCS in square metres and L is the ship length in metres. This model was very consistent with the earlier rule-of-thumb model, with the variability of the ship RCS normalized by equation (2) then describing the fading of the ship RCS due to un-modelled parameters such as ship aspect angle, local incidence angle, sea state, ship type, etc.

However, it was noticed that the resulting PDF did not have unity area or mean. For purposes of the Sentinel-1 analysis, the model fits to the Envisat ASAR data were re-visited such that the PDF was forced to have unity area and mean. This requirement was constrained by retaining the quadratic ship length dependence that was found previously. The generalized model is then described as:

$$\sigma_{PP} = A_{PP} L^2 \quad (3)$$

where A_{PP} is a fitted coefficient and PP represents the polarization (H or V) on transmit and receive. Values for A_{PP} are tabulated in Table 5 for the various polarization choices and with stratification of the data by ENL, which is range dependent for Envisat ASAR. In the Table, N is the number of samples available for each case, Co-Pol includes both HH and VV data, and Cross-Pol includes both HV and VH data.

To model the impact of the choice of P_D , the variability of the normalized ship RCS was used to establish the 10th and 20th percentile (10p and 20p) values. Numerous attempts were made to model the observed variability with simple probability density functions (PDFs) using goodness-of-fit tests [36]. Although the log-normal and Gamma distributions could fit the observed data, it was found that the fit in the vicinity of the tails of the distributions was variable and generally poor. Rather than use a fitted PDF, the observed empirical cumulative density function (ECDF), as plotted in Figure 4, was used instead. The 10p and 20p levels can be read off of these curves directly, as tabulated in Table 5. From the plots and the table, it can be noted that HH and VV have similar distributions, that VH and HV have similar distributions, and that the normalized RCS of the co-polarization channels is more dispersed than that of the cross-polarization channels.

As a check, the dependence on ENL was investigated. Such dependence seems possible since the variability could be a sampling issue related to ENL. The data appear in Table 5 and have been plotted in Figure 5. It could be argued that there is a slight dependence on ENL, but the difference between co-polarization and cross-polarization percentiles is much larger. As such, it was decided to model the normalized ship RCS PDF as independent of ENL and for simplicity, to focus only on the generic co-polarization and cross-polarization data, as appear in the highlighted lines of Table 5. For simplicity, only 10p and 20p levels, corresponding to $P_D = 0.9$ and $P_D = 0.8$, respectively, will be considered.

Table 5: RCS fits and ECDF percentile values for Envisat ASAR data. (Continued on next page).

*** Co-Pol ***				
ENL	<i>N</i>	<i>A</i>	10p	20p
ALL	1330	2.340	0.154	0.231
1.75	407	2.851	0.099	0.187
2.25	222	2.009	0.161	0.242
2.66	291	1.729	0.182	0.289
3.30	50	2.391	0.141	0.204
3.75	360	2.451	0.189	0.279

Table 5: Concluded.

*** Cross-Pol ***				
ENL	N	A	10p	20p
ALL	783	0.155	0.284	0.432
1.75	299	0.176	0.229	0.377
2.25	158	0.145	0.337	0.460
2.66	124	0.137	0.296	0.455
3.30	50	0.118	0.334	0.455
3.75	152	0.154	0.352	0.462
*** HH-Pol ***				
ENL	N	A	10p	20p
ALL	672	2.000	0.152	0.239
1.75	192	2.248	0.108	0.196
2.25	107	1.803	0.151	0.213
2.66	159	1.655	0.156	0.270
3.30	22	1.863	0.121	0.200
3.75	192	2.164	0.213	0.307
*** VV-Pol ***				
ENL	N	A	10p	20p
ALL	658	2.687	0.155	0.235
1.75	215	3.390	0.108	0.188
2.25	115	2.200	0.206	0.288
2.66	132	1.819	0.216	0.297
3.30	28	2.806	0.172	0.211
3.75	168	2.780	0.167	0.249
*** HV-Pol ***				
ENL	N	A	10p	20p
ALL	387	0.169	0.258	0.414
1.75	129	0.195	0.180	0.343
2.25	74	0.153	0.290	0.422
2.66	76	0.146	0.324	0.473
3.30	22	0.098	0.314	0.402
3.75	86	0.181	0.339	0.464
*** VH-Pol ***				
ENL	N	A	10p	20p
ALL	396	0.142	0.310	0.452
1.75	170	0.161	0.272	0.387
2.25	84	0.137	0.370	0.484
2.66	48	0.123	0.297	0.431
3.30	28	0.134	0.378	0.438
3.75	66	0.119	0.280	0.506

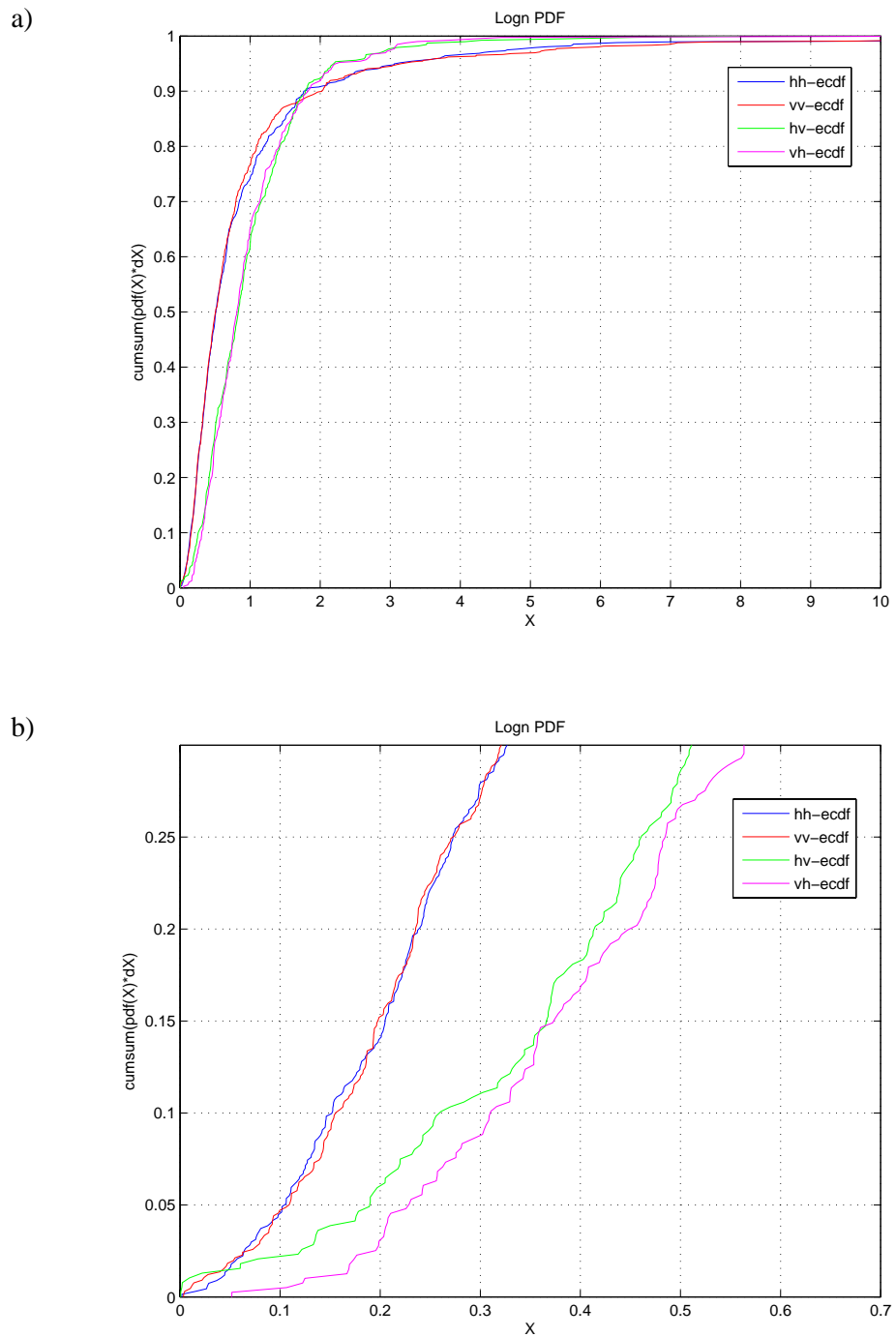


Figure 4: ECDFs as a function of polarization for Envisat ASAR data: a) all data; b) zoom-in on the lower tail.

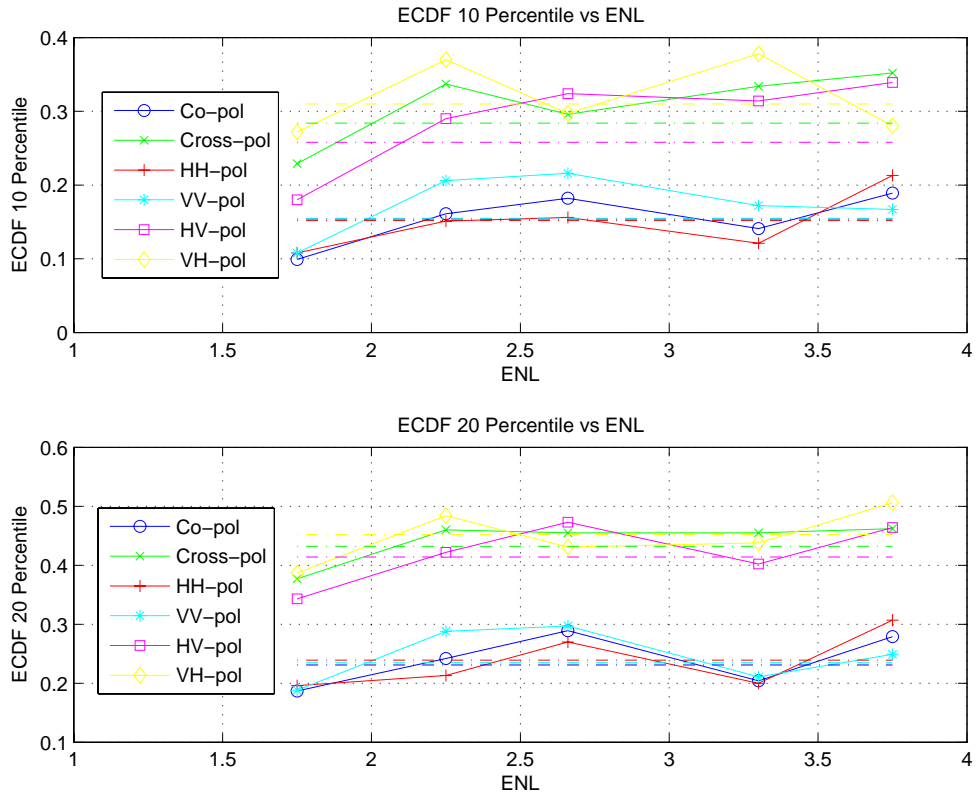


Figure 5: 10^{th} and 20^{th} percentile values of the ECDFs as a function of ENL for Envisat ASAR data.

3.2.4 Model implementation

The model elements are implemented as follows:

1. NESZ and ENL are used to model the noise floor and its PDF (P_n), which leads to a noise-only critical intensity I_{cn} that is a function of P_{FA} :

$$(1 - P_{FA}) = \int_0^{I_{cn}} P_n(x) dx \quad (4)$$

2. The wind speed, wind direction, incidence angle, polarization, ENL, and v are used to model the ocean clutter level and its PDF (P_c), which leads to a clutter-only critical intensity I_{cc} that is a function of P_{FA} :

$$(1 - P_{FA}) = \int_0^{I_{cc}} P_c(x) dx \quad (5)$$

3. The clutter and noise are assumed to be statistically independent such that the overall critical intensity is:

$$I_c = I_{cn} + I_{cc} \quad (6)$$

4. The critical intensity is scaled upward by dividing by the appropriate 10p or 20p threshold level (η_{PD}), which depend upon the radar polarization, and is then converted to a ship RCS (σ) based upon the radar resolution in azimuth (ρ_A) and ground range (ρ_{GR}):

$$\sigma = \frac{I_c \rho_A \rho_{GR}}{\eta_{PD}} \quad (7)$$

5. The ship RCS is adjusted upward by a margin of $M = 3$ dB to accommodate the possible impact of unmodelled factors that could degrade the peak target response, hence ship detectability (see Section 3.2.5);
6. The ship RCS is then converted to an equivalent ship length (L) as a function of the polarization:

$$L = \sqrt{\sigma / A_{pp}} \quad (8)$$

The critical intensity calculation is computationally intensive, thus a 3-dimensional critical intensity matrix was derived and stored in a look-up table as a Matlab® MAT-file. The 3-dimensions are represented by the order-parameter (v), ENL, and the significance level ($SigLev = 1 - P_{FA}$), all at high enough representative resolutions to ensure accurate estimation of the critical intensity level via interpolation. The dynamic ranges of these 3 parameters were configured with the intention of encompassing all meaningful requirements that might arise, as represented by the following Matlab® vectors:

$$\begin{aligned} v &= [2:0.5:20 \ 22:2:50 \ 60:10:100 \ 125 \ 1000]; \\ ENL &= [1:0.1:8 \ 8.5:0.5:15]; \\ SigLev &= 1.0 - [1(10)^{-1} \ 3(10)^{-2} \ 1(10)^{-2} \ 3(10)^{-3} \ 1(10)^{-3} \dots \ 3(10)^{-10} \ 1(10)^{-10}]. \end{aligned} \quad (9)$$

Other specific values may be established through interpolation within the matrix. A representative example is shown in Figure 6. It should be noted that this look-up table applies equally well to the noise-only (i.e., large v) and clutter-only cases.

The model has been implemented in Matlab® as ship detectability analysis tool, including a graphical user interface, as described in Annex A. All model plots and tables presented in this report were generated using the tool.

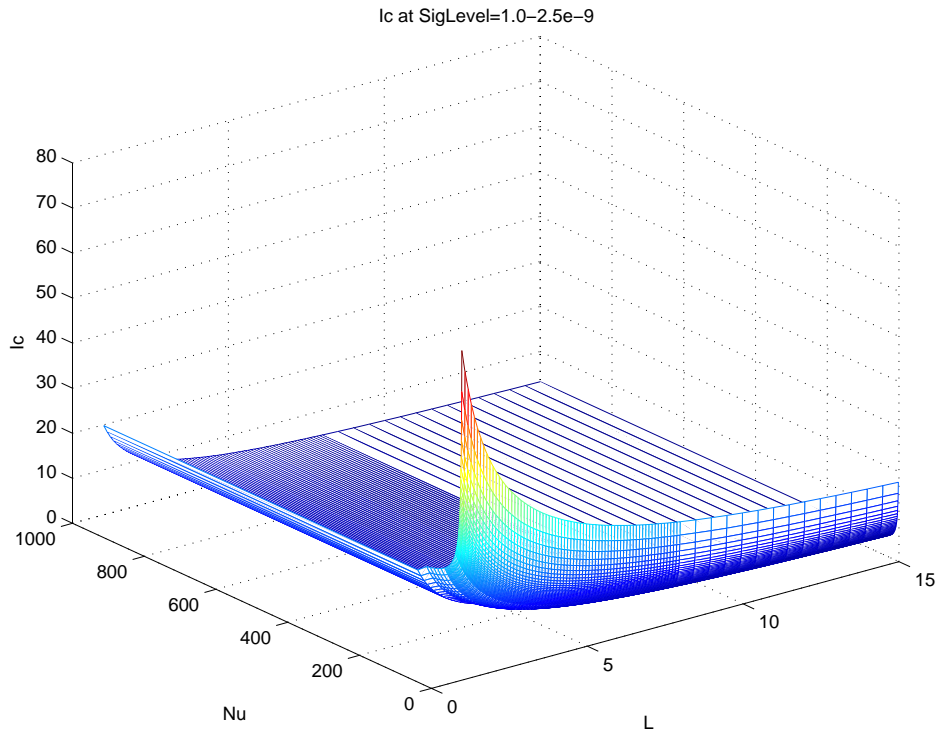


Figure 6: Visualization of I_c for the case of $P_{FA} = 2.5(10)^{-9}$.

3.2.5 Model caveats

3.2.5.1 Relative versus absolute model performance

Although the ship detection model provides an estimate of the minimum detectable ship length, it should be noted that this is a combined statistical and semi-empirical model, and not all factors have been or can be fully taken into consideration. Since the ship detection performance is largely based upon the clutter level and the SAR image quality, the model is expected to be quite adept at predicting the relative performance between beam modes or radars, all else being held equal. The minimum detectable ship lengths should be representative, but a generalized validation is extremely difficult, especially for smaller ships. Representative model predictions in the context of RADARSAT-1 and Envisat ASAR data are included in Annex B.

3.2.5.2 Inter-look coherence

It has been proposed that inter-look coherence techniques could help with the detection of smaller ships [17]. The premise is that each “look”, which arises from bandpass filtering of the Doppler spectrum, corresponds to a different observation time. In the “split-look” ship detection technique, two sub-apertures are used. Ship targets of interest should be correlated between looks, while the background clutter remains uncorrelated. This concept has been difficult to verify and quantify [8], probably due to target decorrelation caused by target motion and changes in the target aspect angle between the two looks. Nevertheless, a 0.9 dB improvement in contrast has been noted for low contrast targets, i.e., signal-to-noise ratio (SNR) < 15 dB [13].

Inter-look coherence techniques or other phase-based analysis methods are not included in the ship detection model. To zeroth order, their impact could be assessed through downward adjustment of the model margin. However, revision of the clutter model parameters might also be required.

3.2.5.3 Image pre-processing to enhance ship targets

Several pre-processing strategies have been proposed to enhance ship targets prior to detection, e.g., [27]. The impacts of these strategies are not included in the ship detection model. To zeroth order, their impact could be assessed through downward adjustment of the model margin. However, revision of the clutter model parameters might also be required.

3.2.5.4 Impulse response location and target motion

There are many other factors that will impact the ship signature peak value that have not been modelled, including where the peak value lies relative to the sampling grid and the effects of target motion, e.g., [21]. To get a handle on some of these factors it is assumed that the ship signature is a simple point target impulse response. The azimuthal impulse response of a moving point target may be written [29]:

$$g_a(t) = \frac{T^2}{\sqrt{4N^2 + (TB)^2 \hat{\eta}^2}} \exp\left(-\pi \frac{t_D^2}{V^2}\right) \exp\left\{-4\pi \frac{B^2}{4N^2 + (TB)^2 \hat{\eta}^2} \left[t + t_D \left(1 + \frac{\hat{\eta}}{2}\right)\right]^2\right\} \quad (10)$$

where t is the azimuth time, $T = R_o \beta / V$ is the coherent integration time, $B = 2V\beta/\lambda$ is the Doppler bandwidth, N is the number of looks (i.e., ENL), $t_D = (R_o/V)(v/V)$ scales the target radial velocity component v (defined as positive for target motion away from the radar), $\hat{\eta} = R_o a / V^2 - 2u / V$ scales the target cross-range velocity component u and the target radial acceleration component a (which is also positive away from the radar), $\beta = \lambda / 2\rho_A$ is the azimuth beamwidth, V is the platform velocity, λ is the radar wavelength, R_o is the slant range of closest approach, ρ_A is the 1-look azimuth resolution, Gaussian-shaped functions have been used to model the azimuth antenna pattern and the look extraction filters, and linear FM and matched filter processing is assumed. In equation (10), the first term is the peak value of the azimuthal

impulse response, the second term represents the effect of Doppler suppression, and the third term sets the shape and location of the azimuth impulse response. Strictly speaking, this formula is only correct for the flat Earth case since it contains the assumption that the spacecraft and footprint velocities are equal (the footprint velocity is usually 10% smaller than the spacecraft velocity), but it is useful since it allows certain parametric dependencies to be deduced by straightforward calculation or inspection.

3.2.5.4.1 Sampling grid

An actual SAR system samples the azimuthal impulse response at the pulse repetition frequency (PRF) $f_p \geq 2B$, where the lower limit arises from the sampling theorem. For a static target with $N = 1$, the worst case maximum-sampled value due to the location of the sampling grid relative to the location of impulse response peak value occurs at a temporal shift of one-half of a sample for the lowest sampling rate, i.e., at $t = 1/4B$. This corresponds to a worst-case reduction in the peak sampled value of -0.9 dB. This value would change for different azimuth antenna and matched filter patterns and if there is a margin built into the sampling design (i.e., the greater-than condition), but provides a guideline for the impact of changing the sampling grid location.

3.2.5.4.2 Doppler suppression

Doppler suppression arises when the Doppler spectrum of a moving target becomes shifted outside of the Doppler passband of the processor. The processor is generally designed under the assumption of a static scene. By inspection of equation (1) and for $N = 1$, the amount by which the peak of the impulse response is reduced is given by:

$$\exp\left(-\pi \frac{t_D^2}{T^2}\right) = \exp\left(-\pi \frac{v^2}{V^2} \frac{4\rho_A^2}{\lambda^2}\right) \quad (11)$$

which is plotted for nominal IW parameters (i.e., $V = 7.5$ km/s, $\lambda = 0.056$ m, $\rho_A = 19.5$ m) in Figure 7.

The radial velocity component could arise from rectilinear target motion in the range direction. To get a handle on the scale of the radial velocity component, consider a ship steaming at 18 knots (9.26 m/s). The ship's speed will be projected onto the range direction through the ship aspect angle. As a worst case, the ship will be moving in the range direction, either directly towards or away from the radar. In this case, the rangeward ship speed would then be projected onto the radial line of sight through the Sine of the local incidence angle. For Sentinel-1 IW mode, the incidence angle ranges from 31° to 46° , corresponding to radial velocity components of 4.8 m/s and 6.8 m/s, respectively, with 6.7 m/s as the worst case within the accessible IW swath. The worst case is reduced if the ship is not range travelling, and scales proportionately for other ship operating speeds. For example, for the same ship steaming at 24 knots (12.35 m/s), the worst case radial velocity component would be 8.9 m/s.

From the plot, it is apparent that for a quickly moving, range-travelling ship, Doppler suppression could reduce the peak response by 5 dB or more.

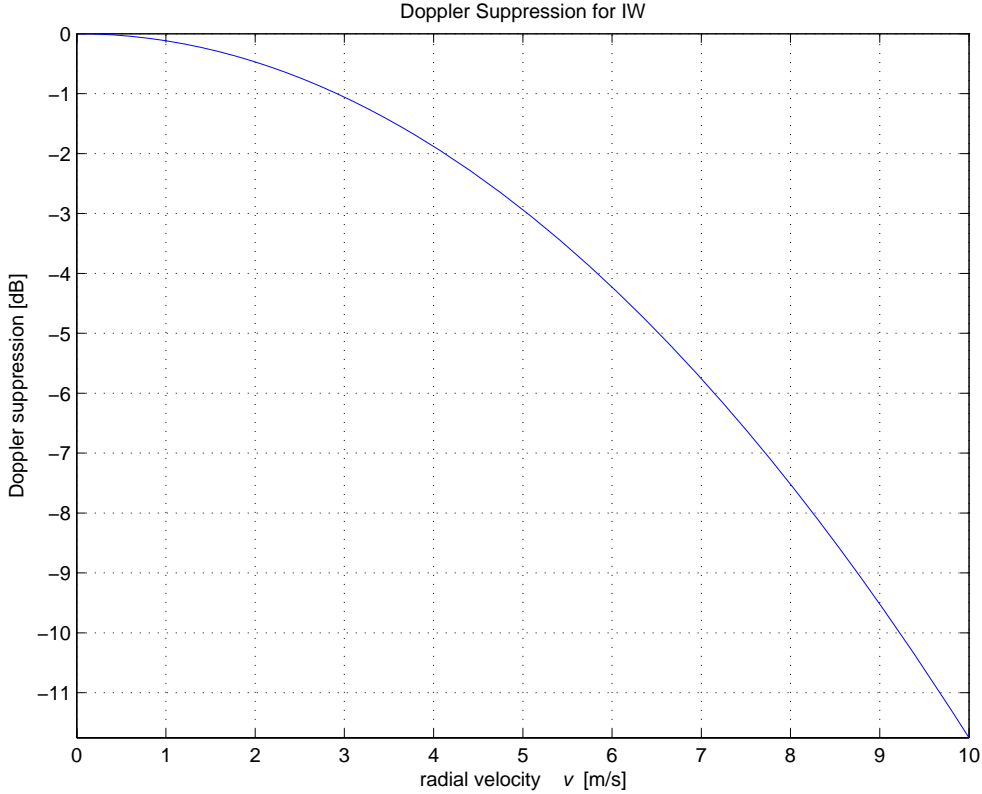


Figure 7: Doppler suppression of the azimuth impulse response peak.

3.2.5.4.3 Radial acceleration and cross-range velocity suppression

The impulse response and in turn the peak impulse response value will be suppressed by target radial acceleration and target cross-range velocity components. By inspection of equation (10) and for $N = 1$, the amount by which the peak of the impulse response is reduced due to these target motions is given by:

$$\delta = \frac{1}{\sqrt{1 + \left(\frac{TB}{2}\right)^2 \hat{\eta}^2}} = \frac{1}{\sqrt{1 + \left(\frac{R_o \lambda}{2\rho_A^2}\right)^2 \left(\frac{R_o a}{V^2} - \frac{2u}{V}\right)^2}} \quad (12)$$

The cross-range velocity component could arise from rectilinear target motion in the azimuthal direction. The effect is plotted for IW2 mid swath parameters (low-orbit case) in Figure 8. Cross-range velocity suppression only reduces the peak response by a few hundredths of a decibel for most practical ship speeds, so may be safely neglected.

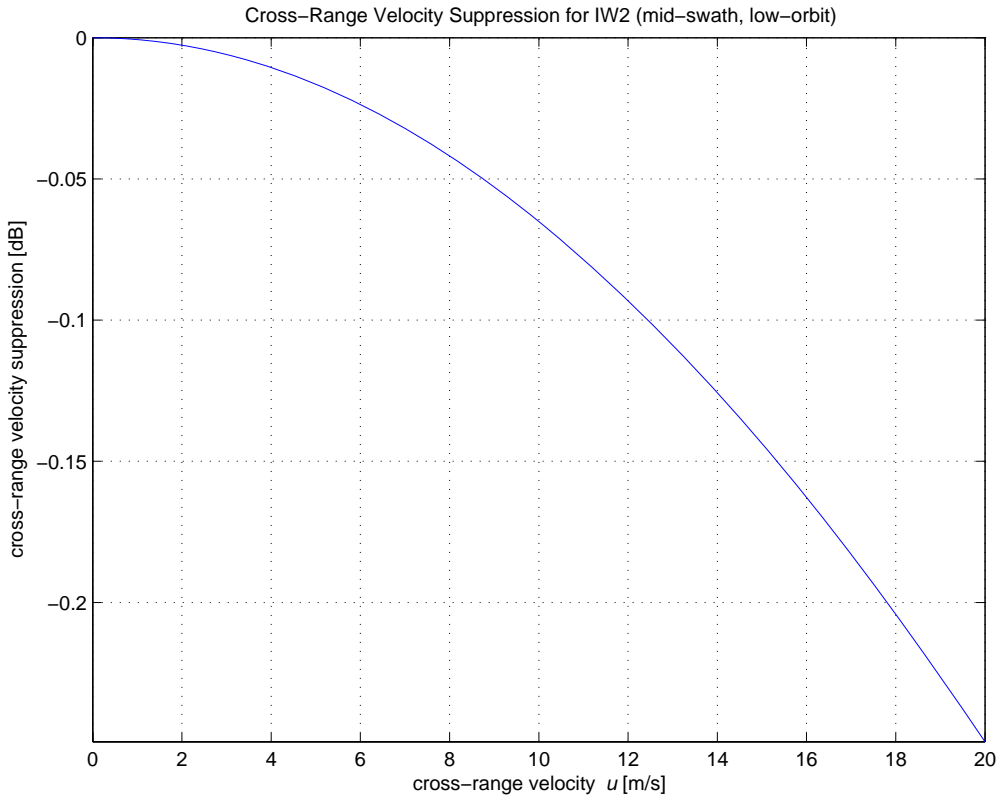


Figure 8: Cross-range velocity suppression of the azimuth impulse response peak.

A radial acceleration component could be imparted upon a ship that is advected by an underlying ocean wave system. Smaller ships would be more susceptible to this type of acceleration motion. As a worst case, consider a Sinusoidal wave that is travelling in the range direction. Then, it can be assumed that the maximum wave orbital acceleration is imparted upon the ship, amounting to:

$$a = \omega^2 A \quad (13)$$

where $\omega = \sqrt{gk}$ (i.e., the deep water ocean wave dispersion relationship), g is the acceleration due to gravity, $k = 2\pi/\Lambda$ is the wavenumber, Λ is the wave length, and A is the wave amplitude corresponding to a significant wave height (H_s) of $2A^2$. In practice, the radial component of the orbital acceleration would be reduced if the wave is other than range travelling. On the other hand, the acceleration could be increased if the ship is moving into the wave (i.e., increasing the encounter wave frequency). Also, depending upon the transfer function between the wave motion and the ship motion, it is likely that the orbital acceleration imparted on the ship will be smaller than that suggested by the worst case of equation (13), which is a function of where the ship lies along the wave during imaging. An inherent assumption in this analysis is that $L \ll \Lambda$, but for practical purposes it may be assumed that $L < \Lambda/4$.

From equations (12) and (13), the radial acceleration peak suppression may be written:

$$\delta = \frac{1}{\sqrt{1 + (\pi g \lambda)^2 \left(\frac{R_o}{V}\right)^4 \left(\frac{A}{\Lambda}\right)^2}} \quad (14)$$

where (A/Λ) is a measure of the wave slope, which in practical terms is limited to 1/24 (e.g., [19]). For IW2 parameters at mid swath (low orbit case), the worst case radial acceleration suppression is plotted in Figure 9. It is apparent that radial acceleration suppression could reduce the peak response by several decibels for shorter, higher frequency wave conditions.

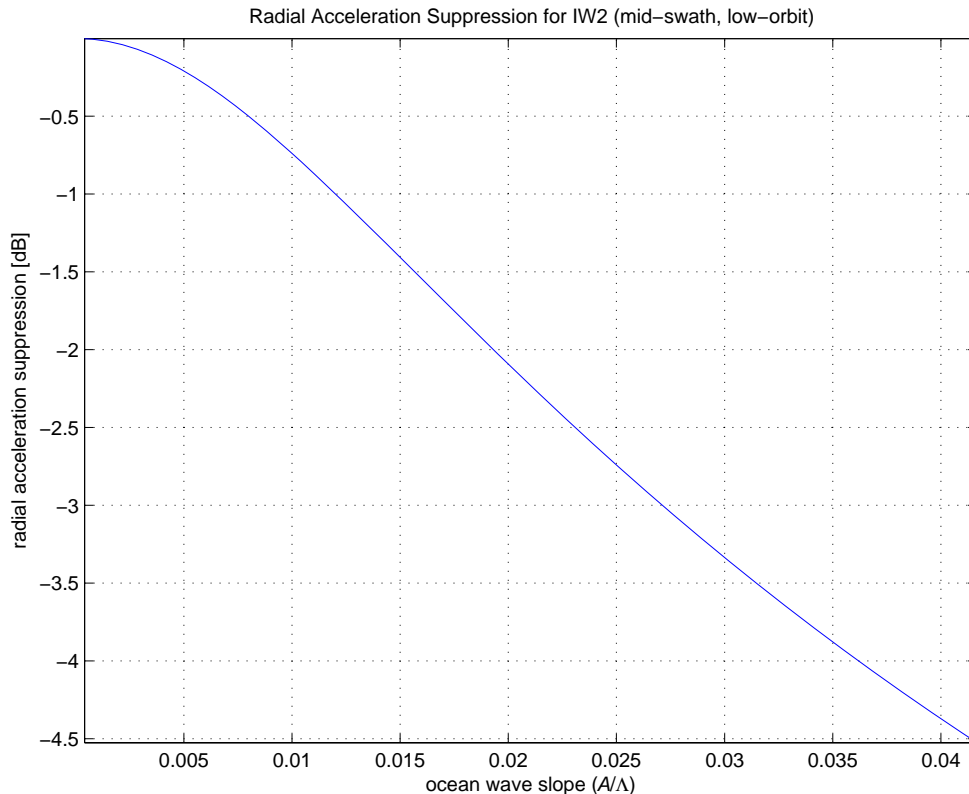


Figure 9: Radial acceleration suppression for a wave of slope (A/Λ) .

To better illustrate the effect, several cases derived from Figure 9 are presented in Table 6. It is apparent that radial acceleration suppression could cause a reduction of the impulse response peak value by several decibels.

A more complete analysis of the impact of wave-induced ship motion on SAR image focus would require an engineering analysis of the motion imparted on a ship by ocean waves, use of a realistic wave spectrum, and integration of the target motion during formation of the azimuth

aperture. Accelerating targets have been discussed in the literature for the case of generic acceleration terms [25] and for heave-induced ship motion [10], with the latter study showing improvements in peak response of 3 to 5 dB if target heave motion is taken into consideration. This is consistent with the scale of the radial acceleration peak suppression estimated here.

A [m]	H_s [m]	Λ [m]	(A/Λ)	L [m]	δ [dB]
1	2	100	0.01	< 25	-0.74
1	2	200	0.05	< 50	-0.21
2	8	100	0.02	< 25	-2.09
2	8	200	0.01	< 50	-0.74
3	18	100	0.03	< 25	-3.34

Table 6: Worst case radial acceleration peak suppression for several sea states for IW2 at mid swath.

3.2.5.4.4 Range smearing

So far only target motion impacts on the azimuthal impulse response have been considered. However, a target that is moving rapidly in the radial direction could pass through several slant-range resolution cells during the coherent integration time, causing the target to be smeared in the range direction, thus reducing the peak value of the impulse response. This effect is important if:

$$|vT| = \frac{R_o \lambda}{2\rho_A} \left| \frac{v}{V} \right| > \rho_{SR} \quad (15)$$

where ρ_{SR} is the slant-range resolution. For IW2 mid swath parameters (low orbit case) and $v = 10$ m/s, it is apparent that the maximum value of the left-hand side of equation (15) is around 1.7 m, in comparison to $\rho_{SR} = 2.8$ m. Therefore, range smearing should not significantly degrade the peak target value.

3.2.5.5 Ship signature size and spatial resolution

If the ship signature extends over several resolution cells, then the peak contrast could be reduced, which could in turn reduce vessel detectability. In principle, the best detection performance should arise if the resolution cell size matches the scale of the vessel that is being detected. The ship detection model assumes that the ship is restricted to a single resolution cell in spatial extent. This will rarely be the case, especially for radar such as that proposed for Sentinel-1, which has a rather high spatial resolution. However, many ship signatures are characterized by a single dominant scatterer. As such, the relative sizes of the ship signature and the resolution cell are not expected to be a limitation of the model.

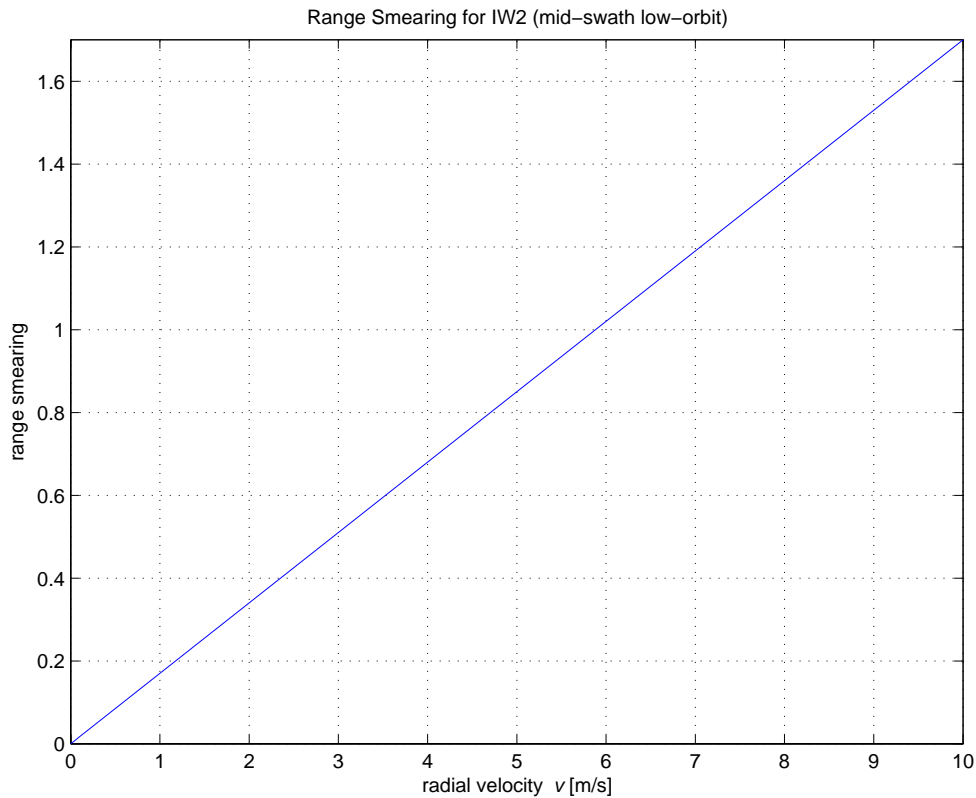


Figure 10: Range smearing due to target radial velocity.

3.2.5.6 False alarm rate reduction

Many practical ship detection systems employ false alarm rate reduction techniques to reject certain candidate ship signatures from further consideration. These techniques can include: target clustering, in which isolated targets are joined into a single target using target scale restrictions; estimation of the ship length for signatures that span multiple resolution cells; estimation of the target RCS in connection with the ship signature length (e.g., through models such as those in equations (2) or (3)); searching for a ship wake signature in the vicinity of the candidate ship signature as confirmation of a ship target; searching for the presence of azimuth and range ambiguities for each candidate ship target and rejecting target ambiguities that presented as candidate ship signatures; and validating candidate ship signatures using external operational ship information such as AIS data.

These false alarm rate reduction techniques could in effect reduce the false alarm, or increase the probability of missed detection. The impact of these false alarm rate reduction techniques has not been included in the ship detection model.

3.3 Minimum detectable ship length

The minimum detectable ship length calculations are based upon the following fixed parameter choices:

- $U = 12 \text{ m/s}$;
- $\varphi = 0^\circ$;
- $v = 4$;
- $P_{FA} = 2.5(10)^{-9}$;
- $P_D = 0.9$;
- $M = 3 \text{ dB}$;
- Co-pol and Cross-pol operation, with HH considered for co-pol.

The chosen wind speed is a representative case that corresponds roughly to sea state 5, and is an operational upper limit in which ship detection is desirable. A lower wind speed would result in better ship detection performance.

The chosen relative wind direction is for the case of wind blowing towards the radar. Towards and away from the radar are the worst clutter cases. Choice of a different wind direction would result in better ship detection performance.

The chosen order parameter is a fairly pessimistic case, but is a value that arises at all wind speeds. A larger order parameter would result in better ship detection performance.

The chosen probability of false alarm is rather low and represents less than one false alarm for a 500 km by 500 km scene. A higher false alarm rate permits the detection of smaller ships.

The chosen probability of detection represents the performance of a useful ship detection system. A lower probability of detection precludes the detection of smaller ships.

Some swath-oriented results from the minimum detectable ship length calculations are shown in Figure 11 through Figure 14. The fixed parameters used in each case are shown across the title of each plot. The plots use the actual ground range resolution and NESZ specific to each position in the swath. The plots are colour coded by sensor and include Sentinel-1 (blue), RADARSAT-1 (red), and Envisat ASAR (green). The beams are plotted alternately with solid and dashed lines for each sensor and the beam mode labels according to Table 1 through Table 4 are placed at the centre of each swath (some of the plots are quite busy). The same Sentinel-1 data results are plotted for the HH and HV cases for reference purposes. The curves for the HH case tend to be smooth and co-linear due to the clutter-limited imaging. The curves for the HV case follow the shape of the noise floor due to the noise limited imaging. A few cases have been tabulated at mid swath (39.1° incidence angle, low-orbit case) to permit a more detailed performance comparison (see Table 7).

By inspection of the table and the plots, the following is noted:

1. The minimum detectable ship length for the groups of single beam modes decreases with increasing incidence angle, which illustrates the importance of incidence angle in reducing the background ocean clutter level.
2. The minimum detectable ship length decreases for modes with increasing (i.e., smaller) resolution.
3. Comparison of the co-polarization and cross-polarization plots shows the impact of changing the polarization. For co-polarization, the ship RCS is larger, but the clutter level is higher, especially for smaller incidence angles. The co-polarization case is generally clutter limited. For cross-polarization the ship RCS is smaller, but the clutter is near or below the noise floor; the cross-polarization case is generally noise limited. There are significant benefits to using cross-polarization, especially for acquisitions at smaller incidence angles. Furthermore, cross-polarization provides more uniform ship detection performance across the image swath since the noise floor is somewhat independent of incidence angle.
4. Comparison of the co-polarization data for $P_D = 0.8$ and $P_D = 0.9$ shows how an increase in this parameter decreases the detection performance for smaller ships.
5. Considering Sentinel-1, due to the higher resolution, there is significantly better ship detection performance for IW than RADARSAT's SCNB, a mode that is being used for operational ship detection, over a comparable swath width. We also see that there is a penalty in using EW for its broader swath due to EW having coarser spatial resolution than IW.

3.4 Model sensitivity analysis

A sensitivity analysis was carried out to establish the impact of the input parameters. This is particularly useful since some of the inputs are not well known (e.g., the K-distribution order parameter). The baseline used for this analysis is IW2 at mid swath (low orbit case) with HH polarization and $P_D = 0.9$, along with the other nominal parameters that were used in the previous section. Perturbations to those parameters were used to arrive at a revised minimum detectable ship length and its local rate of change (if applicable). Figure 15 and Table 8 through Table 16 summarize the analysis results. In the tables, the highlighted rows indicate cases with the nominal parameters that were used in the model runs of the previous section.

Figure 15a) and Table 8 provide the model sensitivity to wind speed, showing how smaller ships may be detected at smaller wind speeds, and that the wind speed sensitivity increases with increasing wind speed. The wind drives the background clutter level, which increases with increasing wind speed.

Figure 15b) and Table 9 provide the model sensitivity to wind direction, showing how smaller ships may be detected for wind directions other than towards (0°) or away from (180°) the radar, with the greatest wind direction sensitivity at angles that lie between up-wind and cross-wind. The wind direction drives the background clutter level, which is maximum for the wind blowing towards or away from the radar, and is minimum for the wind blowing across the radar look direction.

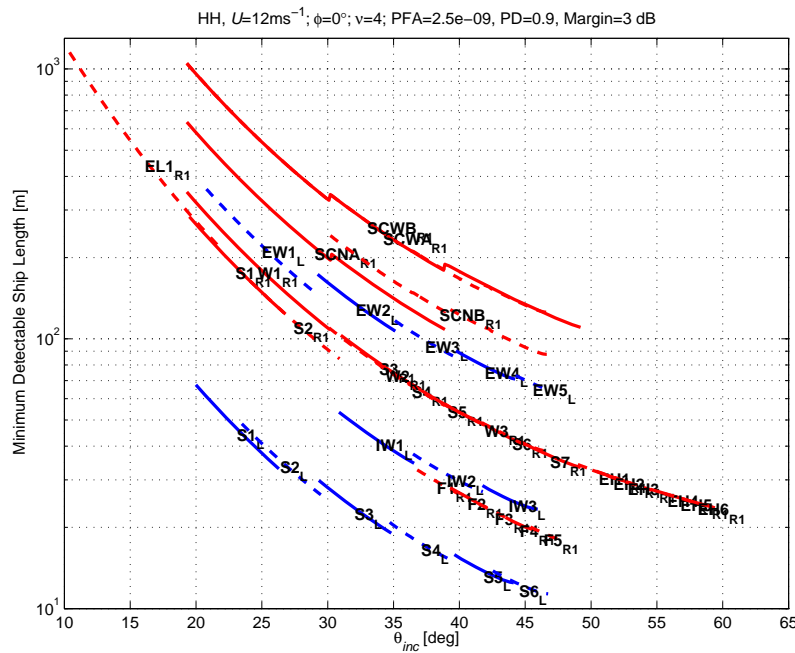


Figure 11: Minimum detectable ship length for Sentinel-1 low orbit HH (blue) and RADARSAT-1 (red).

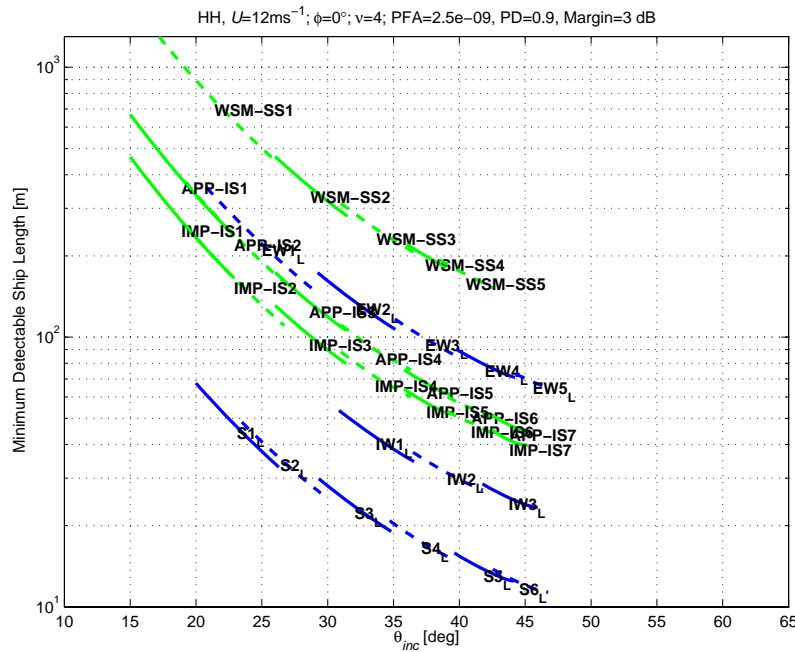


Figure 12: Minimum detectable ship length for Sentinel-1 low orbit HH (blue) and Envisat ASAR HH (green).

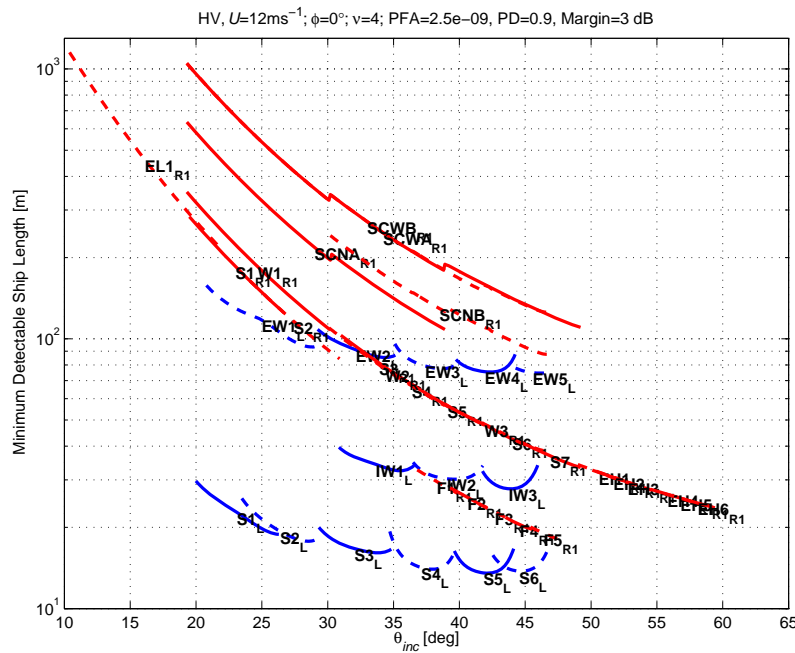


Figure 13: Minimum detectable ship length for Sentinel-1 low orbit HV (blue) and RADARSAT-1 (red).

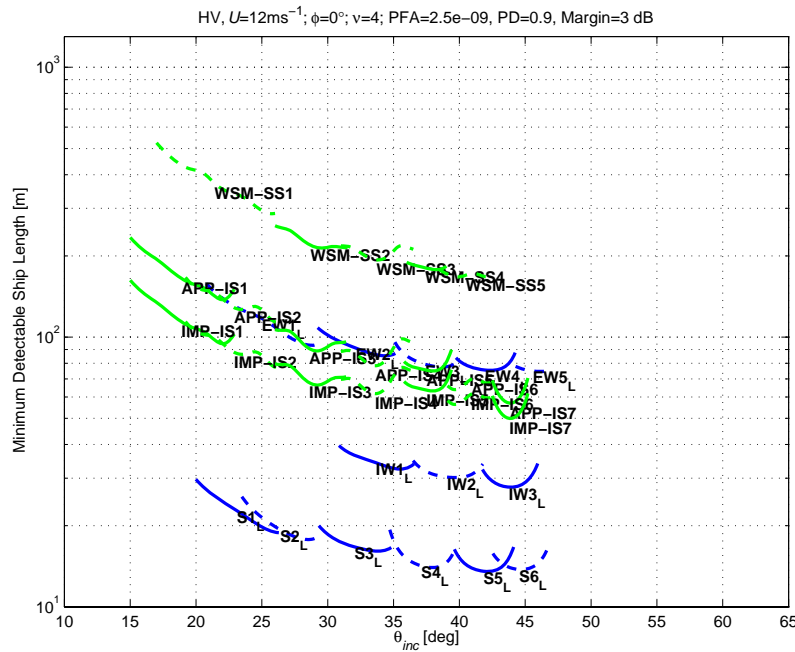


Figure 14: Minimum detectable ship length for Sentinel-1 low orbit HV (blue) and Envisat ASAR HV (green).

Table 7: Minimum detectable ship length at mid swath for several scenarios.

Sensor	Mode	HH $P_D = 0.8$ [m]	HV $P_D = 0.8$ [m]	HH $P_D = 0.9$ [m]	HV $P_D = 0.9$ [m]
RADARSAT-1	S1	149.5	N/A	183.1	N/A
	S4	54.4	N/A	66.7	N/A
	S7	30.1	N/A	36.8	N/A
RADARSAT-1	F1	24.1	N/A	29.5	N/A
	F3	18.5	N/A	22.7	N/A
	F5	15.5	N/A	18.9	N/A
RADARSAT-1	SCNB-near edge	197.0	N/A	241.3	N/A
	SCNB-far edge	71.7	N/A	87.8	N/A
Envisat ASAR	IS1	309.1	132.0	378.6	161.6
	IS4	73.1	63.8	89.5	78.1
	IS7	39.0	47.1	47.8	57.7
Sentinel-1	S1	38.0	18.6	46.5	22.8
	S3	19.3	13.6	23.6	16.7
	S6	10.0	11.2	12.3	13.8
Sentinel-1	IW1	34.7	28.0	42.5	34.2
	IW2	25.6	24.7	31.4	30.3
	IW3	20.6	22.7	25.3	27.8
Sentinel-1	EW1	180.9	95.9	221.6	117.4
	EW3	80.7	64.7	98.9	79.3
	EW5	55.8	61.2	68.3	74.9

Figure 15c) and Table 10 provide the model sensitivity to the margin parameter, showing how the minimum detectable ship length scales with the chosen margin value. The margin value could be significant, depending upon how the factors discussed in Section 3.2.5 accumulate. It could be appropriate to increase the margin, especially if the interest is in the detection performance for smaller ships.

Figure 15d) and Table 11 provide the model sensitivity to the K-distribution order parameter, showing how the minimum detectable ship length decreases for increasing order parameter (i.e., for more uniform or Gaussian clutter), and how the sensitivity increases for smaller order parameters.

Table 12 provides the model sensitivity to the local incidence angle, showing how the minimum detectable ship length decreases for increasing incidence angle. This arises since the background ocean clutter level decreases with increasing incidence angle. This particular case is clutter limited.

Table 13 provides the model sensitivity to several different model and system parameters. Considering the cases of co-polarization, the minimum detectable ship length is smaller for HH polarization than for VV polarization since the HH ocean clutter is smaller than the VV ocean clutter. For cross-polarization, there is only a marginal benefit in this case since the incidence angle is rather large. The benefit of cross-polarization would be more pronounced at smaller incidence angles. Considering the cases of the Sentinel-1 low versus high orbit, we see a marginal benefit for the low orbit case, arising mainly from the slightly larger incidence angle. Considering the cases of probability of detection, the choice of 0.8 permits the detection of smaller ships, but at the expense of more missed detections.

Figure 15e) and Table 14 provide the model sensitivity to the probability of false alarm. Smaller ships may be detected as the false alarm rate is relaxed, but at the expense of more false detections.

Table 15 provides the model sensitivity to some of the basic sensor parameters. The model is more sensitive to the range resolution than the azimuth resolution due to their relative scales (azimuth resolution is much larger than range resolution). The model is quite sensitive to ENL, but it is only realistic to consider this sensitivity if ENL is traded-off against one of the resolution values. In this case, the model is not sensitive to NESZ since this is a clutter-limited scenario.

Table 16 considers the impact of a trade-off between ENL and the slant-range resolution. Comparing the two single look cases, the slant-range resolution is doubled in the second case, representing the ship detection capability of two individual looks, or perhaps two views of the scene as could arise from successive TOPSAR [3] scans, the scanning methodology that will be employed for Sentinel-1. The idea here is to trade-off spatial resolution for two separate, temporally offset views of the scene that could be used to estimate the ship velocity. In this case, the minimum detectable ship length in each look degrades from 31.4 m to 44.4 m. This could be a useful trade-off if the ship velocity could then be estimated. The high spatial resolution of Sentinel-1 makes this trade-off feasible. The subsequent cases in the table show the sequential trade-off as the number of looks increases and the spatial resolution decreases (i.e., the information content is conserved). A degradation of minimum detectable ship length is apparent with increasing ENL.

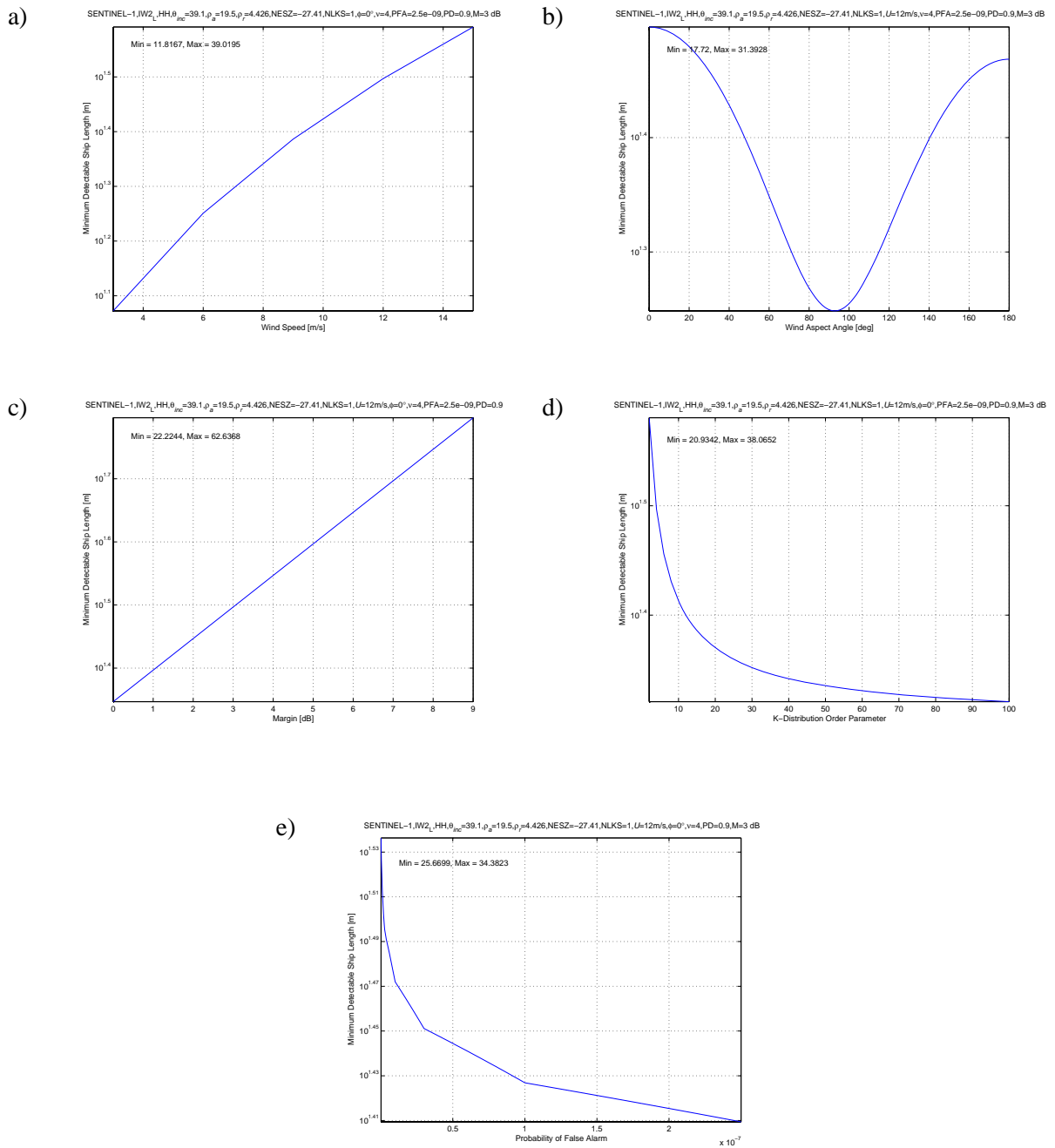


Figure 15: Minimum detectable ship length as a function of: a) wind speed; b) wind direction; c) model margin; d) order parameter; and e) probability of false alarm.

Table 8: Ship detectability – sensitivity to wind speed (U).

U [m/s]	L [m]	dL/dU [s]
3	11.8	1.92
6	17.8	2.09
9	24.3	2.26
12	31.4	2.44
15	39.0	2.65

Table 9: Ship detectability – sensitivity to wind direction (ϕ).

ϕ [deg]	L [m]	$dL/d\phi$ [m/deg]
0	31.4	-0.003
45	25.8	-0.197
90	17.8	-0.024
135	24.0	0.163
180	29.4	-0.003

Table 10: Ship detectability – sensitivity to model margin (M).

M [dB]	L [m]	dL/dM [m/dB]
0	24.3	2.82
3	31.4	3.98
6	48.6	5.63
9	68.6	7.94

Table 11: Ship detectability – sensitivity to order parameter (v).

v	L [m]	dL/dv [m]
2	38.1	-4.72
4	31.4	-1.77
10	25.9	-0.43
100	20.9	-0.03

Table 12: Ship detectability – sensitivity to incidence angle (θ).

θ [deg]	L [m]	$dL/d\theta$ [m/deg]
$\theta_{Mid} - 2$	35.8	-2.50
$\theta_{Mid} - 1$	33.5	-2.18
θ_{Mid}	31.4	-1.94
$\theta_{Mid} + 1$	29.6	-1.70
$\theta_{Mid} + 2$	28.0	-1.38

Table 13: Ship detectability – sensitivity to polarization state (P), orbit altitude, and probability of detection (P_D).

P	Orbit	P_D	L [m]
HH	low	0.8	25.6
		0.9	31.4
	high	0.8	28.6
		0.9	35.0
HV	low	0.8	24.7
		0.9	30.3
	high	0.8	25.7
		0.9	31.5
VH	low	0.8	24.7
		0.9	30.3
	high	0.8	25.7
		0.9	31.5
VV	low	0.8	35.7
		0.9	43.7
	high	0.8	39.0
		0.9	47.7

Table 14: Ship detectability – sensitivity to probability of false alarm (P_{FA}).

P_{FA}	L [m]
$2.5(10)^{-7}$	25.7
$2.5(10)^{-8}$	28.6
$2.5(10)^{-9}$	31.4
$2.5(10)^{-10}$	34.4

Table 15: Ship detectability – sensitivity to sensor parameters (ξ).

ξ	L [m]	$dL/d\xi$
ρ_{AZ} [m]	31.4	0.80 [-]
ρ_{SR} [m]	31.4	3.37 [-]
ENL	31.4	-10.91 [m/look]
NESZ [dB]	31.4	0.07 [m/dB]

Table 16: Ship detectability – trading ρ_{GR} for ENL.

ENL [m]	ρ_{GR} [m]	L [m]
1	4.4	31.4
1	8.8	44.4
2	8.8	34.8
3	13.2	37.4
4	17.6	39.7
5	22.0	41.9

3.5 Implications for Sentinel-1

The ship detection capability of the Sentinel-1 SAR was modelled by using a statistical detection model that includes system noise, ocean clutter, and ship RCS. Each model element includes a level and its variability, which is described by an appropriate PDF. For ship RCS, a database of Envisat ASAR AP mode ship signatures that were validated by shore-based AIS data was used to derive a relationship between ship RCS and ship length, and to model the ship RCS variability as a function of polarization. The model includes a margin to represent imaging issues that could not be fully modelled. The model output is the minimum detectable ship length for each of the radars of interest, specifically, Sentinel-1, RADARSAT-1, RADARSAT-2, and Envisat ASAR.

The relative performance between beam modes, all else held equal, is expected to be a solid prediction of the model. The absolute performance is subject to certain assumptions concerning the environmental conditions and the radar performance. However, the absolute performance is representative of the expected performance of a particular radar or mode.

Based upon the analysis carried out, the following conclusions with respect to Sentinel-1 capabilities are offered:

- The Sentinel-1 IW mode ship detection performance is significantly better than that of RADARSAT SCNB mode at HH polarization over a comparably wide swath. Note that SCNB is a fairly standard mode for ship detection using RADARSAT data. This improved performance is due to the much higher spatial resolution that will be offered by IW.
- The Sentinel-1 IW mode ship detection performance at cross-polarization is comparable to the ship detection performance at co-polarization, although the cross-polarization performance is largely independent of incidence angle. This is because IW starts at around 31° incidence angle. The benefit of cross-polarization is more important for smaller incidence angles, as seen for the performance of the EW mode.
- There is a penalty in terms of ship detection performance if the EW mode is used to gain additional swath coverage. However, the EW mode performance for the HV channel is comparable to that of RADARSAT SCNB, but with a broader swath.

4 Other maritime applications

4.1 Iceberg detection

4.1.1 Problem description

The iceberg detection problem is very similar to the ship detection problem, except that there is often an additional step taken to discriminate candidate ship signatures from candidate iceberg signatures, e.g., [10], [19]. The discrimination operation can be based upon the object's RCS, shape, and texture parameters, or on the relative response of the cross-polarization channel compared to the co-polarization channel.

Operational iceberg detection tends to use higher-numbered Envisat ASAR AP mode imagery. Acquisition in HH+HV mode facilitates ship/iceberg discrimination.

4.1.2 Implications for Sentinel-1

Sentinel-1, with its default selectable dual polarization and high spatial resolution, will support iceberg detection and ship/iceberg discrimination. The IW mode has a much broader swath than Envisat ASAR APP, which will benefit this application.

4.2 Wind retrieval

4.2.1 Problem description

The concept of kilometre-scale wind field retrieval from SAR ocean images was discussed in Section 3.2.2 in the context of the background ocean clutter. Wind retrieval from SAR is an application that has recently matured; SAR-derived wind fields are being demonstrated operationally and are being delivered to forecaster's desktops in near-real time, providing positive impact on weather forecasts [14].

Aside from knowledge of the wind direction and the SAR geometry, a suitable polarization-dependent geophysical model function relating ocean backscatter to wind speed is required. To date, for C-band instruments, these tend to focus on VV polarization due to model function heritage to the ERS scatterometers. Conversion of C-band VV model results to other polarizations tends to be done on an ad hoc basis. Nevertheless, errors of only a few m/s have been observed for RADARSAT-1 wind retrieval for moderate wind speeds [31]. Cross-polarization is a bigger problem since there is few validated observations and the CNR tends to be poor; ad hoc HV or VH models are immature.

In addition to an adequate CNR, a related issue is the instrument sensitivity to wind speed. This may be assessed from the slope of the geophysical model function. Considering co-polarization only, the geophysical model function sensitivity has been plotted in Figure 16 for the case of the wind blowing towards the radar ($\varphi = 0^\circ$). Recall that the co-polarization ratio is independent of

wind speed and direction. Note that sensitivity decreases for smaller incidence angles and for higher wind speeds. For the latter, we note the local maximum in this particular model function for higher wind speeds.

Operational wind field retrieval tends to use broader swath ScanSAR modes such as RADARSAT-1 SCW and Envisat ASAR WSM, to achieve wide area coverage. Better performance is expected for smaller incidence angles. HH or VV polarizations have been used successfully, although VV polarization offers higher CNR and a more mature geophysical model function. An impediment to operational utilization is infrequent repeat coverage (compared to the time scale of the meteorological processes of interest) and locally fixed pass times (i.e., always at nearly the same local time).

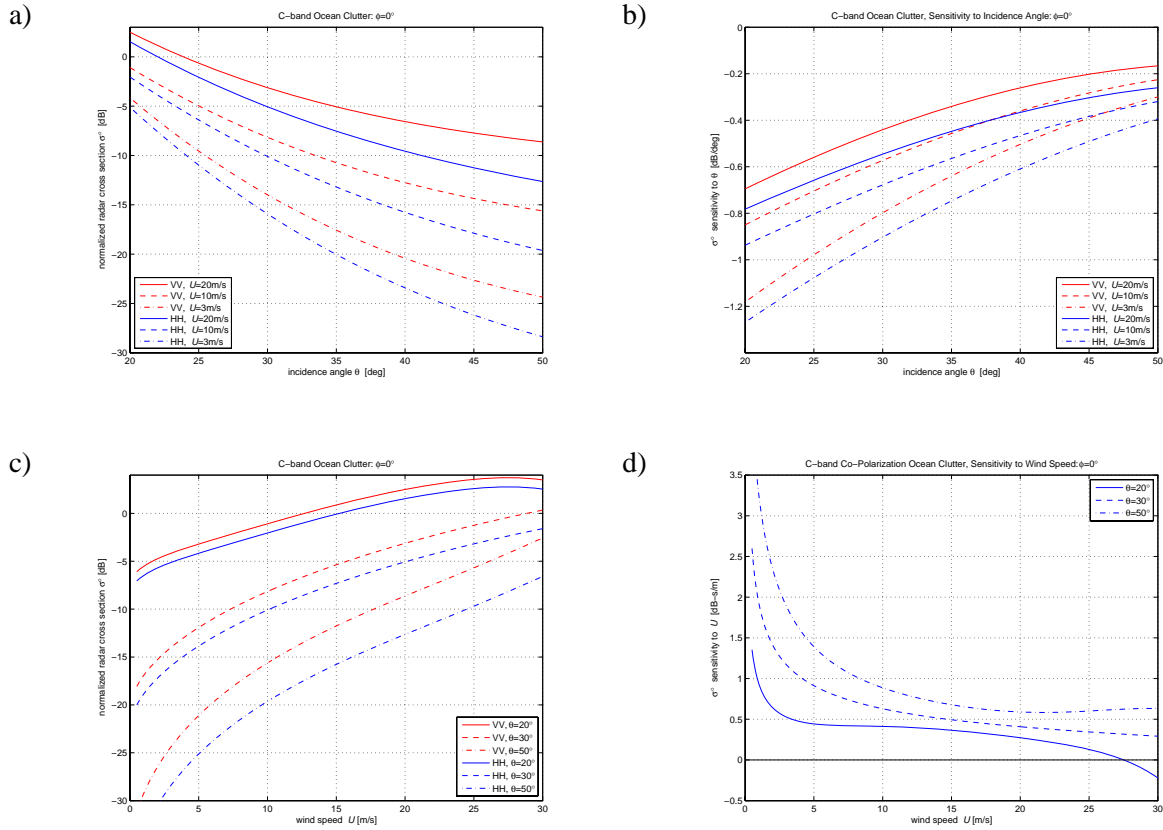


Figure 16: Wind retrieval sensitivity: a) clutter as a function of incidence angle; b) clutter sensitivity to incidence angle; c) clutter as a function of wind speed; d) clutter sensitivity to wind speed.

4.2.2 Implications for Sentinel-1

Sentinel-1 IW mode data appear to be well-suited to wind retrieval by using the co-polarization channel. There is enhanced sensitivity to wind speed for smaller incidence angles, not to mention the possibility of a higher clutter level, thus better clutter-to-noise ratio; an IW mode that starts at a smaller incidence angle would be beneficial. If a broader swath is needed, then the EW would be a good choice. However, the co-polarization channel of IW should be well suited to wind retrieval in the littoral zone. A constellation of two Sentinel-1 satellites would improve the repeat coverage, especially if taken in the context of other operational sources of SAR data.

4.3 Oil spill detection

4.3.1 Problem description

It is well known that ocean backscattering is a Bragg scattering process from ocean surface roughness at the scale of the radar wavelength, and that a layer of oil suppresses the Bragg-scale roughness. This in turn reduces the local ocean backscatter, so that oil can be seen in a SAR image as an area of darker return. In Figure 17, examples are presented of backscatter suppression from two RADARSAT-1 SCNA mode images that were acquired through an operational oil spill detection program in Canada [4]. The lower portion of each plot shows the normalized radar backscatter across the entire swath. The upper portion shows more detail in the vicinity of the oil slick of interest.

For the 30 Sept. 2004 image, there is a backscatter suppression of roughly 5 dB relative to a background clutter level of -18 dB. The background clutter level corresponds to a retrieved wind speed of between 4 m/s and 8 m/s, depending upon the wind direction, with the lower limit corresponding to an upwind look direction and the upper limit to a crosswind look direction. For the 23 Nov. 2004 image, there is a backscatter suppression of roughly 6 dB relative to a background clutter level of -17 dB. The background clutter level corresponds to a retrieved wind speed of between 5 m/s and 10 m/s, depending upon the wind direction.

In both cases, the backscatter has been suppressed to roughly -23 dB, a few decibels above the instrument noise floor. In these cases for which the wind speeds were rather light, the oil slicks were easy to detect by visual inspection of the image due to their dark signatures and size. Detection relies both on the reduction of the clutter and the sharpness of the transition between oil and the clean water around the edge of the spill. The images suggest that a CNR of at least 6 dB would permit the reliable detection of oil slicks. On the other hand, if the wind speed is too high, the slick would be dispersed and mixed downward into the water column. A useful rule of thumb is that the wind speed should be no higher than 10 m/s for successful oil spill detection.

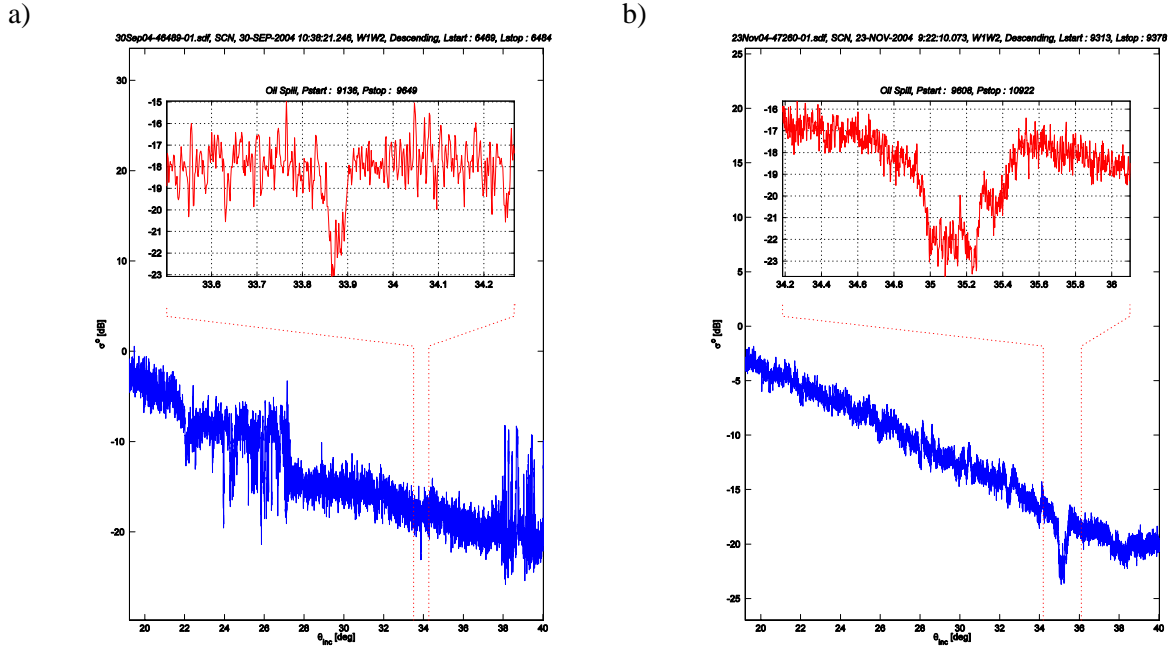


Figure 17: RADARSAT-1 SCNA C-band HH polarization ocean backscatter including an oil slick off the east coast of Canada: a) 30 Sept. 2004; b) 23 Nov. 2004.

Model results for suppression of C-band radar cross section by a layer of oil on the ocean surface can help to better justify the 6 dB CNR requirement. Charbonneau [2] has recently published calculations of ocean backscatter suppression that are based upon modifications to an ocean backscatter model. The calculations combine an ocean surface wave density spectrum model, which is used as the “clean” ocean reference, with the physical properties of an oil layer, which significantly reduces the surface wave density spectrum. The amount of backscatter suppression is a function of the oil’s physical properties (viscosity, elasticity, and surface tension) and of the oil layer thickness. Using an oil-damping model in the clean surface spectrum simulates the reduction in the wave density spectrum. The oil’s dielectric properties are included as a classical multi-layer system, but have little effect on the backscatter interaction due to the low relative permittivity and the thickness of the oil layer relative to the C-band wavelength.

Charbonneau has kindly provided us with several cases that are relevant to this problem. These are presented in what follows as plots of the backscatter suppression as a function of incidence angle for several wind speeds. These backscatter suppressions should be interpreted relative to the background ocean clutter levels for a clean ocean surface, as are available from the appropriate CMOD or hybrid backscatter models.

Figure 18 shows ocean backscatter suppression for a very thin ($< 10^{-7}$ m) layer of Oleyl Alcohol, which has similar properties to those of a natural surfactant. The RCS enhancement (i.e., positive degree of RCS suppression) at 25° incidence angle is an artefact of modifications to the integral equation model that are meant to compensate for a lack of signal near nadir. The prediction of

RCS enhancement represents a failure of this model for this particular case; however, the results and trends are thought to be correct for incidence angles that are larger than 35° . The increasing RCS suppression with increasing incidence angle, and decreasing backscatter suppression with increasing wind speed are the key predictions of the model. Backscatter suppressions of up to 7 dB are noted for HH polarization.

Figure 19 shows ocean backscatter suppression for a 20% emulsion of IFO-180, a high viscosity fuel oil. The backscatter enhancement artefact at smaller incidence angles is no longer present, although there is a trend to decreasing backscatter suppression with smaller incidence angles. There is increasing backscatter suppression for increasing incidence angles, with backscatter suppressions of more than 20 dB for lower wind speeds, and around 10 dB for higher wind speeds. The backscatter suppressions are similar for both polarizations.

Figure 20 shows ocean backscatter suppression for a thin (3×10^{-4} m) layer of Iranian Heavy crude oil, which is medium viscosity oil. We note that the backscatter enhancement artefact has returned for VV polarization. Otherwise, we see increasing backscatter suppression for increasing incidence angles, with significantly more backscatter suppression for HH polarization than for VV polarization.

These model results affirm that the suggested minimum CNR of 6 dB is a reasonable requirement for oil spill detection. To establish the impact of this guideline, consider the useful swath as a function of NESZ. This is plotted for Sentinel-1 IW mode parameters with a nominal NESZ of -24 dB in Figure 21. The vertical line represents the upper limit wind speed of 10 m/s. It is apparent that there is more useful swath for this application for VV polarization and upwind look directions.

Operational oil spill detection tends to use RADARSAT-1 SCNA data since much of the swath is suitable for oil detection, and higher resolution is available than with RADARSAT-1 SCW or Envisat ASAR WSM. Use of VV polarization broadens the useful swath; it is expected that operational services will soon be based upon RADARSAT-2 SCNA with VV polarization (or more likely VV+VH dual polarization to facilitate ship detection in the cross-polarization channel).

4.3.2 Implications for Sentinel-1

Although they have comparable swath widths, Sentinel-1's IW mode provides a fairly limited useful swath for oil spill detection compared to RADARSAT-1 SCNA since it starts at an incidence angle of roughly 30° compared to SCNA's 20° . Best performance will occur for VV polarization. The useful swath for this application would be larger if IW started at a smaller incidence angle. Access to two Sentinel-1 satellites would improve repeat coverage. Availability of dual polarization permits both ship detection and oil spill detection.

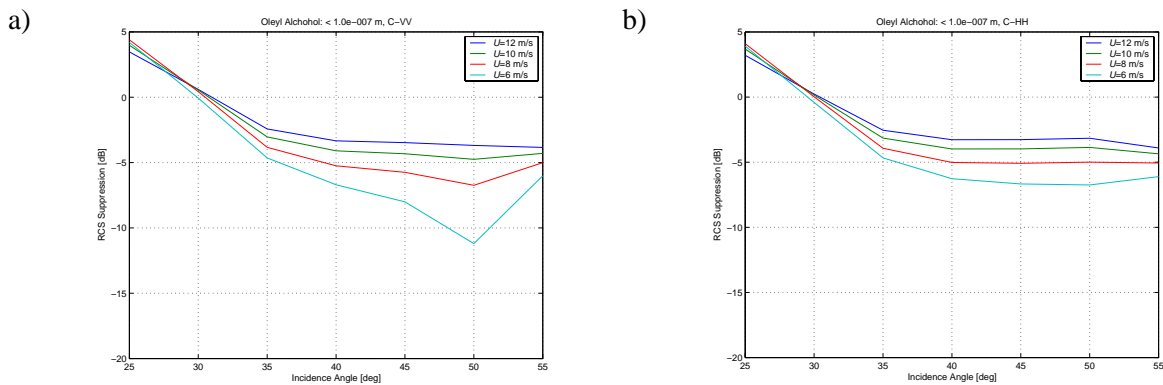


Figure 18: C-band ocean backscatter suppression by a thin layer of Oleyl Alcohol: a) VV; b) HH.

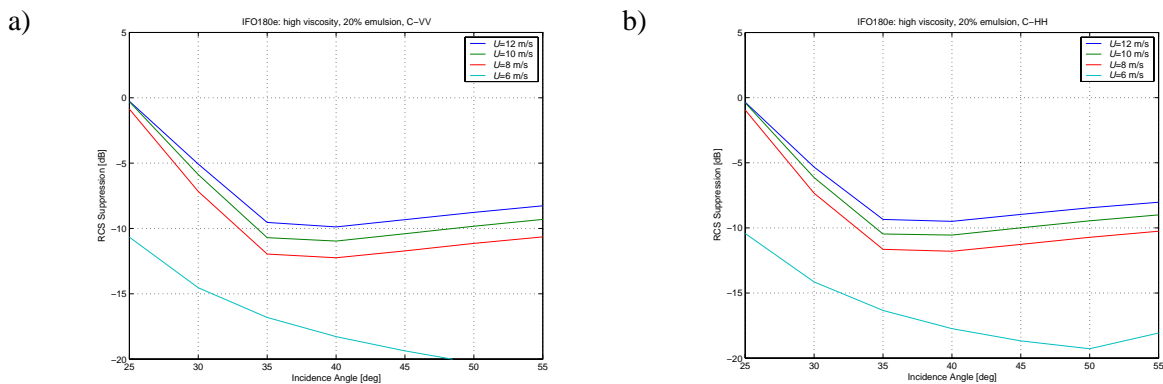


Figure 19: C-band ocean backscatter suppression by IFO180, 20% emulsion: a) VV; b) HH.

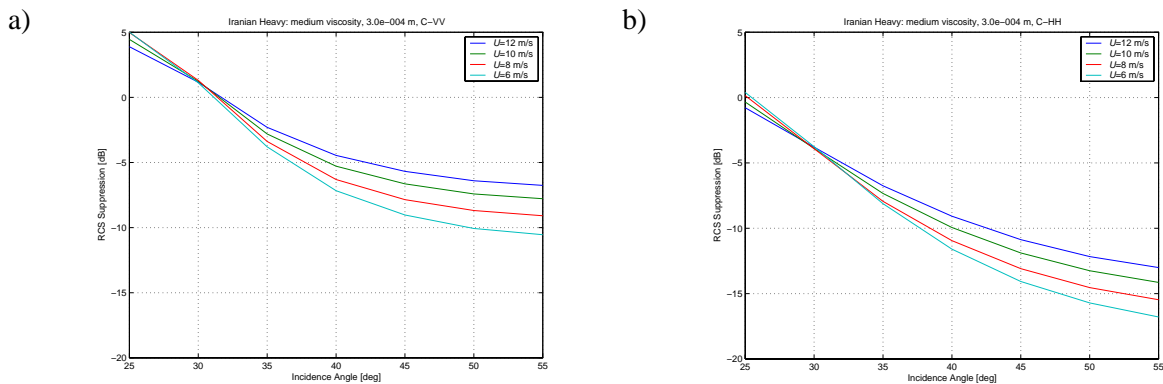


Figure 20: C-band ocean backscatter suppression by a thin layer of Iranian Heavy crude oil: a) VV; b) HH.

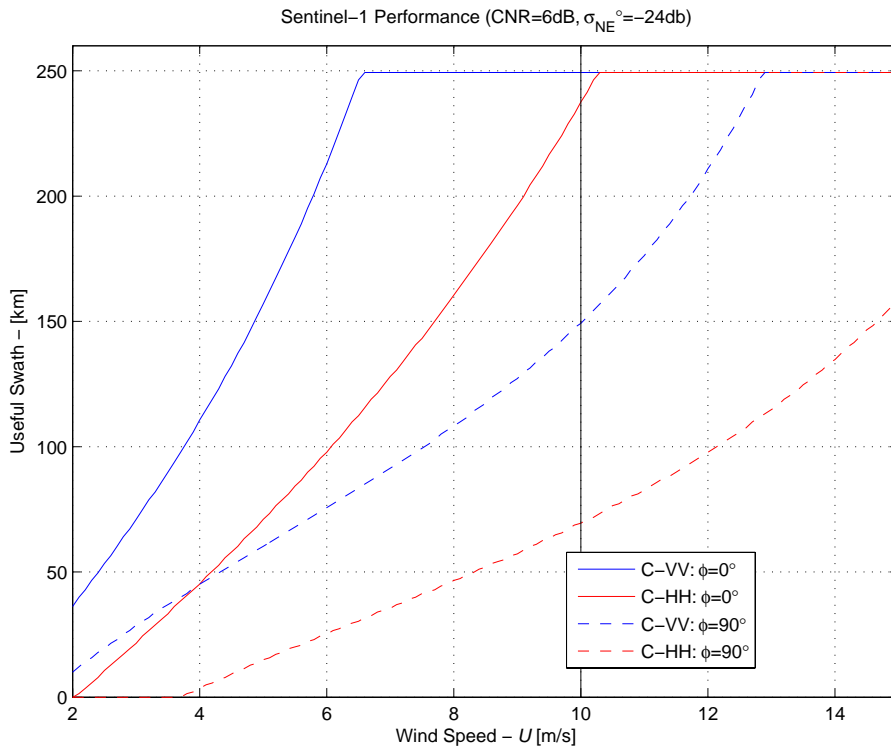


Figure 21: Swath having a CNR larger than 6 dB for a nominal noise floor of -24 dB.

4.4 Sea ice surveillance

4.4.1 Problem description

Use of SAR imagery for operational sea ice surveillance is a proven operational capability, e.g., [6]. The radar backscatter from sea ice depends upon many complex and inter-related factors including location, season, and ice type. Examples of backscatter profiles from RADARSAT-1 SCW imagery are shown in Figure 22, which were acquired near Anticosti Island and just north of Newfoundland during routine sea ice surveillance activities. These examples include the smooth new ice type, which has very low backscatter. It is apparent that, for this case, the backscatter drops down towards and below -26 dB, which is the nominal noise floor for RADARSAT-1.

The identification of smooth new ice is important for smaller vessels that have limited capability to operate within ice. Due to its lack of mechanical strength, smooth new ice deforms (and roughens) very quickly within the ice pack. As a result, within dynamic ice regimes, smooth new ice does not exist over large areas for extended periods of time. In less dynamic regions, such as in sheltered bays, lakes, and in the lee of coastal areas, smooth new ice has a greater presence. These sheltered areas may be high traffic areas for small vessels, thus it is an important requirement to be able to reliably identify and map the extent of smooth new ice.

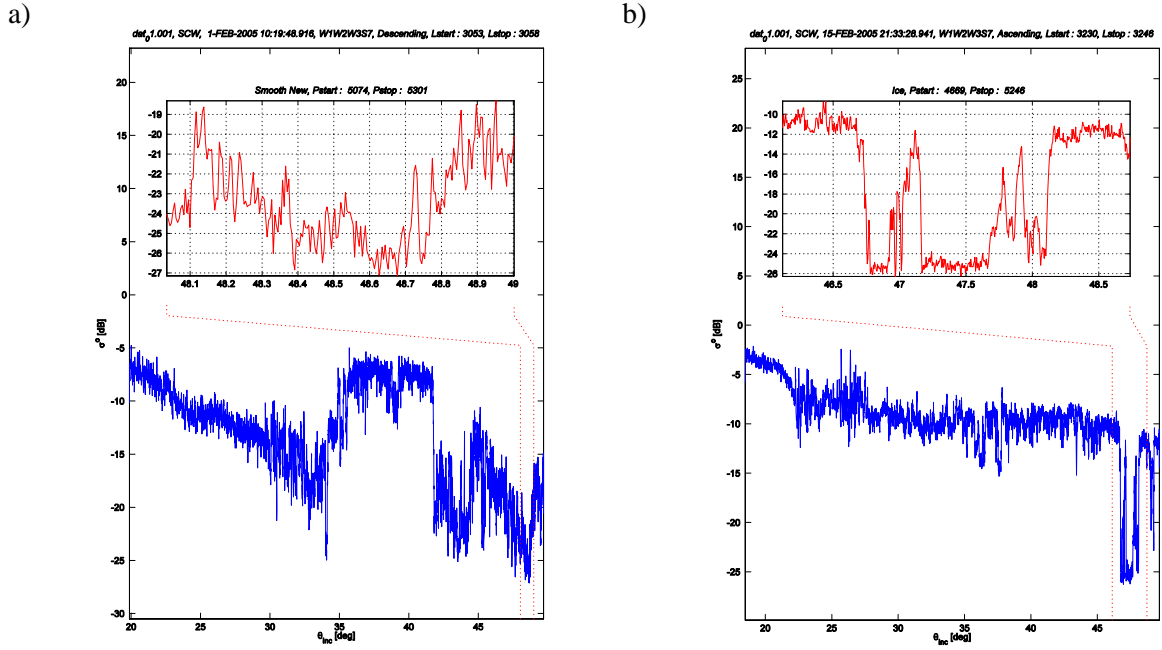


Figure 22: RADARSAT-1 SCW C-band HH polarization sea ice backscatter for smooth new ice: a) near Anticosti Island, 1 Feb. 2005; b) near Newfoundland, 15 Feb. 2005.

To further consider C-band backscatter from sea ice, consider the multi-polarization model of Nghiem and Bertoia [15], which has been validated for incidence angles up to 50° using JPL AirSAR data. The model was recently extended beyond 50° and to include the cross-polarization case [16]. Model results are shown in Figure 23; all linear polarizations are represented for first-year ice (FY), multi-year ice (MY), and smooth new ice (Leads). It is apparent that the normalized RCS difference between HH and VV polarization increases for increasing incidence angle, especially for the case of smooth new ice. There is good SNR for multi-year and first year ice. There are two potential problem cases: first, smooth new ice since the co-polarization backscatter signature drops down to and below -25 dB, as was noted in the RADARSAT-1 data; and second, cross-polarization backscatter, for which aside from the multi-year ice case, the backscatter is below -30 dB.

Ice edge detection is another sea ice surveillance requirement. This relies primarily on there being a difference between the sea ice backscatter and the ocean backscatter, which is generally most pronounced at larger incidence angles. Of course, ice versus ocean texture also enters into this, but a reversal in ice and ocean backscatter can occur, especially for smaller incidence angles (i.e., the ocean backscatter becomes larger than the ice backscatter for smaller incidence angles, whereas the ocean backscatter becomes smaller than the ice backscatter for larger incidence angles). Signature reversal could complicate ice edge detection. Using the Nghiem and Bertoia model, the lowest wind speed that would cause a signature reversal (i.e., for the upwind look direction) as a function of the incidence angle at which the signature reversal occurs for multi-

year ice and first year ice is plotted in Figure 24, which supports the notion of signature reversal being more likely for smaller incidence angles.

Operational sea ice surveillance tends to use RADARSAT-1 SCW due to its large swath. Dual polarization is expected to be beneficial in some cases, and could assist with ice edge detection for smaller incidence angles.

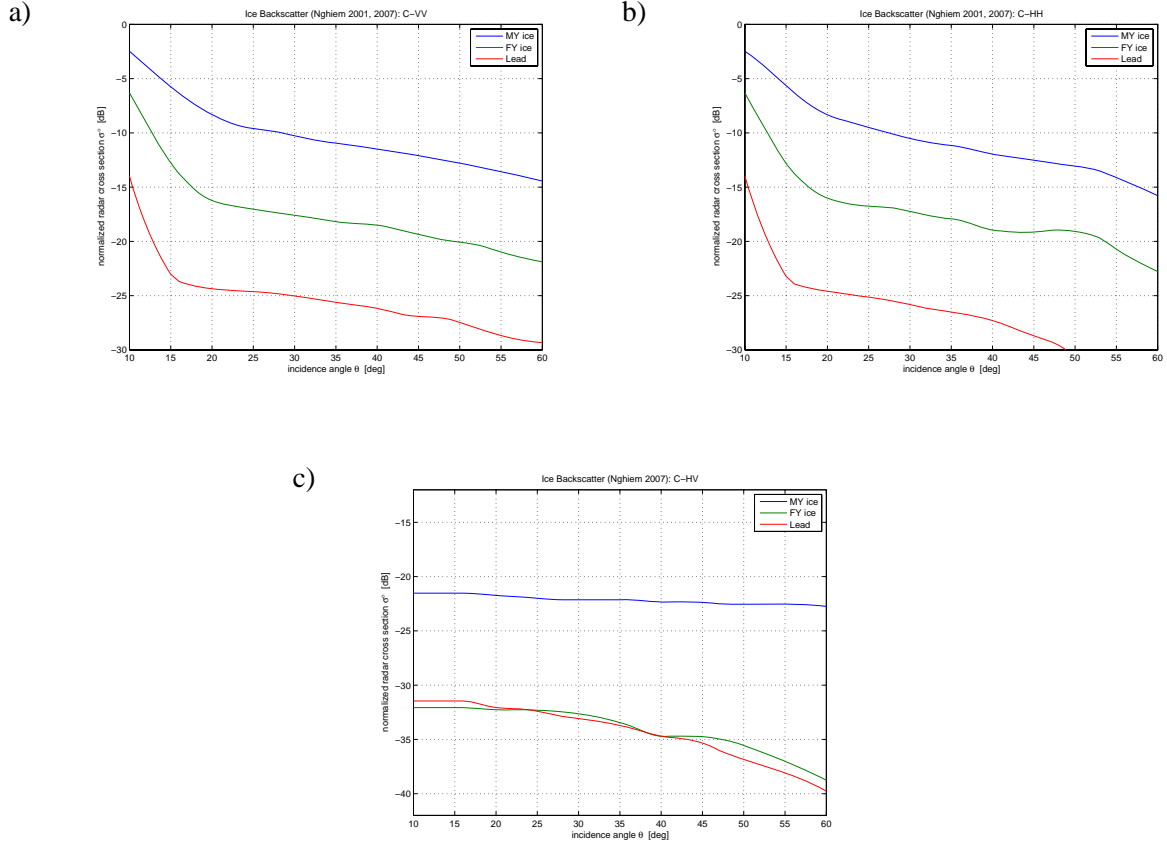


Figure 23: C-band sea ice backscatter: a) VV; b) HH; c) HV.

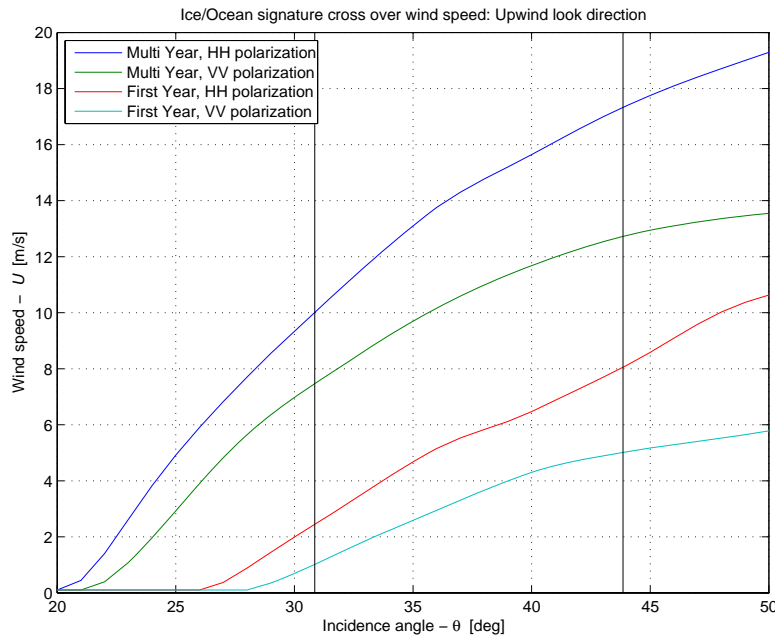


Figure 24: Lowest wind speed required to induce ice/ocean backscatter signature reversal.

4.4.2 Implications for Sentinel-1

In general, IW operating in dual polarization will be well-suited to sea ice surveillance. Since RADARSAT-1 SCW mode is often used for operational sea ice surveillance, the IW mode swath is too narrow compared to standard operational practice. However, access to a constellation of two Sentinel-1 satellites operating in this mode would alleviate this issue, as could use of EW mode.

The ability to detect and classify the smooth new ice (or lead) class is the most challenging requirement. Sentinel-1's noise floor is similar to that of RADARSAT-1 or Envisat ASAR. Also, the information content of the image (in terms of the higher spatial resolution) will be a benefit. Sentinel-1 will perform similarly to RADARSAT-1 or Envisat ASAR in terms of the noise floor, or perhaps better considering the higher resolution.

In Figure 26, the vertical lines indicate the extent of the IW swath for the low orbit case. For multi-year ice and C-band, HH polarization, ice/ocean backscatter signature reversal can occur for wind speeds in excess of 10 m/s. For first-year ice and C-band, HH polarization, ice/ocean backscatter signature reversal can occur for wind speeds in excess of 3 m/s. Signature reversal can occur for first year ice, but is less likely for multi-year ice. Sentinel-1 is less susceptible to signature reversal than RADARSAT-1 SCW due to the relatively large incidence angles that will be used.

4.5 Ship wake detection

4.5.1 Problem description

It is well known that ship wakes appear in SAR ocean images [18], arising in several forms including classic Kelvin and transverse wave wakes (Figure 25, e.g., [28]), and turbulent ship wakes (Figure 26a). A recent observation from Envisat ASAR AP mode data is that there can be a signature related to ship wakes in cross-polarization SAR data (Figure 26b), perhaps caused by the bow wave of the ship [9], [35]. For the cross-polarization case, the wake signature appears as an “echo” of the ship signature that is located near the apex of the wake that is visible in the co-polarization channel. Since the echo is not shifted in azimuth, it cannot be part of the ship itself and must be associated with the ship wake.

In general, ship wakes in co-polarization imagery are most visible under light to moderate wind conditions and when the clutter-to-noise ratio is high, suggesting greater success for smaller incidence angles. While ship wakes could form the basis of a ship detection algorithm, their occurrence is relatively rare. Usually ship wakes are searched for in the vicinity of candidate ship signatures as a mechanism to reduce false alarms and possibly to obtain an estimate of ship velocity based upon the azimuthal Doppler shift of the ship signature and the wake orientation.

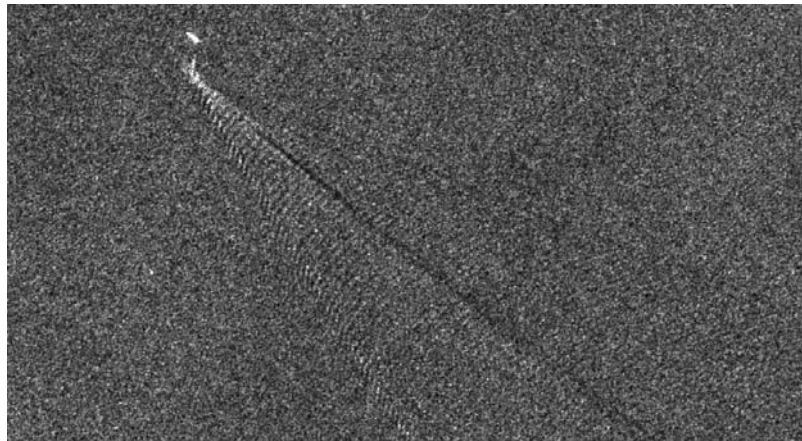


Figure 25: RADARSAT-1 image of a ship and its Kelvin wake (©Canadian Space Agency, 2001).

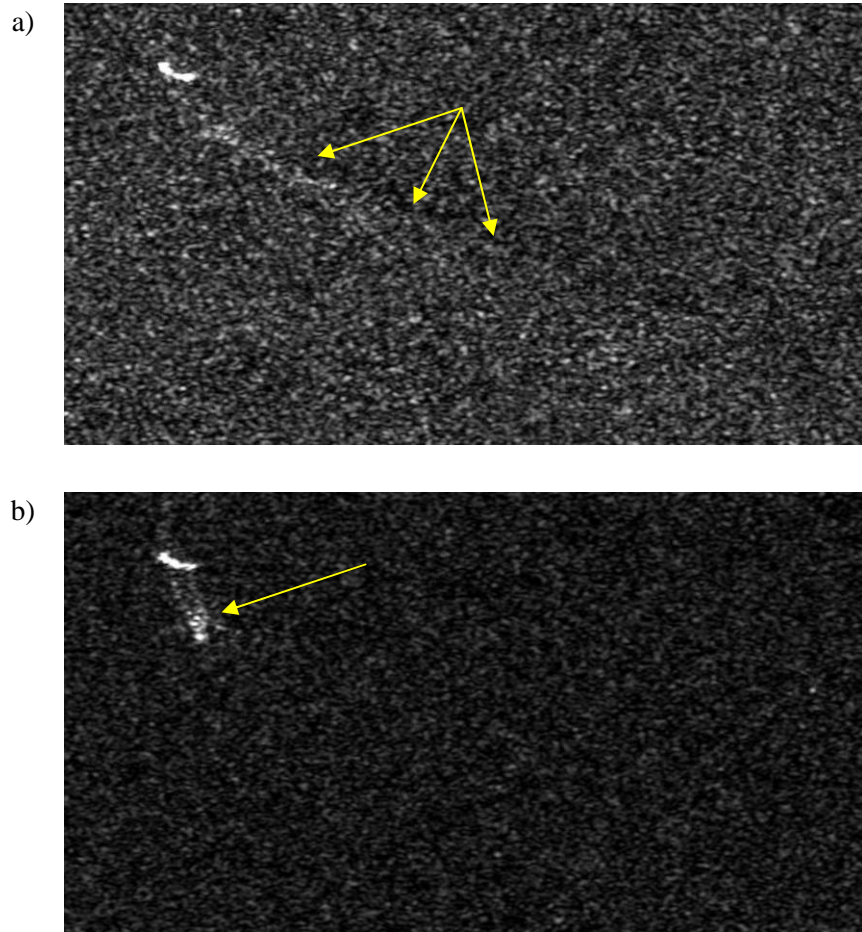


Figure 26: Envisat ASAR image of a ship and its wake (©European Space Agency, 2006): a) HH polarization turbulent wake; b) HV polarization wake signature. The arrows point to the wake features of interest.

There is much less observational evidence for ship wakes in cross-polarization imagery, but they do seem to be more prevalent for smaller incidence angles [9]. In principle, for a cross-polarization wake signature it should be possible to establish the radial component of the ship velocity from the azimuthal Doppler shift of the ship signature. An extended wake signature is not apparent in the cross-polarization case, so resolution of the full velocity vector from a cross-polarization wake signature alone would be difficult unless the ship orientation can be deduced from the ship signature.

Operational ship wake detection is rather rarely implemented due to opposing clutter requirements for ship wake detection and ship signature detection, with ship signature detection taking precedence since ship wakes are rather rarely observed. Dual polarization can help by focussing ship detection on the cross-polarization channel and ship wake detection on the co-polarization channel.

4.5.2 Implications for Sentinel-1

Sentinel-1 in IW mode with high spatial resolution and dual polarization will provide some ship wakes, especially if the VV channel is available. Ship signatures could be sought in both polarization channels, followed by wake detection in both channels in the vicinity of the wake signature. Wake detection in IW mode would be better if smaller incidence angles were available.

5 Conclusions

This document addresses the analysis of marine applications potential of the GMES Sentinel-1 SAR mission. The main focus of the work has been on ship detectability modelling, but other marine applications including iceberg detection, wind retrieval, oil spill detection, sea ice surveillance, and ship wake detection are also addressed.

The ship detectability model has extended previous modelling that was carried out for RADARSAT-1 to other sensors, and takes into consideration alternating polarization observations from Envisat ASAR trials. The detection model applies to all linear polarizations and has been implemented as a Matlab® ship detectability performance tool that operates in several modes. All model results and plots concerning ship detection that are presented in this document were generated with the tool.

Whereas Sentinel-1 will have several modes of operation, the focus of this work has been the Interferometric Wide (IW) mode. This is expected to be Sentinel-1's default mode of operation in the littoral zone. Performance of the IW mode has been compared relative to current operational practice with RADARSAT-1 and Envisat ASAR.

The ship detectability modelling has shown that IW is very well-suited to ship detection, almost regardless of the available polarization. HH polarization is the best of the co-polarization choices, with cross-polarization improving performance at smaller incidence angles. Availability of two polarizations would improve the detection performance or could be used to reject false alarms. Cross-polarization would have more benefits for incidence angles smaller than the minimum of 29° to 31° for IW. On the other hand, cross-polarization clutter could become a factor for incidence angles of less than 25° or so.

The other maritime surveillance applications were treated relatively cursorily compared to the treatment of ship detectability:

- For iceberg detection and ship/iceberg discrimination, IW with HH+HV polarization is expected to work well;
- For wind retrieval, IW performance would be better if the incidence angles were smaller;
- For oil spill detection, IW performance would be better if the incidence angles were smaller;
- For sea ice surveillance, IW performance is expected to be very good, but a larger swath would be desirable;
- For ship wake detection, dual polarization with high spatial resolution is expected to be a benefit, but IW performance would be better if the incidence angles were smaller.

As a general statement, the one-size-fits-all approach that will be adopted with Sentinel-1 IW operations will suit most maritime applications in the littoral zone rather well. On the other hand, use of smaller incidence angles would be beneficial for several applications.

5.1 Future work to consider

A few gaps and weaknesses are apparent in this study that could benefit from additional study. These are summarized as follows:

- Modelling and error bound estimates should be improved for moving ships;
- Cross-polarization clutter should be measured and models should be improved;
- Implement other C-band ocean back scatter models (such as CMOD5);
- Estimation of the K-distribution order parameter for ocean clutter should be addressed and models for the K-distribution order parameter as a function of sea state should be developed;
- Other detection approaches such as use of inter-look coherence should be considered, both experimentally and as an extension to the current ship detectability tool. This would include use of successive TOPSAR scans to provide two images separated in time for estimation of ship velocity;
- The RADARSAT-2 component of the ship detectability tool is incomplete, especially for the higher resolution RADARSAT-2 modes. Actual RADARSAT-2 noise floors should also be implemented in the ship detectability tool;
- Implement the tool for other sensors, such as TerraSAR-X. This would require a campaign to acquire appropriate data for generation of ocean clutter and ship RCS at X-band;
- RADARSAT-2 UltraFine mode data should be evaluated to further study the performance of higher resolution data, especially with respect to the detection of small ships (e.g., $L < 50$ m) as should be detectable by Sentinel-1 IW mode. UltraFine mode data could be degraded to simulate Sentinel-1 S and IW mode data;
- Modelling of dual-polarization data for ship and iceberg discrimination should be carried out and implemented as an extension of the ship detectability tool.

References

- [1] Attema, E., Davidson, M., Flouri, N., Levrini, G., Rosich, B., Rommen, B., and Snoeij, P. (2008). Sentinel-1 ESA's new European radar observatory. Proc. 7th European Conference on Synthetic Aperture Radar (EUSAR 2008), 2 to 5 June 2008, Friedrichshafen, Germany. Vol. 1, 179-182. VDE Verlag, Berlin, ISBN 978-3-8007-3084-1.
- [2] Charbonneau, F. (2005). Caractérisation du coefficient de rétrodiffusion radar des surfaces d'hydrocarbure: Modélisation et interprétation. Ph.D. Thesis, Département de géographie et télédétection, Université de Sherbrooke.
- [3] D'Aria, D., De Zan, F., Giudici, D., Monti Guarneri, A., and Rocca, F. (2007). Burst-mode SARs for wide-swath surveys. *Canadian Journal of Remote Sensing*, 33(1), 27-38.
- [4] De Abreu, R., Gauthier, M.-F., and Van Wychen, W. (2006). SAR-based oil pollution surveillance in Canada: Operational implementation and research priorities. Proc. OceanSAR 2006 – The Third Workshop on Coastal and Marine Applications of SAR, St. John's, NL, Canada, 23 to 25 October 2006.
- [5] European Space Agency (2008). ASAR Public Performance Reports. Available: http://earth.esa.int/pcs/envisat/asar/public_reports.
- [6] Flett, D. (2003). Operational use of SAR at the Canadian Ice Service: Present operations and a look to the future. Proc. 2nd Workshop on Coast and Marine Applications of SAR, pp. 183-197, Svalbard, Norway, 8 to 12 Sept. 2003.
- [7] Greidanus, H., and Kourtzi, N. (2006). Findings of the DECLIMS project - Detection and classification of marine traffic from space. Proc. SEASAR 2006: Advances in SAR oceanography from ENVISAT and ERS. 23 to 26 Jan. 2006, ESA-ESRIN, Frascati, Italy.
- [8] Greidanus, H. (2006). Sub-aperture behavior of SAR signatures of ships. Proc. 2006 International Geoscience and Remote Sensing Symposium (IGARSS 2006). CD-ROM proceedings. 31 July to 4 Aug. 2006, Denver, USA.
- [9] Greidanus, H., Thoorens, F.X., Bauna, T., Indregard, M., and Arnesen, T.N. (2007). Ship detection in Envisat ASAR alternating polarization images. Proc. 7th ASAR Workshop, on CD-ROM. 11 to 13 Sept. 2007, Vancouver, B.C., Canada.
- [10] Henschel, M.D., and Livingstone, C.E. (2006). Observation of vessel heave with airborne SAR. Proc. OceanSAR 2006 – The Third Workshop on Coastal and Marine Applications of SAR, St. John's, NL, Canada, 23 to 25 October 2006.
- [11] Howell, C., Mills, J., Power, D., Youden, J., Dodge, K., Randell, C., Churchill, S., and Flett, D. (2006). A multivariate approach to iceberg and ship classification in HH/HV ASAR data. Proc. 2006 International Geoscience and Remote Sensing Symposium (IGARSS 2006). CD-ROM proceedings. 31 July to 4 Aug. 2006, Denver, USA.

- [12] Jackson, C.R., and Apel, J.R., eds. (2004). Synthetic aperture radar marine user's manual. National Oceanic and Atmospheric Administration, US Dept. of Commerce, September 2004, ISBN 0-16-073214-X. Available: <http://www.sarusersmanual.com/>.
- [13] Johnsen, H. (2007). A novel method for spaceborne SAR vessel-detection using complex radar backscatter – Using ASAR WSS product. Norut report IT 08/2007.
- [14] Neil, A., Saper, R.H., Lange, O., and Vachon, P.W. (2006). Operational utilization of SAR-derived winds for forecast operations at the Pacific Storm Prediction Centre. Proc. OceanSAR 2006 – The Third Workshop on Coastal and Marine Applications of SAR, St. John's, NL, Canada, 23 to 25 October 2006.
- [15] Nghiem, S.V., and Bertoia, C. (2001). Study of multi-polarization C-band backscatter signatures for Arctic sea ice mapping with future satellite SAR. *Canadian Journal of Remote Sensing*, 27(5), 387-402.
- [16] Nghiem, S.V. (2007). L-band and C-band SAR scattering signature of sea ice for operational applications. JPL D-40304, National Aeronautics and Space Administration, Jet Propulsion Laboratory.
- [17] Ouchi, K., Tamaki, S., Yaguchi, H., and Iehara, M. (2004). Ship Detection based on coherence images derived from cross correlation of multilook SAR images. *IEEE Geoscience and Remote Sensing Letters*, 1(3), 184-187.
- [18] Pichel, W.G., Clemente-Colón, P., Wackerman, C.C., and Friedman, K.S. (2004). Ship and wake detection. Ch. 12 in: Jackson, C.R., and Apel, J.R., eds. (2004). Synthetic aperture radar marine user's manual. National Oceanic and Atmospheric Administration, US Dept. of Commerce, September 2004, ISBN 0-16-073214-X. Available: <http://www.sarusersmanual.com/>.
- [19] Pond, S., and Pickard, G.L. (1983). Introductory Dynamical Oceanography, 2nd Edition. Pergamon Press, Toronto.
- [20] Power, D., Youden, J., Lane, K., Randell, C., and Flett, D. (2001). Iceberg detection capabilities of RADARSAT synthetic aperture radar. *Canadian Journal of Remote Sensing*, 27(5), 476-486.
- [21] Raney, R.K. (1971). Synthetic aperture imaging radar and moving targets. *IEEE Transactions on Aerospace and Electronic Systems*, AES-7(3), 499-505.
- [22] Rosich, B., Torres, R., Navas, I., Monti-Guarnieri, A., and Meadows, P.J. (2006). ASAR calibration performance: a review after four years of operation. Proc. 6th European Conference on Synthetic Aperture Radar (EUSAR 2006), on CD-ROM. 16 to 18 May 2006, Dresden, Germany.

- [23] Rostan, F., S. Riegger, W. Pitz, R. Croci, and R. Torres (2008). The C-SAR instrument design & performance for the GMES Sentinel-1 Mission. Proc. 7th European Conference on Synthetic Aperture Radar (EUSAR 2008), on CD-ROM. 2 to 5 June 2008, Friedrichshafen, Germany. Vol. 2, 257-260. VDE Verlag, Berlin, ISBN 978-3-8007-3084-1.
- [24] Rostan, F., Riegger, S., Pitz, W., Croci, R., and Torres R. (2008). The Sentinel-1 C-SAR instrument: Status and performance. To appear, Proc. 2008 International Geoscience and Remote Sensing Symposium (IGARSS 2008). 7 to 11 July 2008, Boston, USA.
- [25] Sharma, J.J., Gierull, C.H., and Collins, M.J. (2006). Compensating the effects of target acceleration in dual-channel SAR-GMTI. *IEEE Proceedings on Radar, Sonar, and Navigation*, 153(1), 53-62.
- [26] Srivastava, S.K., Côté, S., Le Dantec, P., Hawkins, R.K., and Murnaghan, K. (2007). RADARSAT-1 calibration and image quality evolution to the extended mission. *Advances in Space Research*, 39(1), 7-12, doi:10.1016/j.asr.2006.02.027.
- [27] Tello, M., López-Martínez, C., and Mallorqui, J. (2005). A Novel Algorithm for Ship Detection in SAR Imagery Based on the Wavelet Transform. *IEEE Geoscience and Remote Sensing Letters*, 2(2), 201-205.
- [28] Tunaley, J.K.E. (2005). Status of ship wake modelling for radar imagery. Proc. 8th International Conference on Remote Sensing for Marine and Coastal Environments, on CD-ROM. 17 to 19 May 2005, Halifax, Nova Scotia, Canada.
- [29] Vachon, P.W., Raney, R.K., and Emery, W.J. (1989). A simulation for spaceborne SAR imagery of a distributed, moving scene. *IEEE Transactions on Geoscience and Remote Sensing*, 27(1), 67-78.
- [30] Vachon, P.W., Campbell, J.W.M., Bjerkelund, C., Dobson, F.W., and Rey, M.T. (1997). Ship detection by the RADARSAT SAR: Validation of detection model predictions. *Canadian Journal of Remote Sensing*, 23(1), 48-59.
- [31] Vachon, P.W., and Dobson, F.W. (2000). Wind retrieval from RADARSAT SAR images: Selection of a suitable C-band HH polarization wind retrieval model. *Canadian Journal of Remote Sensing*, 26(4), 306-313.
- [32] Vachon, P.W., English, R.A., and Wolfe, J. (2007). Validation of RADARSAT-1 Vessel Signatures with AISLive data. *Canadian Journal of Remote Sensing*, 33(1), 20-26.
- [33] Vachon, P.W., Wolfe, J., and Hawkins, R.K. (2004). Comparison of C-band wind retrieval model functions with airborne multipolarization SAR data. *Canadian Journal of Remote Sensing*, 30(3), 462-469.
- [34] Vachon, P.W., English, R.A., and Wolfe, J. (2007). Ship signatures in synthetic aperture radar imagery: Validation using Automatic Identification System data. Proc. 2007 International Geoscience and Remote Sensing Symposium (IGARSS 2007), 23 to 27 July 2007, Barcelona, Spain.

- [35] Vachon, P.W., English, R.A., and Wolfe, J. (2007). Ship signatures in Envisat ASAR AP Mode data. Proc. 7th ASAR Workshop, on CD-ROM. 11 to 13 Sept. 2007, Vancouver, B.C., Canada.
- [36] Vachon, P.W., and Wolfe, J. (2008). Validation of ship signatures in Envisat ASAR AP mode data using AISLive: Data acquisition, processing, and analysis results. DRDC Ottawa TM 2008-005, Defence R&D Canada – Ottawa.

Annex A SAR Ship Detectability Performance Tool

The *SAR Ship Detectability Performance Tool* is a GUI-driven system written in the Matlab® scripting language and should run on any computer that has basic Matlab® installed. The essence of the tool is to provide the *minimum detectable ship length* given configurable sensor, performance, and environmental parameters. The minimum detectable ship length calculation is described in Section 3.2 of this document. The tool currently supports five sensors: Sentinel-1 with Low and High orbit scenarios, RADARSAT-1, RADARSAT-2, and Envisat ASAR. Supported beam modes for each of the sensors are shown in Table 17. Other beam modes can be added and/or modified with relative ease. Available polarizations are HH, VV, HV, and VH. For RADARSAT-1, only HH-polarization is available, regardless of the chosen polarization.

The GUI provides the ability to modify parameters via a series of pop-up menus, radio buttons, and text windows. Text windows with a white background can be modified by the user. Text windows with a grey background are not directly editable by the user, but in some cases are slaved to another parameter that can be modified. Tool parameters are summarized in Table 18.

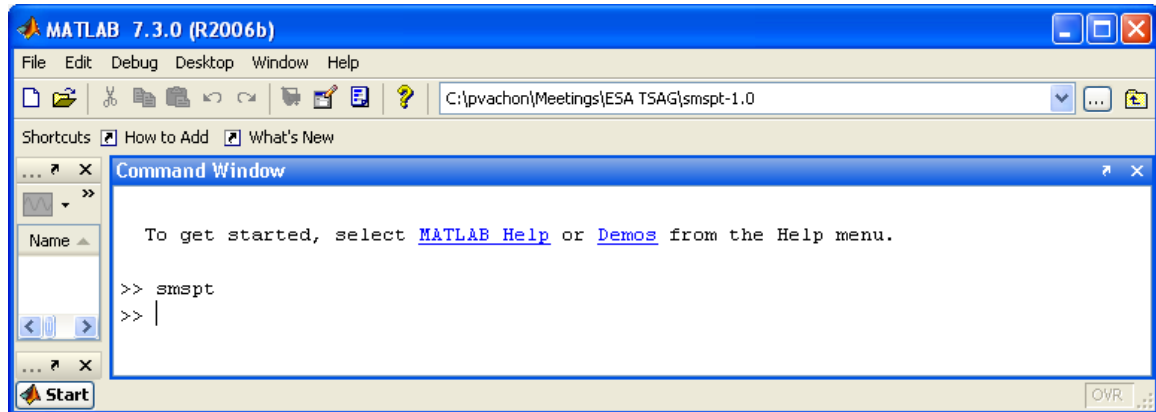
Table 17: Supported beam modes for each Sensor.

Sentinel-1/2	RADARSAT-1/2	Envisat ASAR
S1	S1	APP-IS1
S2	S2	APP-IS2
S3	S3	APP-IS3
S4	S4	APP-IS4
S5	S5	APP-IS5
S6	S6	APP-IS6
IW1	S7	APP-IS7
IW2	F1	WSM-SS1
IW3	F2	WSM-SS2
EW1	F3	WSM-SS3
EW2	F4	WSM-SS4
EW3	F5	WSM-SS5
EW4	W1	IMP-IS1
EW5	W2	IMP-IS2
	W3	IMP-IS3
	EH1	IMP-IS4
	EH2	IMP-IS5
	EH3	IMP-IS6
	EH4	IMP-IS7
	EH5	
	EH6	
	EL1	
	SCNA	
	SCNB	
	SCWA	
	SCWB	

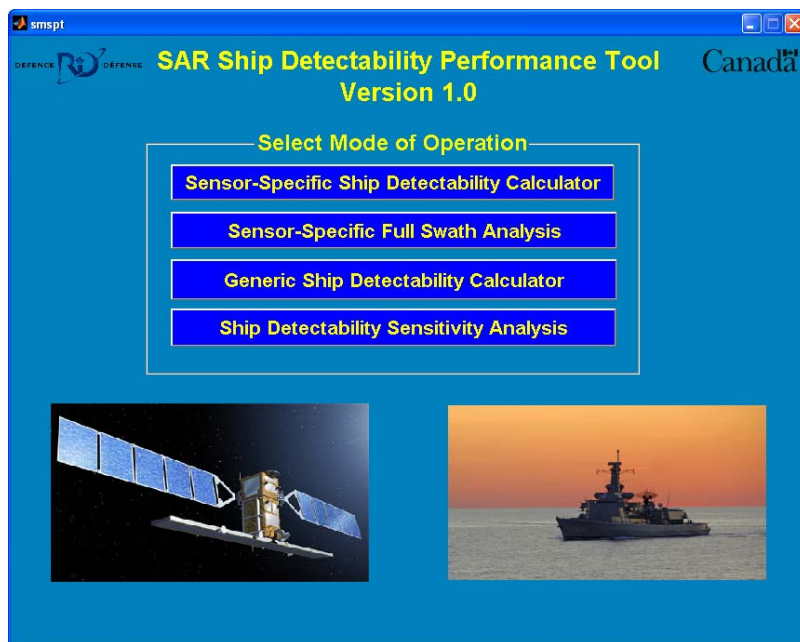
Table 18: Glossary of parameters presented when using the SAR ship detectability performance tool.

Parameter	Description	Status	Nature	Units
Clutter to Noise Ratio (CNR)	The ratio of the model ocean radar cross-section and NESZ.	Output		dB
Incidence Angle (θ)	The angle between the radar beam and the local normal.	Input	Sensor	deg
K-Distribution order parameter (v)	The multi-look intensity K-distribution parameter that describes the local modulation of the mean.	Input	Environment	—
Margin (M)	A contingency factor that is added to the minimum detectable radar cross section.	Input	Detection Performance	dB
Minimum Detectable RCS (σ)	The minimum detectable radar cross section.	Output		dB- m^2
Minimum Detectable Ship Length (L)	The minimum detectable ship length.	Output		m
Minimum Detectable Peak to Clutter Ratio (PCR)	The minimum detectable peak to clutter ratio assuming the target is restricted to a single resolution cell.	Output		dB
NESZ (σ_{NE}^0)	The radar system noise equivalent sigma zero.	Input or from Tables	Sensor	dB
NLOOKS (ENL or N)	The equivalent number of independent looks.	Input or from Tables	Sensor	—
Ocean Clutter (σ^0)	The normalized radar cross section of the background ocean clutter.	Output		dB
PD %80 or PD %90 (20p or 10p) (P_D)	The two available probabilities of detection.	Input	Detection Performance	%
Probability of False Alarm (P_{FA})	The false alarm rate.	Input	Detection Performance	—
RHOa (ρ_A)	The azimuth resolution.	Input or from Tables	Sensor	m
RHOr (ρ_{GR})	The ground range resolution.	Input or calculated	Sensor	m
Wind Speed (U)	The measured wind speed, usually parameterized as the equivalent neutral stability wind measured at a height of 10 m above the ocean surface.	Input	Environmental	m/s
Wind Aspect Angle (ϕ)	The angle between the wind direction and the SAR look direction (zero for wind blowing towards the radar).	Input	Environmental	deg

To install the tool, save the contents of the provided zip archive to a uniquely named directory. To launch the tool, invoke Matlab®, change to the installation directory, and type *smspt* at the Matlab® prompt:



The following startup menu is displayed:

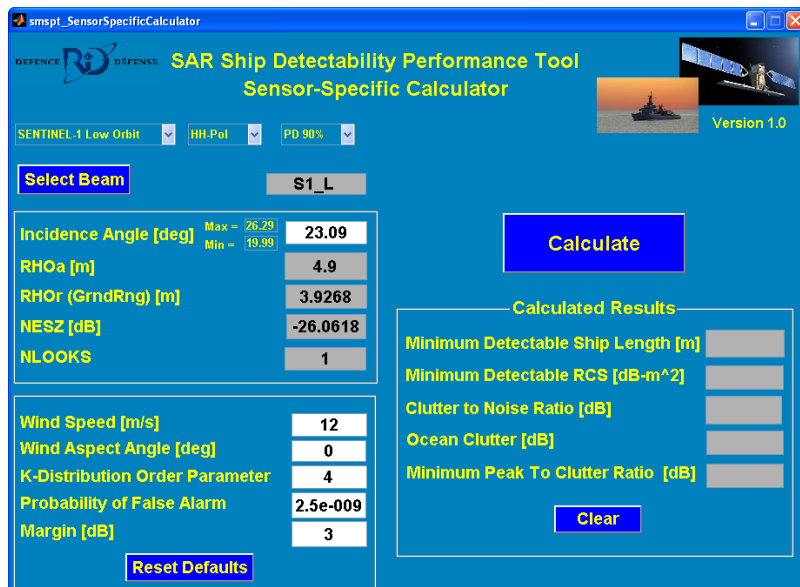


The user is presented with four options from which to choose:

1. Sensor-Specific Ship Detectability Calculator;
2. Sensor-Specific Full Swath Analysis;
3. Generic Ship Detectability Calculator; and
4. Ship Detectability Sensitivity Analysis.

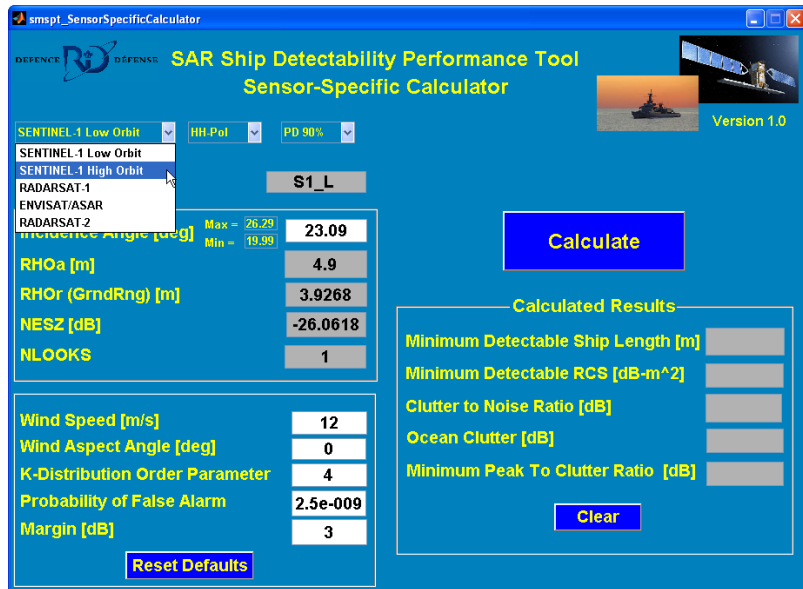
A.1 Sensor-Specific Ship Detectability Calculator

Based on user-selected parameters, the *Sensor-Specific Ship Detectability Calculator* calculates the *Minimum Detectable Ship Length* in meters, the *Minimum Detectable RCS* in dB-m², the *Clutter to Noise Ratio* in dB, the *Ocean Clutter* level in dB, and the *Minimum Peak to Clutter Ratio* in dB.

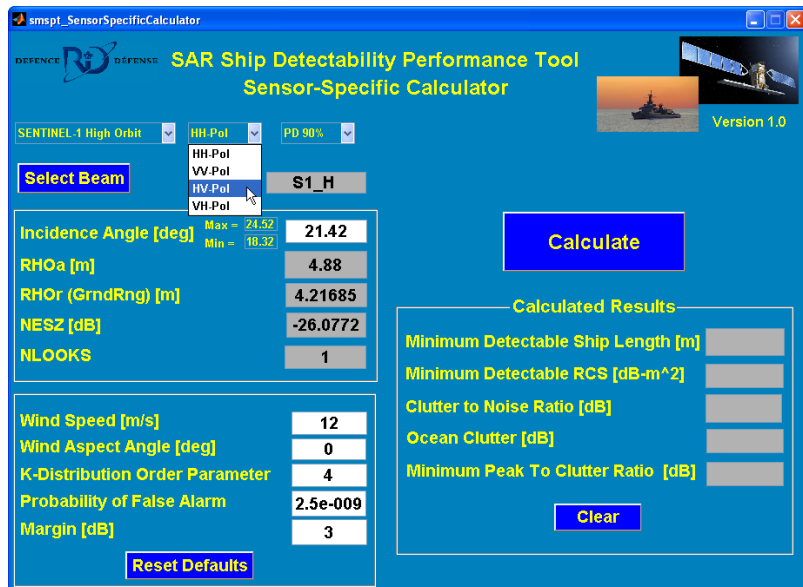


To calculate parameters for a Sentinel-1 High Orbit, HV-polarization, with probability of detection of 80% for the near-edge of beam IW2 at the default supplied values of wind speed of 12 m/s, wind aspect angle of 0°, K-distribution order parameter of 4, probability of false alarm of 2.5e-9, and margin of 3 dB, the user would do the following:

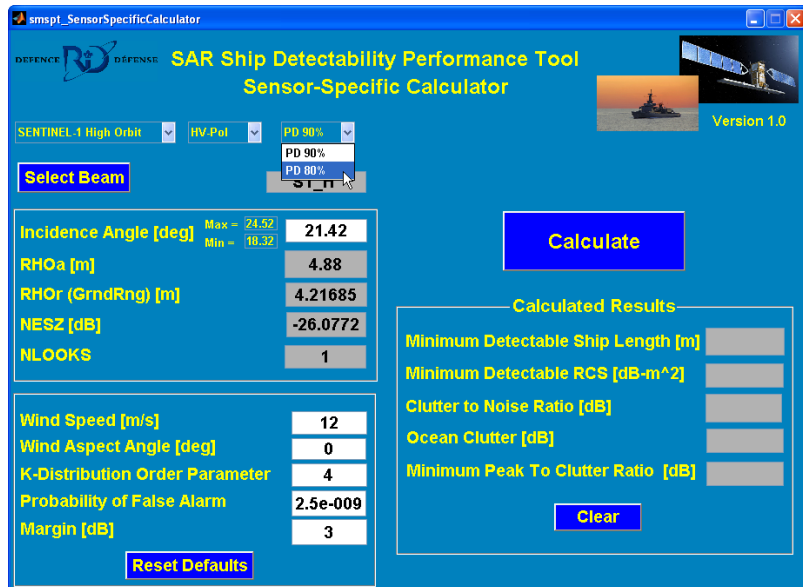
From the sensor popup menu select SENTINEL-1 High Orbit:



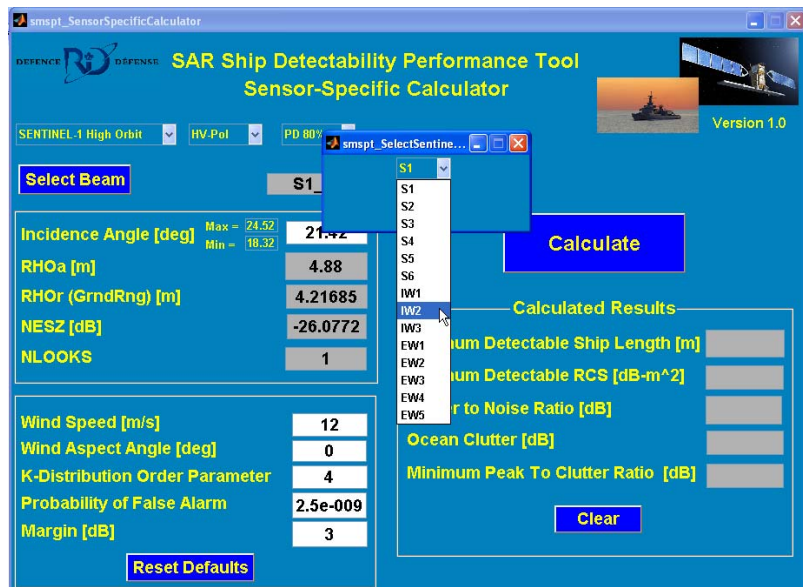
From the polarization popup menu select HV-Pol:



From the probability of detection popup menu select **PD 80%**:

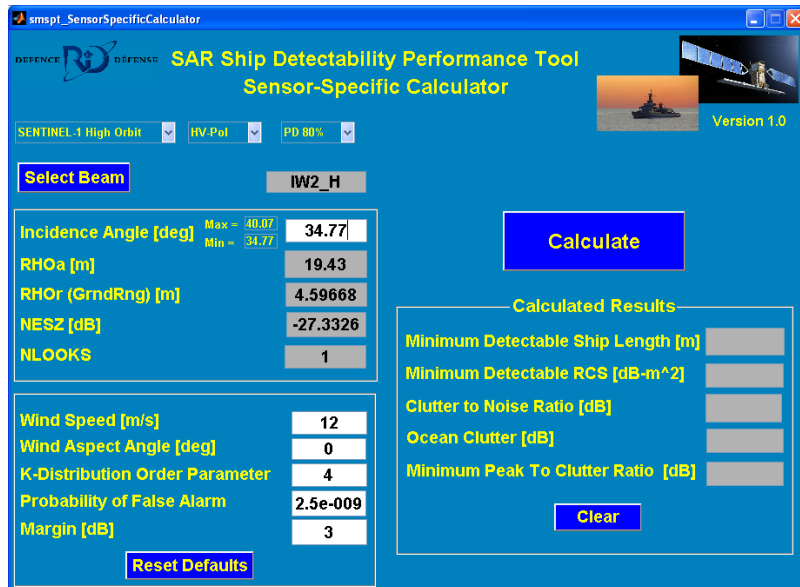


Click on the “Select Beam” button to initiate the *beam selection popup menu* and click-and-drag to **IW2**:

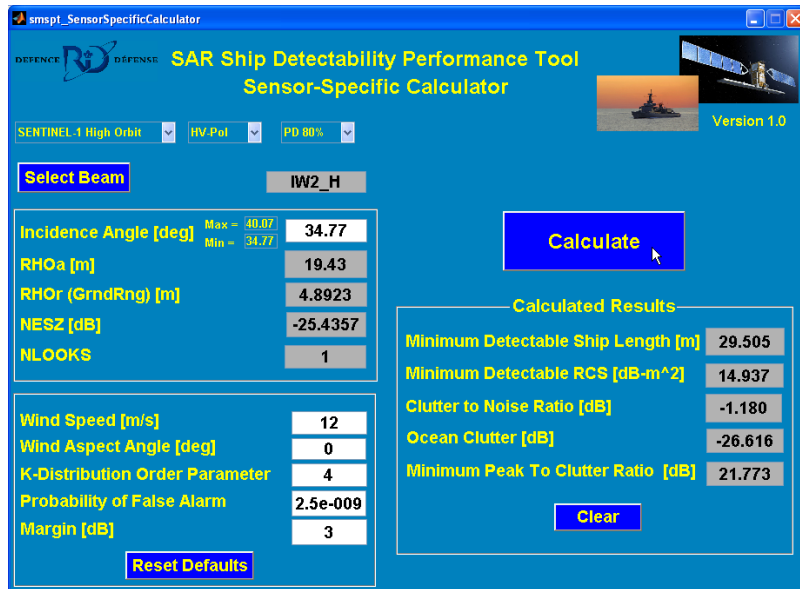


Click on the “OK” button to return to main page.

Next, click on the Incidence Angle text box and change the incidence angle to the near-edge of IW2, i.e., to 34.77° . The minimum and maximum incidence angles for the selected beam are displayed just to the left of the Incidence Angle text box for informational purposes. RHOa, RHOr, NESZ, and NLOOKS are slaved to the Incidence Angle and their values may change with a change to the Incidence Angle.



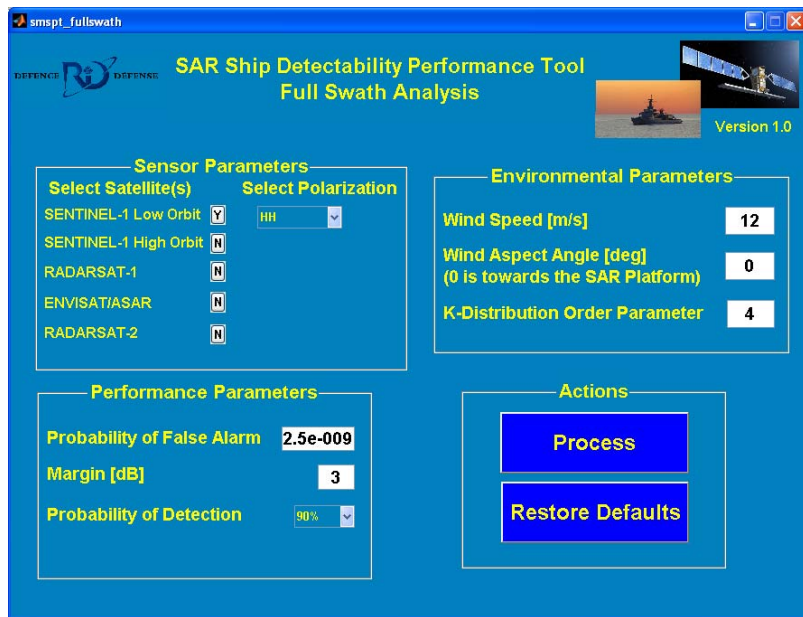
Finally, click on “Calculate” to generate the *Calculated Results*.



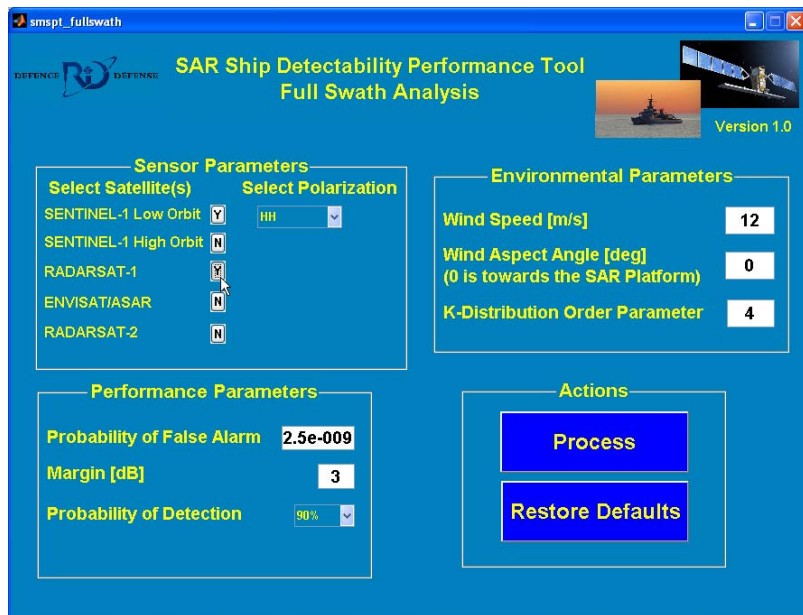
If desired, click on the “Reset Defaults” button to reset the default values in the lower-left sector, or click on “Clear” to clear the *Calculated Results*. Note that clicking on “Calculate” updates all of the calculated results (i.e., it is not essential to click on “Clear” prior to “Calculate”).

A.2 Sensor-Specific Full Swath Analysis

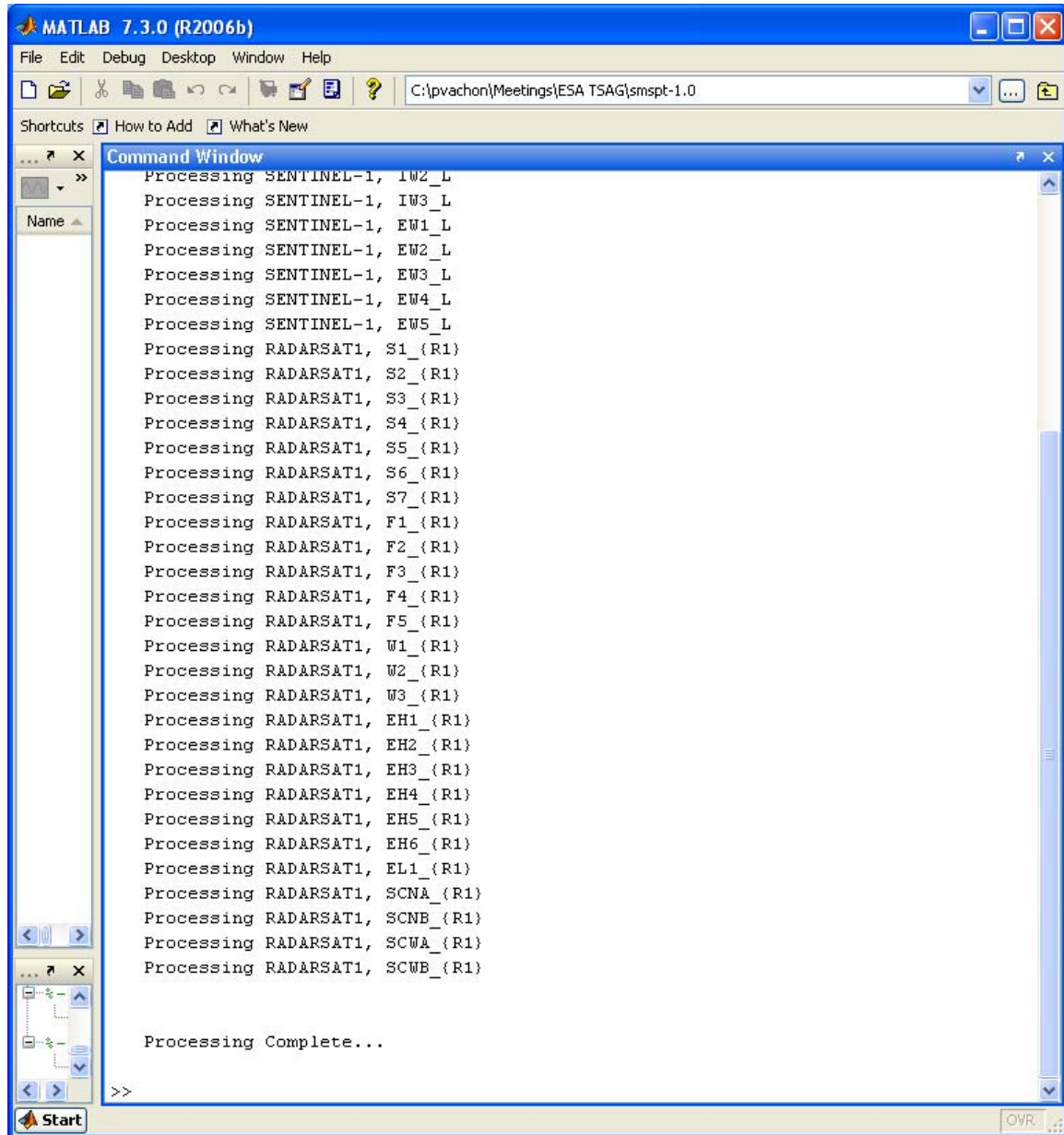
The **Full Swath Analysis** tool provides the user with the ability to plot the *minimum detectable ship length (across the full swath of the beam)* versus *incidence angle* for all the beams of one or more selected sensors, at the selected polarization, and at the desired *performance* and *environmental* parameter settings.



To generate a plot of SENTINEL-1 Low Orbit and RADARSAT-1 sensors at HH-polarization with the default-supplied performance and environmental parameters, click on the RADARSAT-1 “N” radio-button to change it to “Y”



Click on the “Process” button to initiate processing. The processing status is provided in the Matlab® workspace:

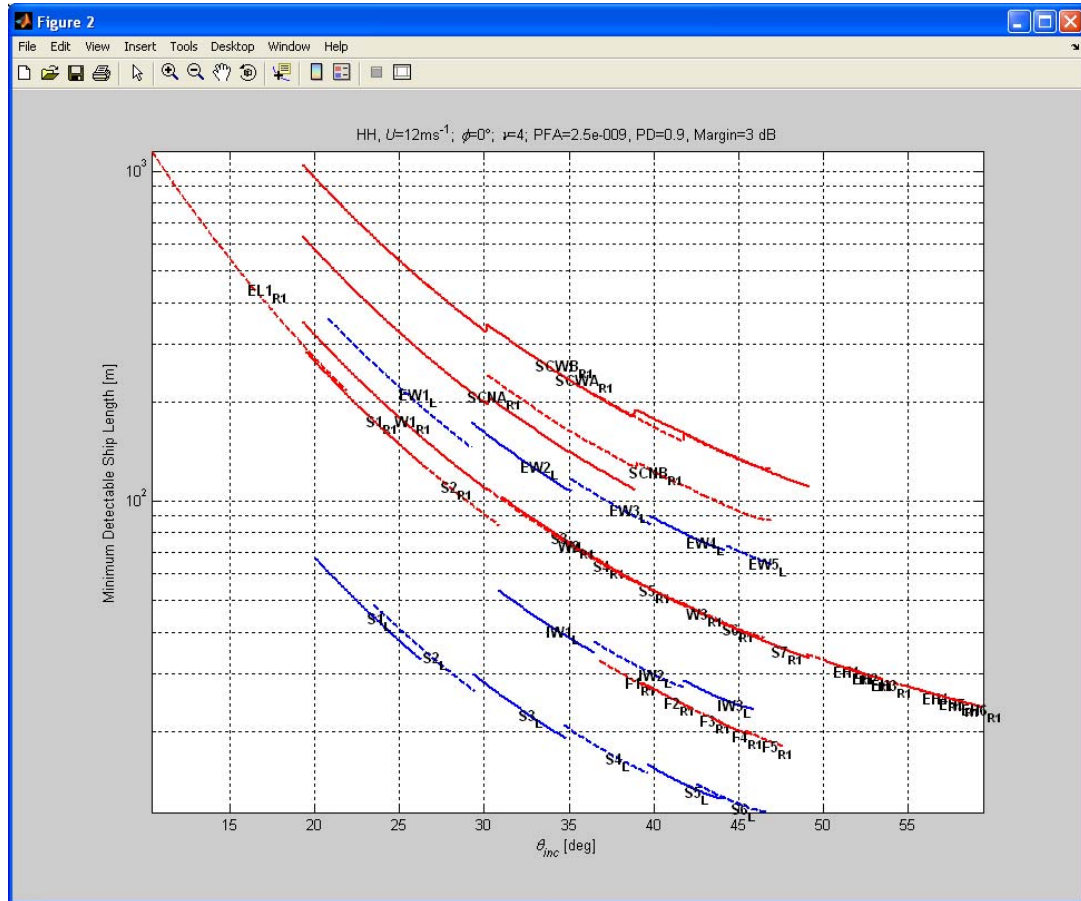


The screenshot shows the MATLAB 7.3.0 (R2006b) interface with the Command Window open. The window title is "Command Window". The workspace path is displayed as "C:\pvachon\Meetings\ESA TSAG\smpt-1.0". The Command Window displays a series of processing log entries, each starting with "Processing" followed by a file name such as "SENTINEL-1, IW2_L", "RADARSAT1, S1_(R1)", etc. The log continues through various file types including L, R1, and R2. At the bottom of the log, the message "Processing Complete..." is visible. The bottom right corner of the window has an "OVR" button.

```
Processing SENTINEL-1, IW2_L
Processing SENTINEL-1, IW3_L
Processing SENTINEL-1, EW1_L
Processing SENTINEL-1, EW2_L
Processing SENTINEL-1, EW3_L
Processing SENTINEL-1, EW4_L
Processing SENTINEL-1, EW5_L
Processing RADARSAT1, S1_(R1)
Processing RADARSAT1, S2_(R1)
Processing RADARSAT1, S3_(R1)
Processing RADARSAT1, S4_(R1)
Processing RADARSAT1, S5_(R1)
Processing RADARSAT1, S6_(R1)
Processing RADARSAT1, S7_(R1)
Processing RADARSAT1, F1_(R1)
Processing RADARSAT1, F2_(R1)
Processing RADARSAT1, F3_(R1)
Processing RADARSAT1, F4_(R1)
Processing RADARSAT1, F5_(R1)
Processing RADARSAT1, W1_(R1)
Processing RADARSAT1, W2_(R1)
Processing RADARSAT1, W3_(R1)
Processing RADARSAT1, EH1_(R1)
Processing RADARSAT1, EH2_(R1)
Processing RADARSAT1, EH3_(R1)
Processing RADARSAT1, EH4_(R1)
Processing RADARSAT1, EH5_(R1)
Processing RADARSAT1, EH6_(R1)
Processing RADARSAT1, EL1_(R1)
Processing RADARSAT1, SCNA_(R1)
Processing RADARSAT1, SCNB_(R1)
Processing RADARSAT1, SCWA_(R1)
Processing RADARSAT1, SCWB_(R1)

Processing Complete...
>>
```

A plot of Minimum Detectable Ship Length in meters (on a logarithmic scale) versus Incidence Angle (on a linear scale) in degrees is produced (the title displays the selected parameters):



For these plots, the sensors are color coded as follows:

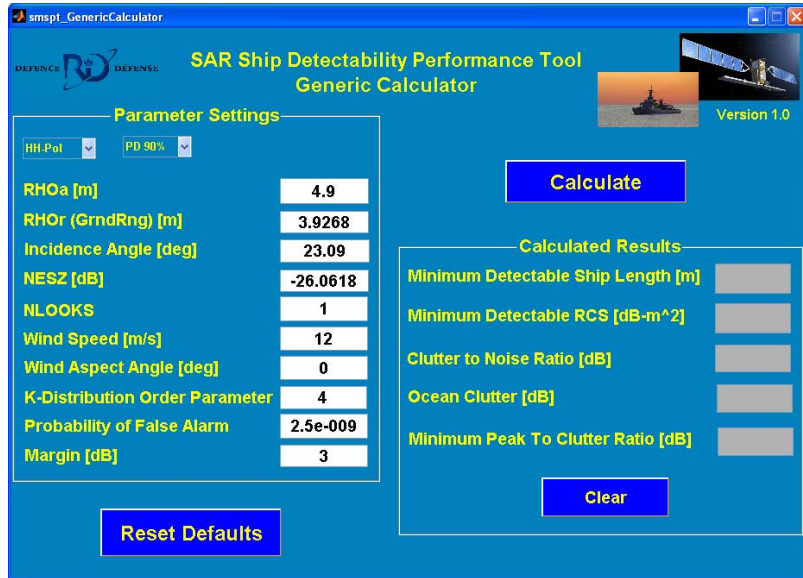
- SENTINEL-1 Low Orbit in **Blue** (each beam has an “L” qualifier to designate Low Orbit);
- SENTINEL-1 High Orbit in **Blue** (each beam has an “H” qualifier to designate High Orbit);
- RADARSAT-1 in **Red** (each beam has an R1 qualifier to designate RADARSAT-1);
- Envisat ASAR in **Green**; and
- RADARSAT-2 in **Black** (each beam has an R2 qualifier to designate RADARSAT-2).

Sequential beams are plotted as a solid line, dashed line, solid line, dashed line, etc. to help differentiate between neighbouring beams. As well, the beam mode name is stamped at the mid-swath of each beam.

The “Restore Defaults” button sets the sensor to SENTINEL-1, HH polarization, and the nominal performance and environmental parameters.

A.3 Generic Ship Detectability Calculator

The *Generic Ship Detectability Calculator* is essentially the same as the *Sensor Specific Calculator*, but without any sensor dependence. As such, all the model parameters are editable with no real constraints.



At startup and by clicking on the “Reset Defaults” button, the parameters are set to the nominal defaults for Sentinel-1 Low Orbit at mid-swath of beam S1.

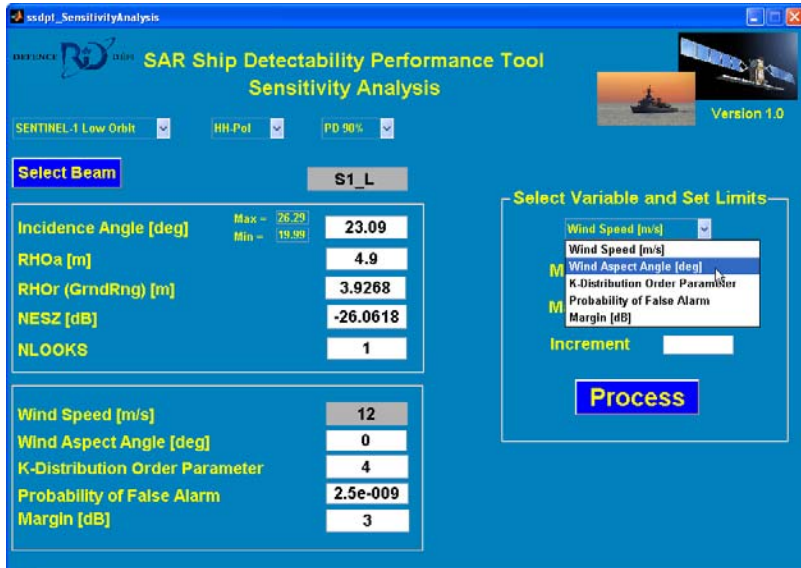
A.4 Ship Detectability Sensitivity Analysis

The *Sensitivity Analysis* tool is sensor specific and is designed to provide the sensitivity of the minimum detectable ship length with respect to varying wind speed, wind aspect angle, K-distribution order parameter, probability of false alarm, and model Margin.

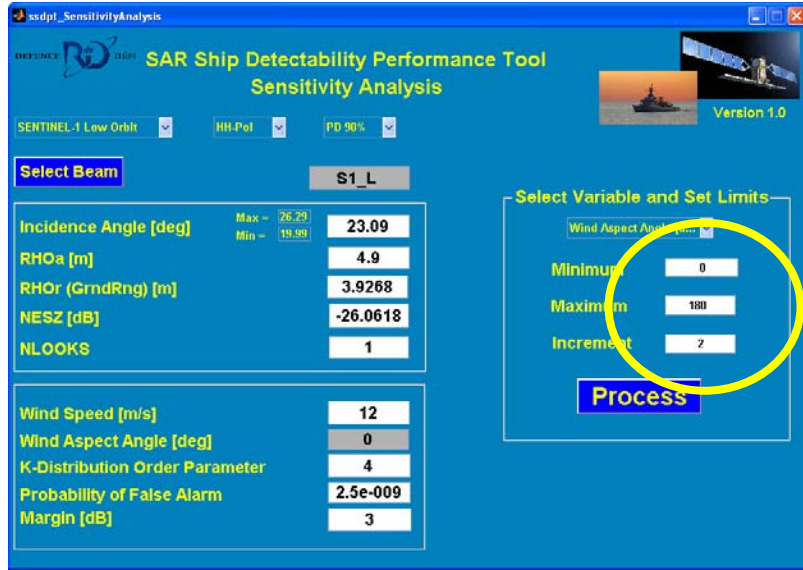


The user selects the sensor, polarization, probability of detection and the beam mode; the tool automatically sets the incidence angle, RHOa, RHOr, NESZ and NLOOKS parameters at nominal mid-swath settings. RHOa, RHOr, NESZ, and NLOOKS are still slaved to the incidence angle but are user editable if desired. The variable of interest is selected, the dynamic range and resolution of the selected variable are input by the user, and a plot of minimum detectable ship length versus the selected variable is produced.

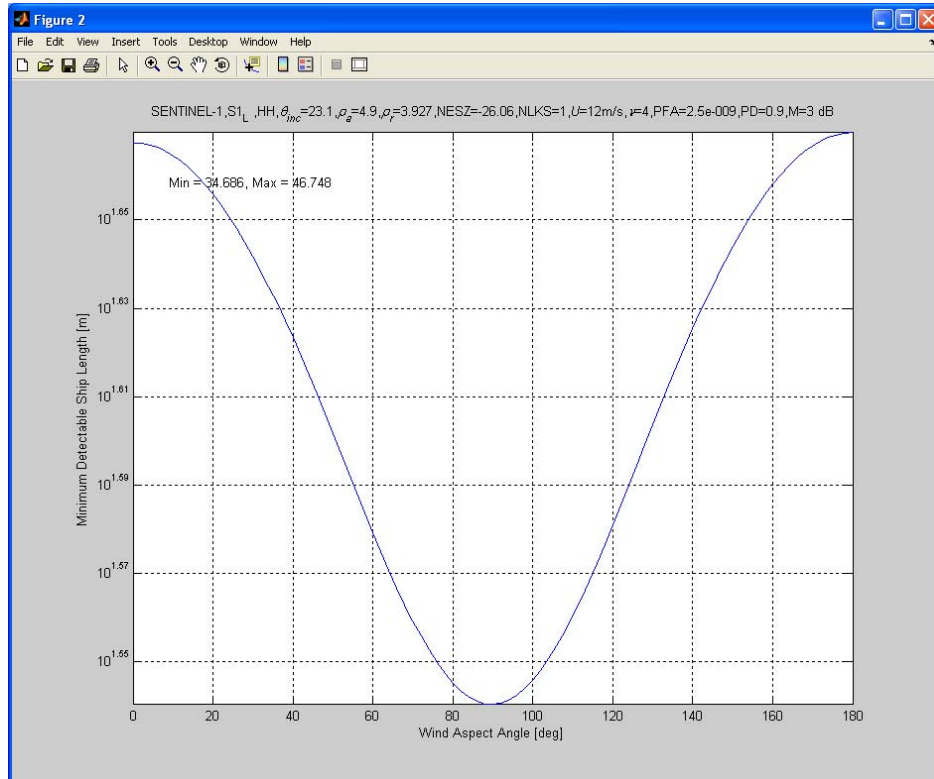
By way of example, a *wind aspect angle* sensitivity analysis is illustrated for Sentinel-1 Low Orbit, HH-pol, PD of 90%, beam S1 and nominal settings for wind speed, K-distribution order parameter, probability of false alarm and margin. From the *Select Variable* popup menu select the *Wind Aspect Angle* parameter:



Next, set *Minimum*, *Maximum* and *Increment* values for the selected variable in the editable text boxes (this sets the variable resolution and dynamic range over which to plot the minimum detectable ship length):

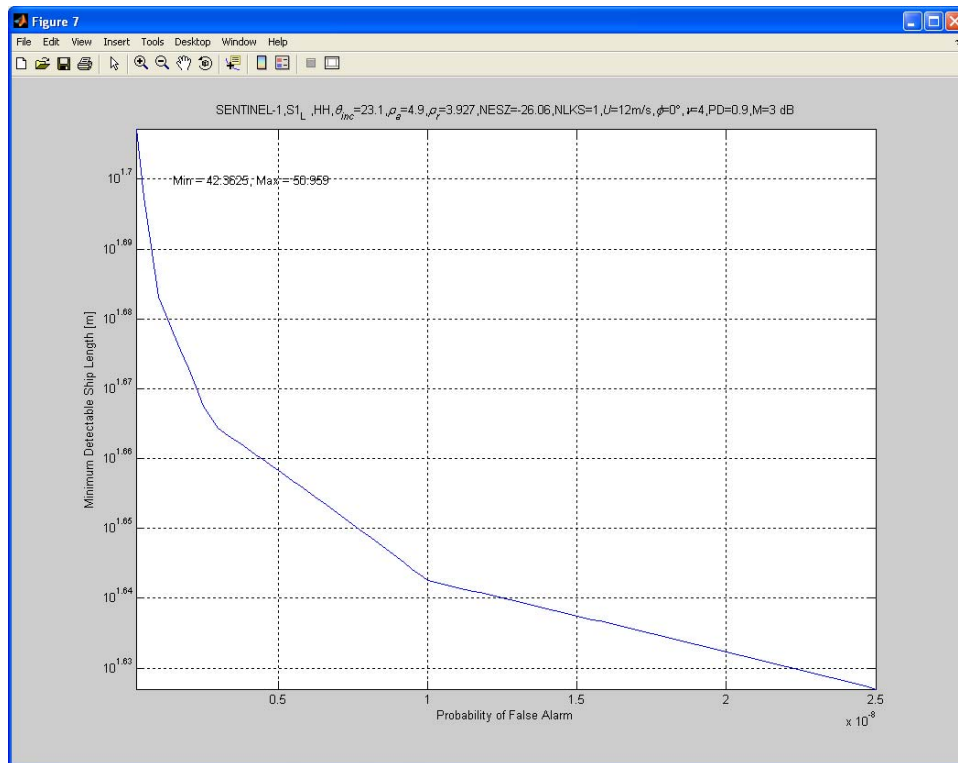
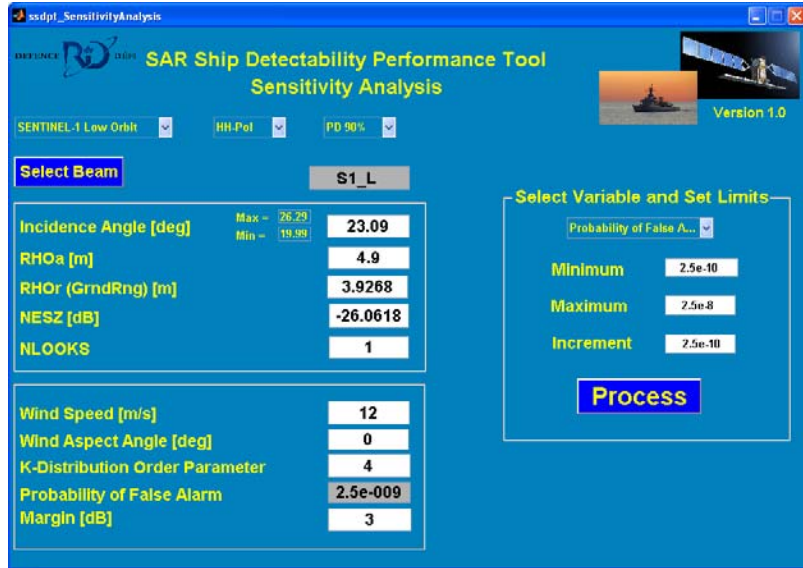


Finally, click on the “Process” button to produce a plot of minimum detectable ship length (on a logarithmic scale) versus wind aspect angle (on a linear scale):



All of the parameter settings are provided in the title and the min and max *minimum detectable ship length* in meters are provided (inset) for information purposes.

As another example, setting a range of values for the Probability of False Alarm can be tricky since the numbers involved are so small. However, choosing the parameters noted below produces the following plot.



Annex B Examples from Envisat ASAR and RADARSAT-1

To demonstrate the relationship between the SAR Ship Detectability Performance Tool and actual SAR data, several case studies have been developed based upon available Envisat ASAR and RADARSAT-1 imagery, with ship validation data via coastal AIS data. In the Envisat case, the same ship has been considered in three different alternating polarization scenes. In the RADARSAT-1 case, two ships in a single SCNA scene have been considered. For each case, the overall image with validated ships is presented, followed by target analysis using a DRDC Ottawa target analysis tool kit. The ship detectability tool was then run based upon actual image parameters, and the tool output was considered in the context of the available image data.

The cases considered are summarized in Table 19 and the tool outputs are provided in Table 20. In the latter table, the wind direction was taken as zero, unless an external wind direction source was available. In either case, the retrieved wind speed sets the CNR for the performance calculations. The K-distribution order parameter (ν) was estimated from the actual number of statistically independent looks for the specific beam mode and the observed MSVR in the vicinity of the ship of interest. The case studies are presented and discussed in the following sections.

Table 19: Demonstration products – case studies.

Case	Date	Location	Sensor	Mode	Pol	Ship	L [m]	θ [deg]	PCR [dB]
1	9 Dec. 2006	Gibraltar	ASAR AP	IS1	HH	<i>Le Rif</i> , Ferry	129	15.6	N/A
					HV				27.5
2	22 Dec. 2006	Gibraltar	ASAR AP	IS3	HH	<i>Le Rif</i> , Ferry	129	28.8	16.6
					HV				19.9
3	16 Dec. 2006	Gibraltar	ASAR AP	IS7	HH	<i>Le Rif</i> , Ferry	129	44.4	30.8
					HV				23.6
4	4 March 2004	Halifax	ASAR AP	IS3	HH	<i>Quest</i> , Research	76	29.7	17.7
					VV				13.1
					HH	<i>Grenfell</i> , CCG	68	29.8	16.0
					VV				12.4
					HH				N/A
					VV				9.3
5	3 Jan. 2007	Gibraltar	ASAR AP	IS1	VV	<i>Nakhchivan</i> , Cargo	140	14.8	N/A
					VH				22.0
					VV	<i>Stav. Prince</i> , Tanker	244	15.0	15.8
					VH				32.6
					VV				N/A
					VH				20.7
6	9 July 2006	Dover	R1	SCNA	HH	<i>Leo Glory</i> , Tanker	334	38.0	31.3
					HH				25.2

Table 20: Demonstration products – ship detectability tool inputs and outputs.

Case	Pol	Ship	U [m/s]	φ [deg]	MSVR	Lks	ν	Min L [m]	Min PCR [dB]
1	HH	<i>Le Rif, Ferry</i>	1	21	1.72	1.76	119	267.6	14.1
	HV				1.98	1.76	∞	85.4	16.2
2	HH	<i>Le Rif, Ferry</i>	4.9	0	1.94	2.25	20	55.4	15.0
	HV				2.44	2.25	∞	54.9	21.8
3	HH	<i>Le Rif, Ferry</i>	6.3	0	3.75	3.73	∞	17.8	13.2
	HV				4.50	3.73	∞	39.4	21.5
4	HH	<i>Quest, Research</i>	6.1	0	2.11	2.25	49	52.2	14.3
	VV				2.28	2.25	∞	59.1	13.5
	HH	<i>Grenfell</i> , CCG			2.11	2.25	49	52.2	14.3
	VV				2.28	2.25	∞	59.1	13.5
	HH	<i>Sambro</i> , CCG			2.11	2.25	49	52.2	14.3
	VV				2.28	2.25	∞	59.1	13.5
5	VV	<i>Nakhchivan</i> , Cargo	5.6	0	1.66	1.76	45.8	399.0	14.8
	VH				1.81	1.76	∞	112.7	15.4
	VV	<i>Stav. Prince</i> , Tanker			1.66	1.76	45.8	399.0	14.8
	VH				1.81	1.76	∞	112.7	15.4
	VV	<i>Sara1</i> , Ferry			1.66	1.76	45.8	399.0	14.8
	VH				1.81	1.76	∞	112.7	15.4
6	HH	<i>Leo Glory</i> , Tanker	15.3	90	10.4	3.50	∞	50.8	12.3
	HH	<i>Sandettie</i> , Cargo		90	10.4	3.50	∞	55.6	12.3

B.1 Case 1 – ASAR dual polarization HH+HV, low incidence angle

These cases are summarized in Figure 27. In this figure, as well as the next three figures, the top row shows the overall image (left) and a zoom of the outlined area (right). The image channels are colour coded in red, green, and blue (RGB) as indicated in the caption. The next rows show zooms on the ships of interest, either for the available polarizations or for ships considered, while the next rows show point target analyses. The bottom row shows screen shots of the Ship Detectability Tool. The constituent images in the case studies are presented here in small format. They are available along with other supporting information at full resolution in the final report presentation. The ships in this image were validated using coastal AIS data.

In Case 1 there is a known ship at an incidence angle of 15.6° that is not visible in the co-polarization channel but is visible in the cross-polarization channel. The minimum detectable ship lengths are 268 m and 85 m for HH and HV respectively, with the actual ship length of 129 m being between the two. This case illustrates improved ship detection performance at smaller incidence angles for cross-polarization data.

B.2 Cases – ASAR dual polarization HH+HV, medium incidence angle

This case is summarized in Figure 28 and shows the same ship as was considered in Case 1 but at an incidence angle of 29°. The minimum detectable ship lengths are about 55 m for both HH and HV. The observed PCRs are 17 dB and 20 dB for HH and HV, respectively. This case illustrates ship detection performance that is comparable for the two channels; the ship of interest is readily detectable in both channels.

B.3 Case 3 – ASAR dual polarization HH+HV, high incidence angle

This case is summarized in Figure 29 and shows the same ship as was considered in Cases 1 and 2, but at an incidence angle of 44°. The minimum detectable ship lengths are about 18 m and 40 m for the HH and HV channels, respectively. The observed PCRs are 31 dB and 24 dB for HH and HV, respectively. These cases illustrate improved ship detection performance at larger incidence angles for co-polarization data; the ship of interest is readily detectable in both channels.

B.4 Case 4 – ASAR dual polarization HH+VV, small ships

This case is summarized in Figure 30 and shows three known ships (74 m, 68 m, and 16 m) that were imaged during a controlled ship detection trial held off Halifax in 2004. The minimum detectable ship lengths are 52 m and 59 m for HH and VV, respectively. The two larger ships are readily visible in both available channels. The smaller ship is marginally visible in the HV channel. This is consistent with the minimum detectable ship length relative to the actual vessel sizes.

B.5 Case 5 – ASAR dual polarization VV+VH

This case is summarized in figure and shows three known ships (244 m, 140 m, and 119 m) that were validated using coastal AIS data. The minimum detectable ship lengths are 399 m and 113 m for VV and VH, respectively. With a PCR of 15.8 dB, even the largest ship is barely visible in the VV channel. All three ships are readily visible in the VH channel, which is consistent with the minimum detectable ship length relative to the actual vessel sizes.

B.6 Case 6 – RADARSAT-1 ScanSAR Narrow

This case is summarized in **Error! Reference source not found.** and shows a tanker (334 m) and a cargo ship (142 m) in RADARSAT-1 SCNA imagery. The minimum detectable ship lengths are 51 m and 56 m, respectively, and both ships are readily detectable with PCRs of 31 dB and 25 dB, respectively. These cases illustrate good ship detection performance across a broad image swath of 300 km.

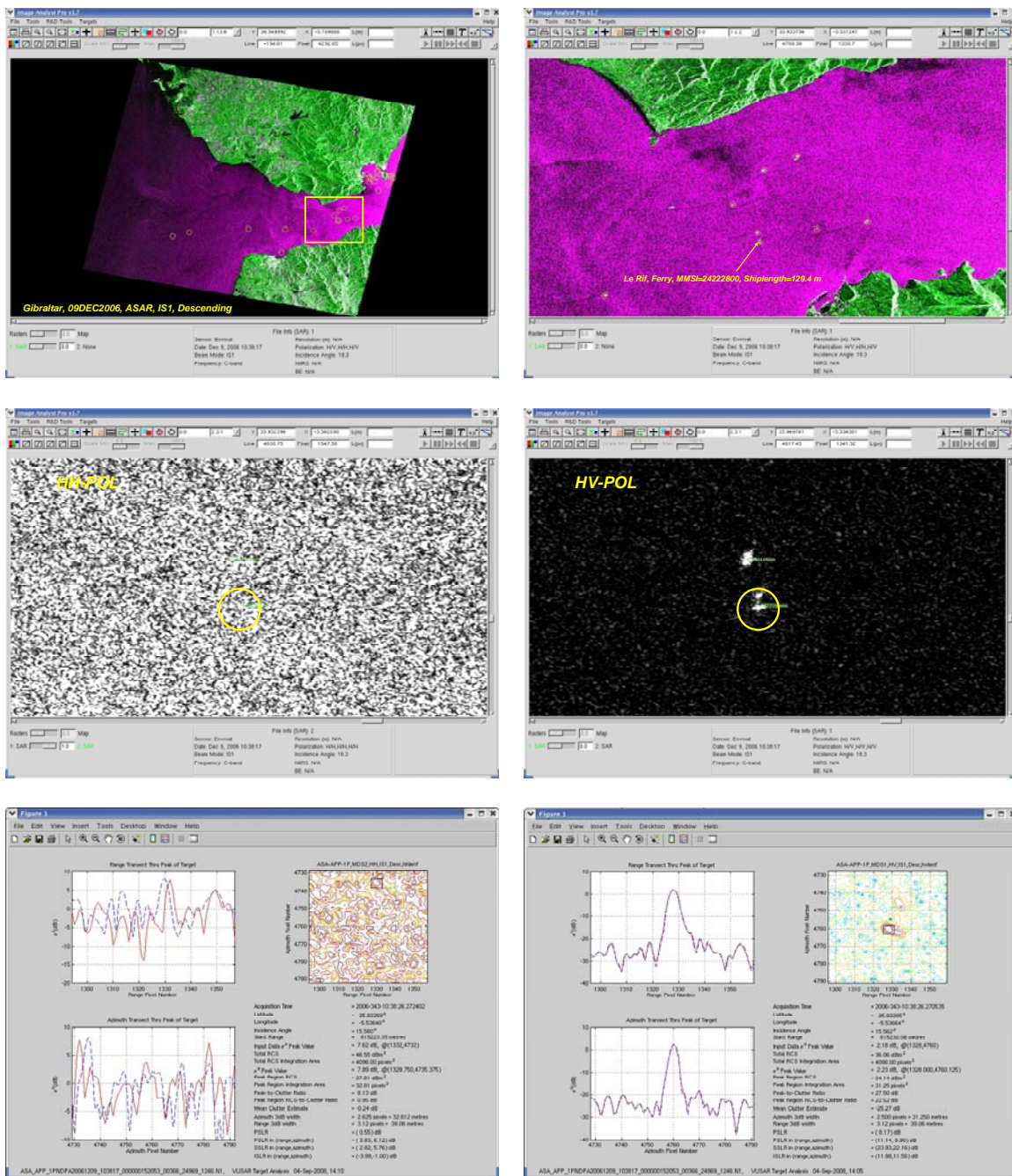


Figure 27: Case 1 with HH (left) and HV (right). RGB = (HV, HH, HV). (Continued on next page.)

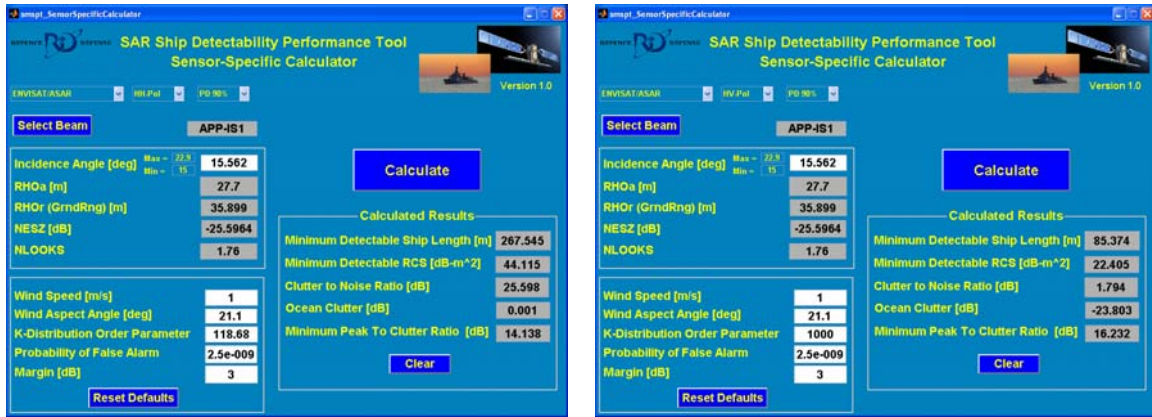


Figure 27: Concluded.

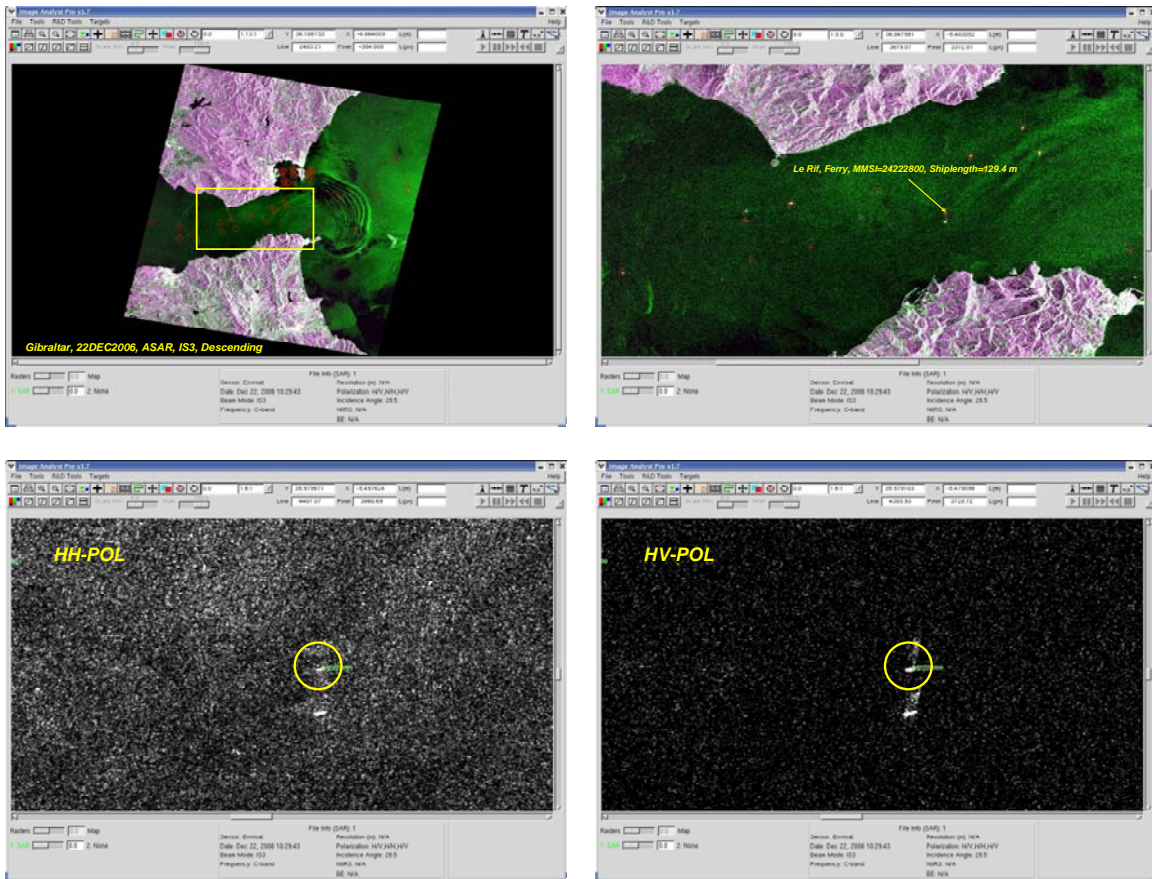


Figure 28: Case 2 with HH (left) and HV (right). RGB = (HV, HH, HV). (Continued on next page.)

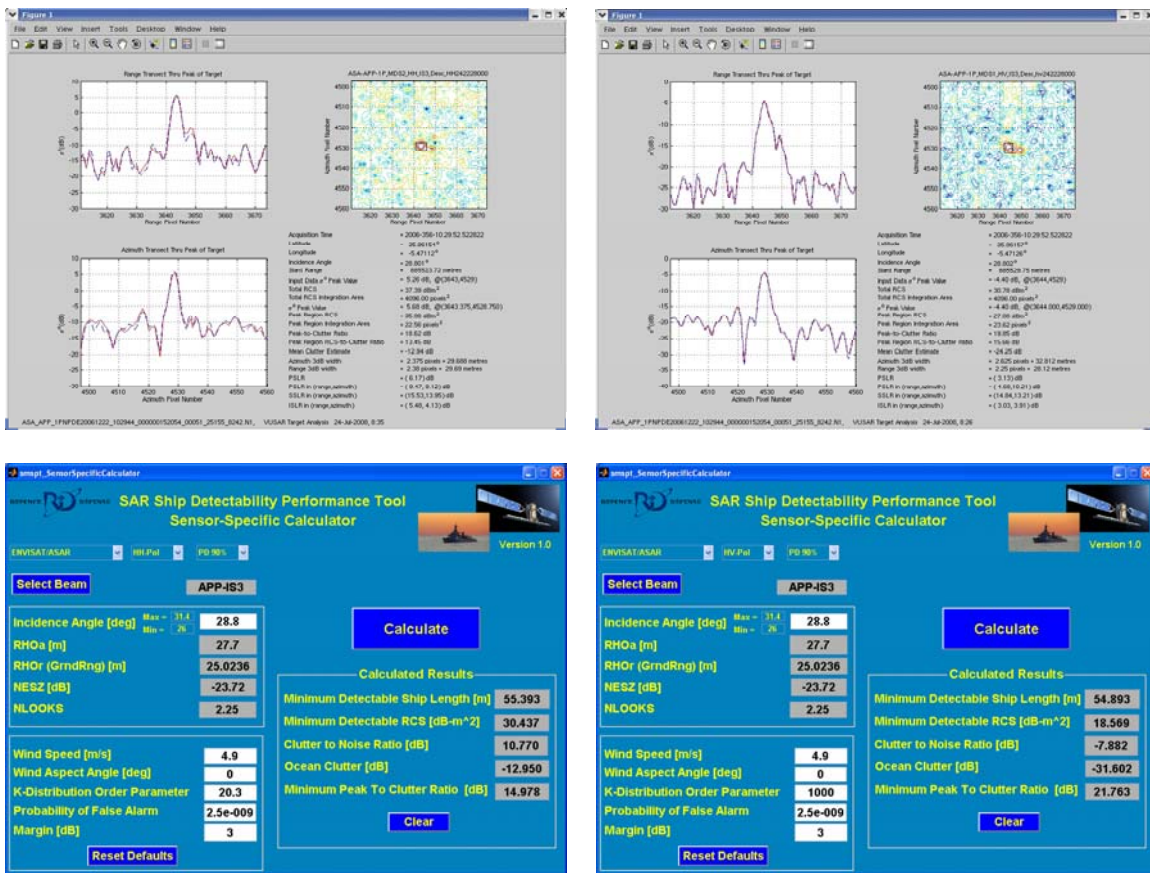


Figure 28: Concluded.

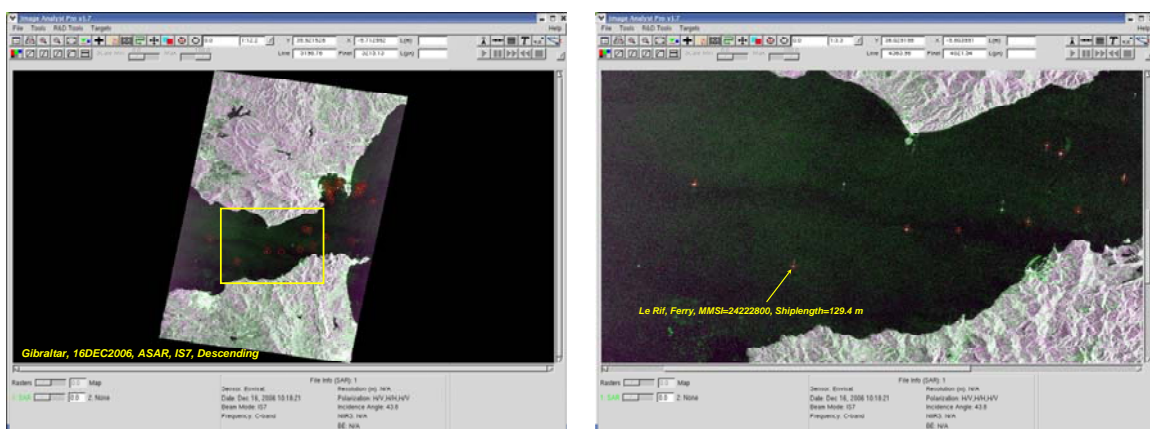


Figure 29: Case 3 with HH (left) and HV (right). $RGB = (HV, HH, HV)$. (Continued on next page.)

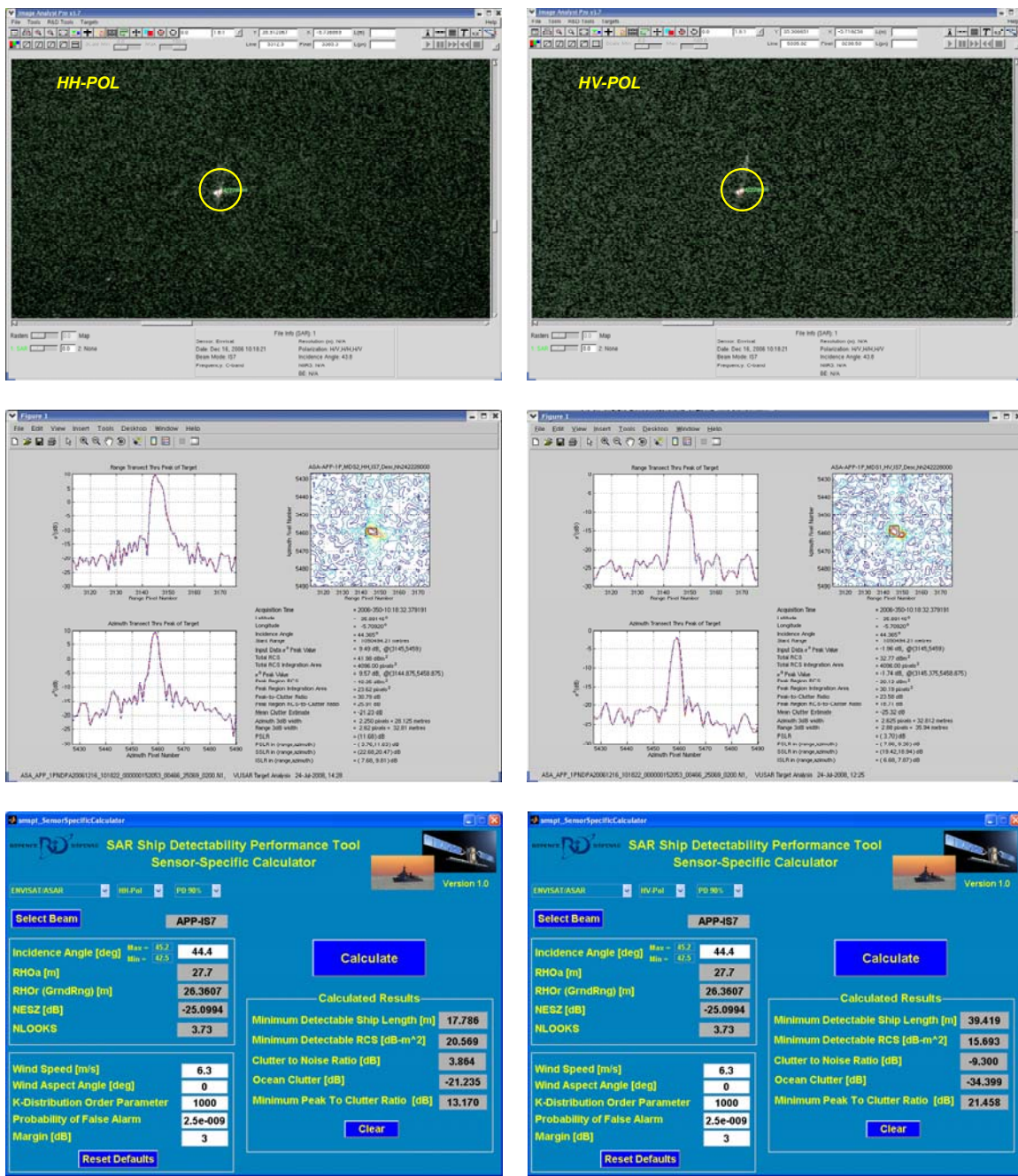


Figure 29: Concluded.

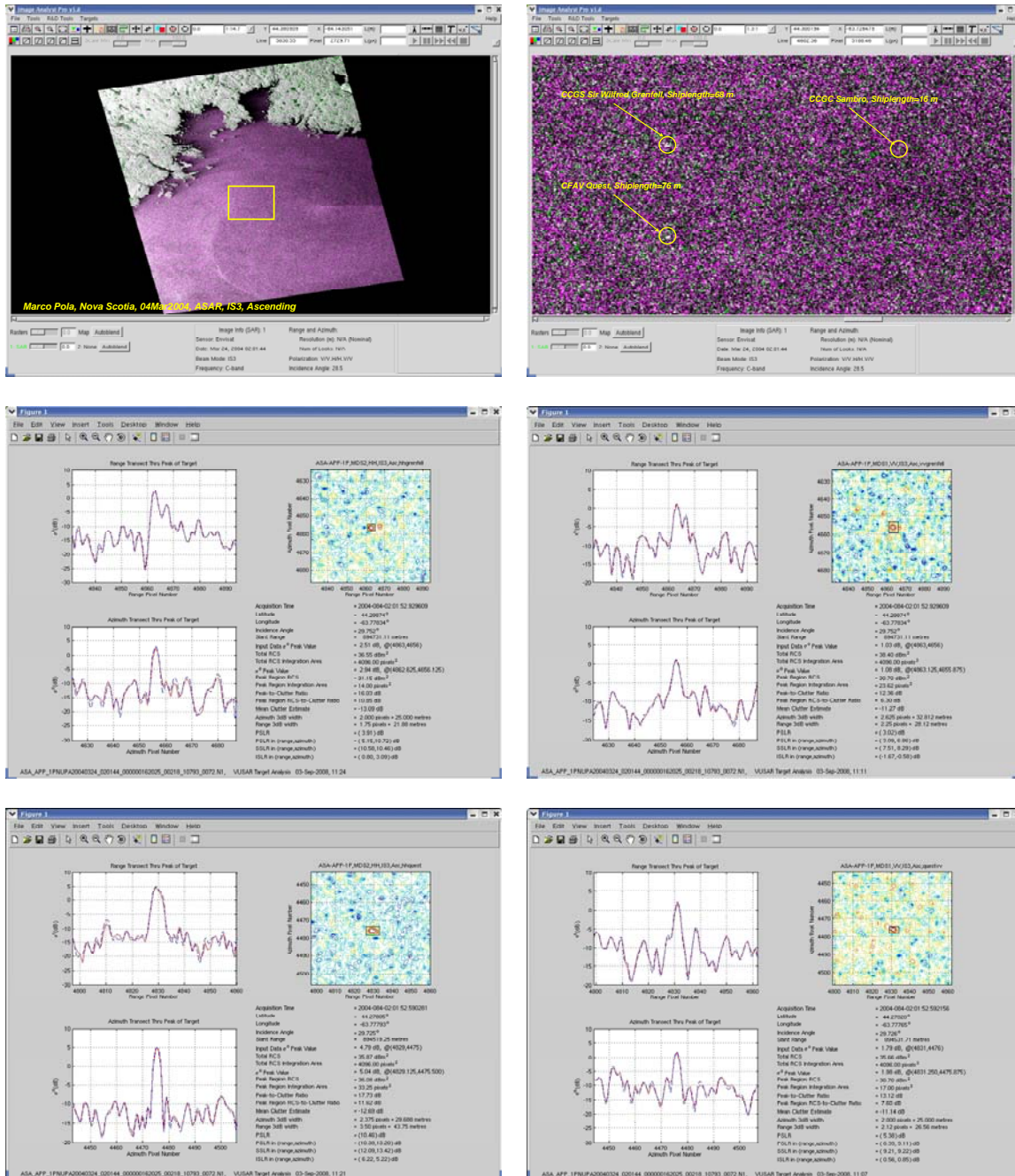


Figure 30: Case 4 with Grenfell (left) and Quest (right). RGB = (VV, HH, VV). (Continued on next page.)

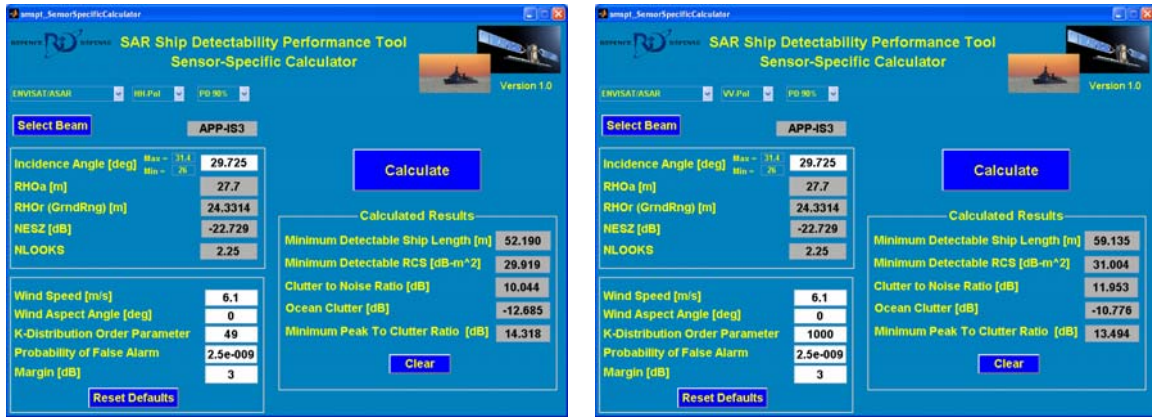


Figure 30: Concluded.

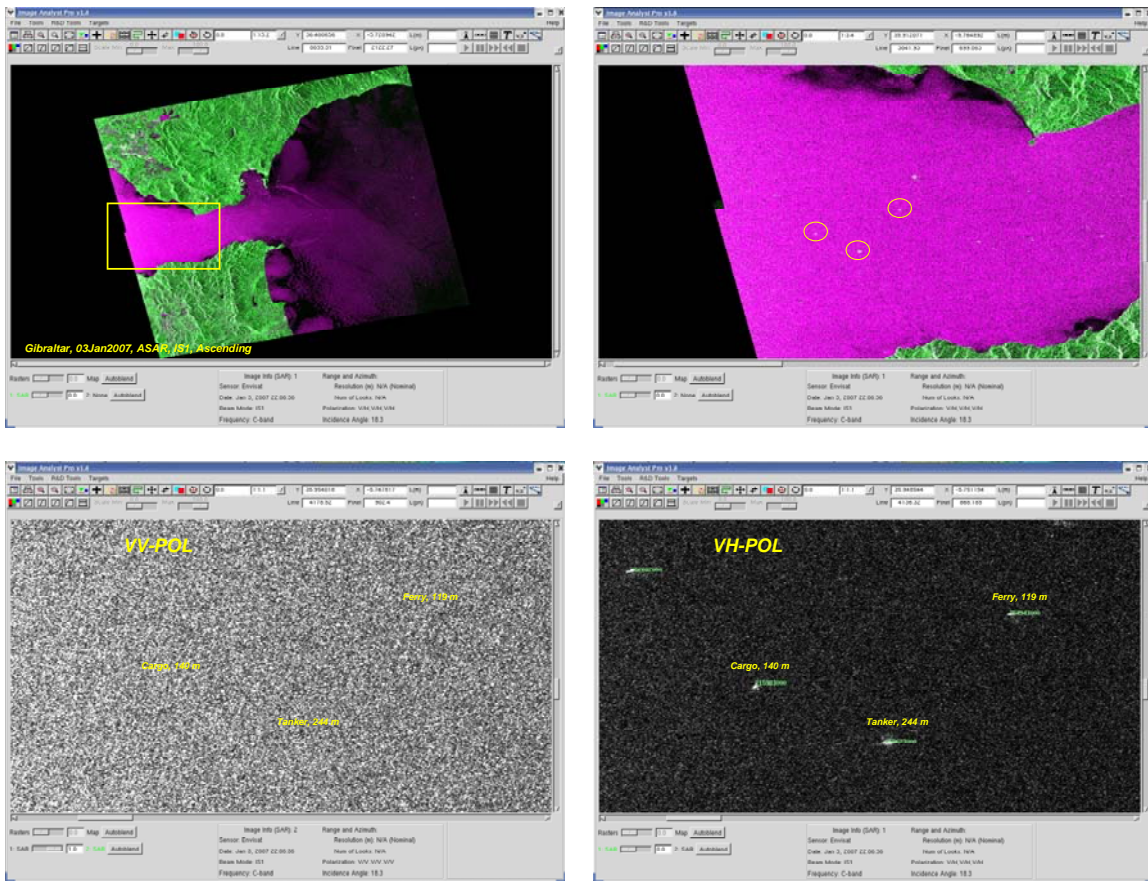


Figure 31: Case 5 with VV (left) and VH (right). RGB = (VV, VH, VV). (Continued on next page.)

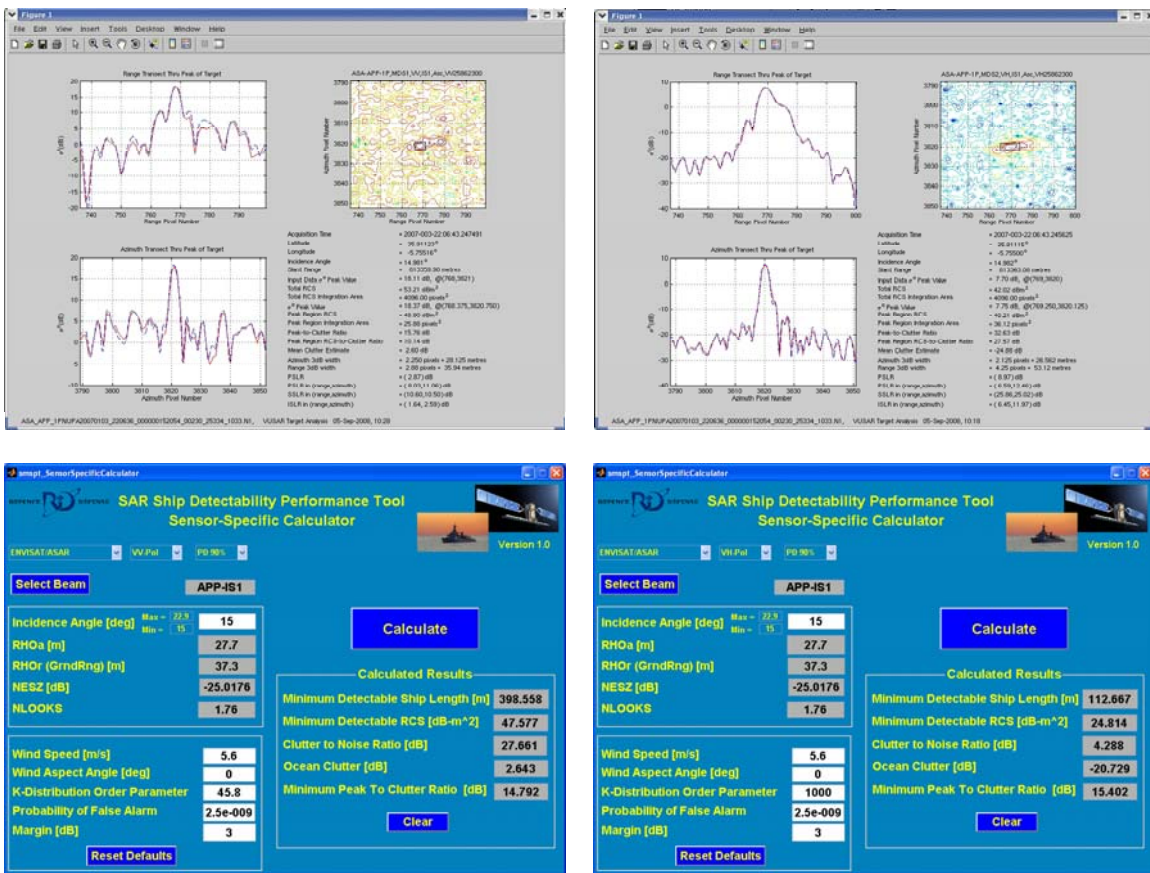


Figure 31: Concluded.

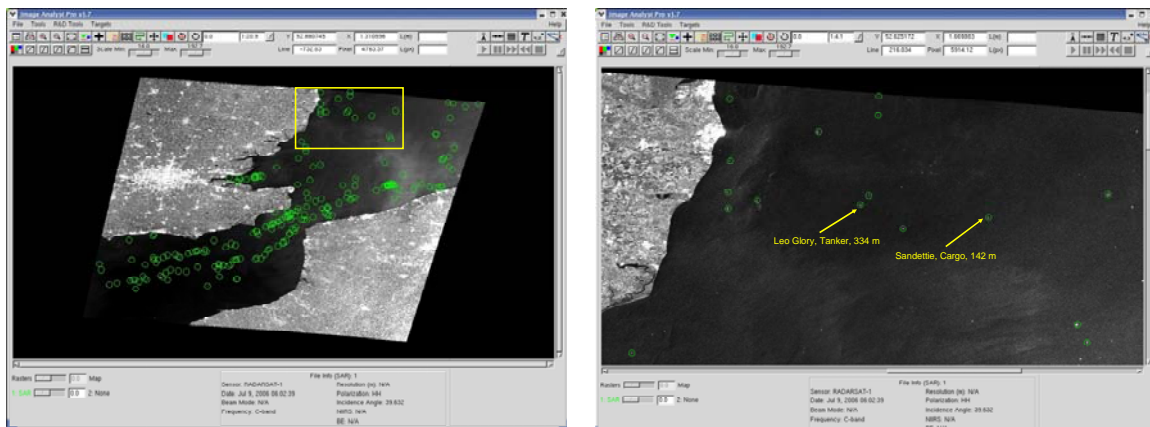


Figure 32: Case 6 with a tanker (left) and a cargo ship (right). (Continued on next page.)

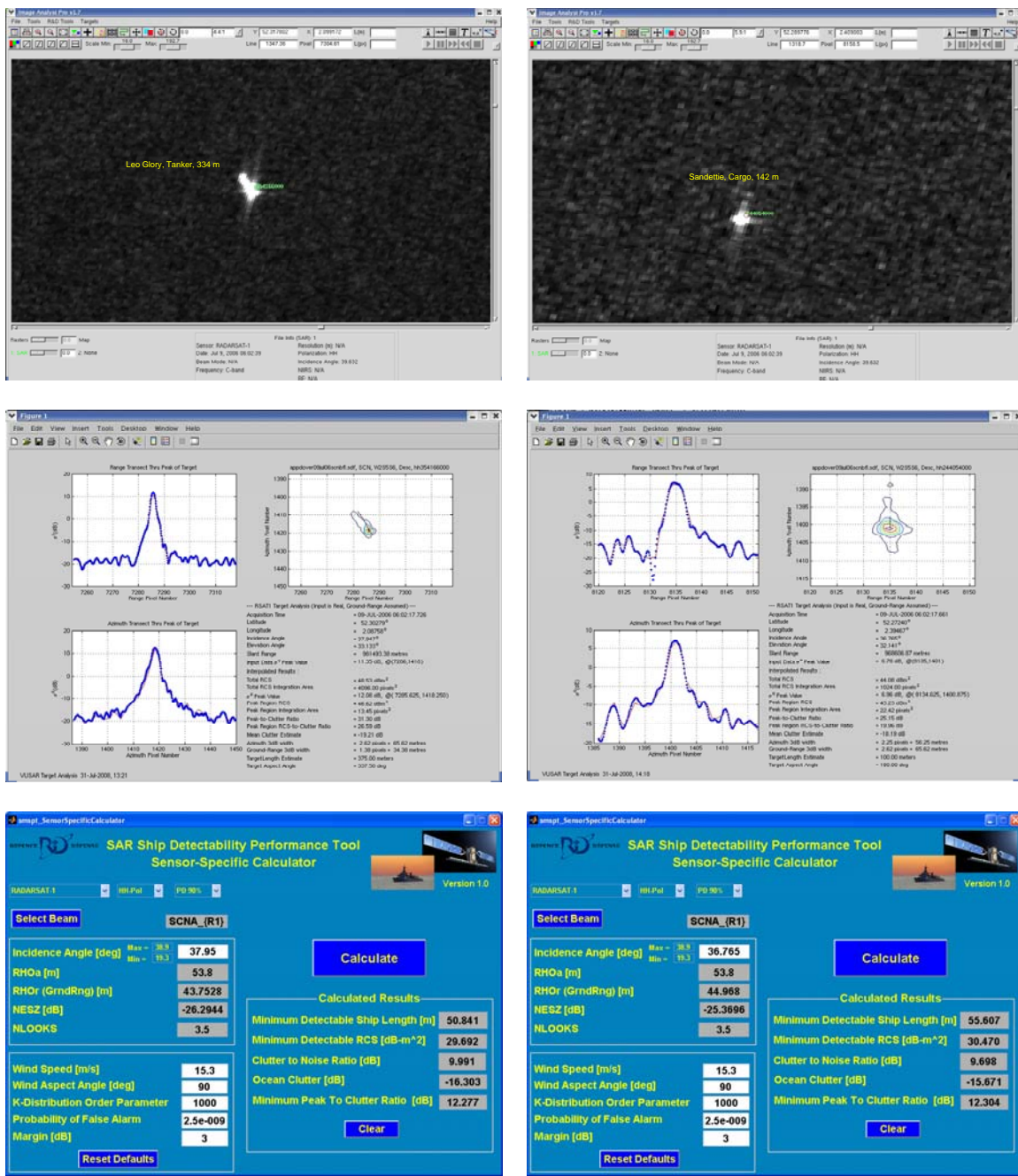


Figure 32: Concluded.

This page intentionally left blank.

List of acronyms

AIS	Automatic Identification System
AMAP	Analysis of Marine Applications Potential
AP	Alternating Polarization mode (Envisat ASAR)
APP	Alternating Polarization Product (Envisat ASAR)
ASAR	Advanced SAR (Envisat)
CCG	Canadian Coast Guard
CNR	Clutter-to-Noise Ratio
Co-Pol	Co-polarization (i.e., HH or VV)
Cross-Pol	Cross-Polarization (i.e., HV or VH)
DRDC	Defence Research & Development Canada
ECDF	Empirical Cumulative Density Function
EH	Extended High mode (RADARSAT)
EL	Extended Low mode (RADARSAT)
ENL	Equivalent Number of Looks
ESA	European Space Agency
EW	Extra Wide swath mode (Sentinel-1)
F	Fine mode (RADARSAT)
FY	First Year
GMES	Global Monitoring for Environment and Security
HH	Horizontal transmit, Horizontal receive
HV	Horizontal transmit, Vertical receive
IMP	Precision Image Product (Envisat ASAR)
IS	Image Swath mode (Envisat ASAR)
IW	Interferometric Wide swath mode (Sentinel-1)
MY	Multi Year
NESZ	Noise-Equivalent Sigma-Zero
PDF	Probability Density Function
PRF	Pulse Repetition Frequency
R1	RADARSAT-1
R2	RADARSAT-2

R&D	Research & Development
RCS	Radar Cross Section
RGB	Red, Green, Blue
S	Strip map mode (Sentinel)
S	Standard mode (RADARSAT)
SAR	Synthetic Aperture Radar
SCN	ScanSAR Narrow (RADARSAT)
SCNA	ScanSAR Narrow A (RADARSAT)
SCNB	ScanSAR Narrow B (RADARSAT)
SS	ScanSAR Sub-Swath (Envisat ASAR)
SCW	ScanSAR Wide (RADARSAT)
SCWA	ScanSAR Wide A (RADARSAT)
SCWB	ScanSAR Wide B (RADARSAT)
SNR	Signal to Noise Ratio
VH	Vertical transmit, Horizontal receive
VHF	Very High Frequency
VV	Vertical transmit, Vertical receive
W	Wide mode (RADARSAT)
W	Wave mode (Sentinel-1)
WSM	Wide Swath Mode (Envisat ASAR)

DOCUMENT CONTROL DATA

(Security classification of title, body of abstract and indexing annotation must be entered when the overall document is classified)

1. ORIGINATOR (The name and address of the organization preparing the document. Organizations for whom the document was prepared, e.g. Centre sponsoring a contractor's report, or tasking agency, are entered in section 8.) Defence R&D Canada – Ottawa 3701 Carling Avenue Ottawa, Ontario K1A 0Z4		2. SECURITY CLASSIFICATION (Overall security classification of the document including special warning terms if applicable.) <u>UNCLASSIFIED</u>
3. TITLE (The complete document title as indicated on the title page. Its classification should be indicated by the appropriate abbreviation (S, C or U) in parentheses after the title.) GMES Sentinel-1 Analysis of Marine Applications Potential (AMAP)		
4. AUTHORS (last name, followed by initials – ranks, titles, etc. not to be used) Vachon, P.W.; Wolfe, J.		
5. DATE OF PUBLICATION (Month and year of publication of document.) October 2008	6a. NO. OF PAGES (Total containing information, including Annexes, Appendices, etc.) 98	6b. NO. OF REFS (Total cited in document.) 36
7. DESCRIPTIVE NOTES (The category of the document, e.g. technical report, technical note or memorandum. If appropriate, enter the type of report, e.g. interim, progress, summary, annual or final. Give the inclusive dates when a specific reporting period is covered.) External Client Report		
8. SPONSORING ACTIVITY (The name of the department project office or laboratory sponsoring the research and development – include address.) Defence R&D Canada – Ottawa 3701 Carling Avenue Ottawa, Ontario K1A 0Z4		
9a. PROJECT OR GRANT NO. (If appropriate, the applicable research and development project or grant number under which the document was written. Please specify whether project or grant.) 15el04	9b. CONTRACT NO. (If appropriate, the applicable number under which the document was written.) ESTEC Contract No. 21303/07/NL/CB	
10a. ORIGINATOR'S DOCUMENT NUMBER (The official document number by which the document is identified by the originating activity. This number must be unique to this document.) DRDC Ottawa ECR 2008-218	10b. OTHER DOCUMENT NO(s). (Any other numbers which may be assigned this document either by the originator or by the sponsor.)	
11. DOCUMENT AVAILABILITY (Any limitations on further dissemination of the document, other than those imposed by security classification.) Unlimited		
12. DOCUMENT ANNOUNCEMENT (Any limitation to the bibliographic announcement of this document. This will normally correspond to the Document Availability (11). However, where further distribution (beyond the audience specified in (11) is possible, a wider announcement audience may be selected.) Unlimited		

13. **ABSTRACT** (A brief and factual summary of the document. It may also appear elsewhere in the body of the document itself. It is highly desirable that the abstract of classified documents be unclassified. Each paragraph of the abstract shall begin with an indication of the security classification of the information in the paragraph (unless the document itself is unclassified) represented as (S), (C), (R), or (U). It is not necessary to include here abstracts in both official languages unless the text is bilingual.)

This document is the Final Report deliverable under ESTEC Contract No. 21303/07/NL/CB “GMES Sentinel-1 analysis of marine applications potential (AMAP)”. The document includes ship detectability modelling that has been carried out for Sentinel-1, including development of a ship detectability tool that applies to Sentinel-1, RADARSAT-1, RADARSAT-2, and Envisat ASAR image data. Limitations of the tool’s predictions are discussed, and examples from RADARSAT-1 and Envisat ASAR are provided to illustrate the performance of the tool. Also considered is Sentinel-1’s expected capability for other maritime applications, including iceberg detection, wind retrieval, oil spill detection, sea ice surveillance, and ship wake detection. In general, the Interferometric Wide Swath mode with its high spatial resolution and 250 km swath will be a useful mode for maritime surveillance in the littoral zone.

14. **KEYWORDS, DESCRIPTORS or IDENTIFIERS** (Technically meaningful terms or short phrases that characterize a document and could be helpful in cataloguing the document. They should be selected so that no security classification is required. Identifiers, such as equipment model designation, trade name, military project code name, geographic location may also be included. If possible keywords should be selected from a published thesaurus, e.g. Thesaurus of Engineering and Scientific Terms (TEST) and that thesaurus identified. If it is not possible to select indexing terms which are Unclassified, the classification of each should be indicated as with the title.)

synthetic aperture radar; SAR; Sentinel-1; marine applications; ship detection

Defence R&D Canada

Canada's leader in Defence
and National Security
Science and Technology

R & D pour la défense Canada

Chef de file au Canada en matière
de science et de technologie pour
la défense et la sécurité nationale



www.drdc-rddc.gc.ca